國立臺灣大學工學院材料科學與工程學研究所

碩士論文

Department of Materials Science and Engineering
College of Engineering
National Taiwan University

Master Thesis

新穎倒置結構之有機太陽能電池

Novel Devices Based on Inverted Type Polymer Photovoltaics

李昱瑩

Yu-Ying Lee

指導教授：陳俊維 博士

Advisor: Chun-Wei Chen, Ph. D.

中華民國 100 年 6 月

June, 2011

Novel Devices Based on Inverted Type Polymer Photovoltaics

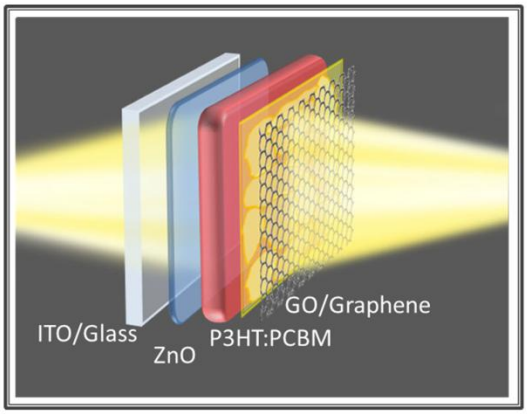

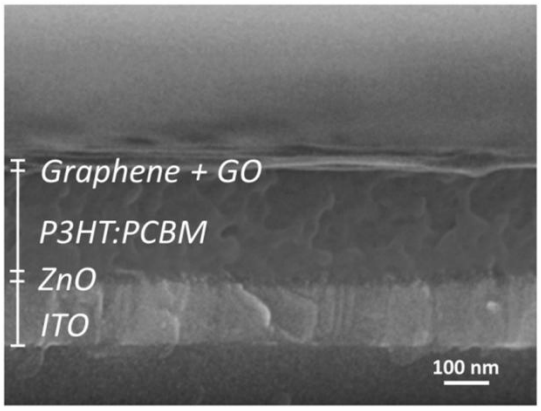

李昱瑩　碩士　民國 100 年 6 月

國立臺灣大學碩士學位論文
口試委員會審定書

論文中文題目： 新穎倒置結構之有機太陽能電池

論文英文題目： Novel devices based on inverted type polymer photovoltaics

本論文係**李昱瑩**(R98527031)在國立臺灣大學材料科學與工程學系、所完成之碩士學位論文，於民國 100 年 6 月 23 日承下列考試委員審查通過及口試及格，特此證明

口試委員： 陳俊維 陳俊維
（指導教授）

陳學禮 陳學禮

吳季珍 吳季珍

系主任、所長 高振宏 高振宏 （簽名）

Acknowledgements

時光飛逝，記得當時從大三開始作專題，到現在已經過了四年，每年看著學長們一個個畢業、離開，終於也輪到自己了。從當時的懵懂無知，到現在些微地可以獨當一面，這都要感謝許多人一路上對我的幫助。

首先要感謝我的指導教授陳俊維老師，陳老師對於研究的熱忱與專注，使我在這幾年的研究期間獲益良多，除了培養我獨立思考的能力，更重要的是養成了我對於做人做事以及學習的良好態度。老師除了提供我們良好的實驗環境，更給了我許多出國參加國際研討會的經驗，這是在碩士班研究期間很難得的經驗，即使因此有了一些小成果，都是因為老師的提拔以及指導。另一方面，老師更是時常與我們分享生活的態度以及人生的經驗，這些寶貴的經驗是即使離開了實驗室，也一生受用無窮的。還要好好感謝口試委員吳季珍老師和陳學禮老師，除了平時實驗上給予我幫助，口試時也給了我許多寶貴的意見。

接著我要感謝所有曾經幫助過我的人，首先感謝林雲躍學長對我的指導，更在我實驗迷失方向的時候，給我一些建議。感謝林志誠學長在最一開始的時候，帶領著我成長氧化鋅，並且介紹實驗室一些基本儀器的使用方法。感謝李紹先學長在量測上的幫忙，還有其他一切事務的大力相助。除此之外，感謝王迪彥學長葉雲傑學長、朱叢鴻學長、莊家豪學長、曾云亨學長、謝孟翔學長以及王瑜、何柏勳、楊雅婷、紹騰緯、鍾怡萱等學弟妹們，一路上給我的協助與鼓勵，以及在實驗室事務上各種大小事的幫忙。更感謝杜昆樺一直以來的陪伴，在這些日子中給予了我許許多多的幫助。

最後我要感謝我的家人一直以來的支持和信任，給予了我很大的空間，因為他們，我才能有我現在這樣的成就。

摘要

本研究主要是探討一種倒置結構之有機太陽能電池，此倒置結構之元件，擁有氧化鋅薄膜作為一個電子傳輸層，鍍上P3HT:PCBM作為光反應層，並利用PEDOT:PSS當作電洞傳輸層，最後蒸鍍上銀電極。相對於傳統式的有機太陽能電池，倒置結構使用功函數較高的電極，移除了原本較低功函數容易產生氧化的鋁電極，可以有效地提升有機太陽能電池的壽命。本文中探討了紫外光對於氧化鋅電子傳輸層產生的效應，以及對倒置太陽能電池元件效率的影響，並量測電子電洞的結合效率。此外，我們還介紹了使用石墨烯氧化物以及石墨烯在倒置有機太陽能電池中作為一個電洞傳輸層，取代了傳統的PEDOT:PSS，並且展現了不錯的效率。最後，我們利用熱脫膠轉印的方式，作出了一個以石墨烯為上電極，石墨烯氧化物為電洞傳輸層而氧化銦錫作為下電極的半透明式倒置有機太陽能電池。為了達到更高的效率，我們改善了原本的製程，減少石墨烯層與層之間的殘留物，使得效率提升到約莫2.5%。此外，利用兩邊電極皆為透光的特性，可以利用一面反射鏡，對元件進行兩面照光，使得光電流有進一步的提升。

Abstract

In this study, we demonstrated an inverted polymer solar cell which has ZnO thin film as an electron transport layer, P3HT:PCBM as an active layer, PEDOT:PSS as a hole transport layer, and silver as the top electrode. Compared to the conventional devices, because of the high work-function metal electrode, inverted PSCs are more air-stable. In the following chapter, the UV effect on ZnO electron transport layer and the impact to device performance were investigated. Then, the using of graphene and graphene oxide to substitute for PEDOT:PSS as a hole transport layer was introduced. J-V characteristics were investigated to compare the device performance of the devices with different hole transport layers. Finally, we constructed a novel structure with graphene as a top electrode, graphene oxide as a hole transport layer and ITO as a bottom electrode. Because of the two transparent electrodes, this device is semitransparent, and a modified-transferring process was introduced for further improvement of the device performance.

Contents

口試委員審定書 ..... **I**

Acknowledgements ..... **II**

摘要 ..... **III**

Abstract ..... **IV**

Contents ..... **V**

List of Figures ..... **VIII**

List of Tables ..... **XII**

List of Publications ..... **XIII**

Chapter 1 Introduction **1**

1.1 Introduction **2**

1.2 Polymer solar cells **4**

1.2.1 Conventional type 6

1.2.2 Inverted type 7

1.3 Components of inverted organic solar cells **9**

1.3.1 Photoactive layer 9

1.3.2 Electron transport layer 10

1.3.3 Hole transport layer 11

1.3.4 Electrode 12

1.4 Reference **13**

Chapter 2 Experimental Setup **15**

2.1 Solar cell characteristics **16**

2.1.1 Solar spectrum (I-V curve) 16

2.1.2 External quantum efficiency (EQE) 18

2.2 UV-Visible absorption spectroscopy 19

2.3 AFM measurement..... 20

2.4 Transient Photovoltage(TPV) 23

2.5 Raman spectroscopy..... 25

Chapter 3 UV sensitive electron transport layer in inverted polymer solar cell 27

3.1 Inverted polymer solar cell..... 28

3.1.1 Preparation of ZnO thin film for electron transport layer 29

3.1.2 Fabrication of inverted type polymer solar cell.....30

3.2 Suppression of recombination by UV illumination 32

3.2.1 Device performance due to UV effect 32

3.2.2 Discussion and Transport properties 35

3.3 Reference..... 39

Chapter 4 Using Graphene and Graphene oxide as a hole transport layer for inverted type PSCs 41

4.1 Graphene oxide (GO)..... 42

4.1.1 Synthesis of graphene oxide.....43

4.1.2 Characterization of graphene oxide.....45

4.1.3 Fabrication of inverted devices with GO as a hole transport layer 49

4.1.4 Device performance and discussion 52

4.2 Graphene..... 54

4.2.1 Synthesis of graphene.....55

4.2.2 P-doped graphene due to adsorption of H_2O and O_2 in air.....56

4.2.3 Experimental step 58

4.2.4 Device performance and discussion 59

4.3 Reference 64

Chapter 5 Bifacial semitransparent inverted OPV with graphene/GO top electrode 66

5.1 Introduction 67

5.1.1 Graphene electrode 67

5.1.2 Semitransparent solar cell.....68

5.2 Characterization of graphene..... 69

5.3 Lamination process for graphene top electrode 72

5.3.1 Thermal release transferring method 72

5.3.2 Device characterization 73

5.3.3 Device performance.....76

5.4 Modification of the lamination process 82

5.4.1 Thermal release tape with multilayer graphene.....82

5.4.2 Layer dependent of graphene 87

5.4.3 Bifacial polymer solar cell.....89

5.4.4 Electrical property 92

5.5 Refernece..... 94

Chapter 6 Conclusions 96

6.1 Conclusions 96

List of Figures

Figure 1.1 Selected renewable energy indicators 3
Figure 1.2 2008 worldwide renewable-energy sources. Source: REN21 3
Figure 1.3 The schematic shows the effect of morphology to transport properties in polymer solar cells 5
Figure 1.4 Device architecture of a conventional polymer solar cell 6
Figure 1.5 Rapid degradation of conventional OSCs exposed to air.[8] 7
Figure 1.6 Device architecture of an inverted polymer solar cell 8
Figure 1.7 Device performance of unencapsulated conventional and inverted solar cells stored 40 days in air under ambient conditions. (a) Normalized PCE, (b) short-circuit current density (J_{sc}), (c) open-circuit voltage, and (d) FF 8
Figure 1.8 Schematic illustrations of the light absorption and excitons generation step from incident light in an organic donor-acceptor heterojunction 9
Figure 1.9 Energy level diagrams of device components referenced to the vacuum level. (a) Typical P3HT:PCBM BHJ OPV with a PEDOT:PSS hole transport layer. (b) With NiO as a hole transport layer. The published valence band, conduction band, and the Fermi level energies of NiO are shown.[18] 11
Figure 2.1 Solar radiation spectrum 16
Figure 2.2 The path length of the solar radiation through the Earth's atmosphere in units of Air Mass (AM) increases with the angle from the zenith. 17
Figure 2.3 External quantum efficiency (EQE) system setup 18
Figure 2.4 Schematic illustration of absorption spectroscopy set-up 19
Figure 2.5 Feedback loop controlled scanning of the sample topography for tapping mode. 21
Figure 2.6 (a) schematic of a band diagram in transient photovoltage setup (b) a typical transient photovoltage decay curve. 24
Figure 2.7 Schematic of energy level diagram related to Raman scattering. 26
Figure 3.1 The flow chart shows the procedure for preparing ZnO films. 29
Figure 3.2 SEM image of the ZnO thin film deposited by sol-gel method. 30
Figure 3.3 The cross-sectional SEM image of the device structure of the ITO/ZnO/P3HT:PCBM/PEDOT:PSS/Ag. 31
Figure 3.4 Schematic of the installation to illuminate the device by a solar simulator with a UV filter 32
Figure 3.5 Current-voltage characteristics of inverted type polymer solar cell with and without an UV filter during illumination. 33
Figure 3.6 Current-voltage characteristics of conventional polymer solar cell with and without an UV filter during illumination. 34

Figure 3.7 Space-charge accumulation in semiconductor devices.[24] 35
Figure 3.8 Charge recombination rate at Voc in different light intensity determined by TPV measurement. 37
Figure 3.9 Recombination mechanism of inverted polymer solar cell with ZnO as an electron transport layer without UV exposure 37
Figure 4.1 Thin films of solution-processed GO, Photographs of GO thin films on filtration membrane (a), glass (b) and plastic (c) substrates[6] 42
Figure 4.2 The flow chart shows the procedure for preparing graphene oxide. 44
Figure 4.3 (a) TEM image of as-prepared GO sheet on a lacey carbon support. (b) SAED pattern; the diffraction spots are labeled with MillerBravais indices. (c) Relative intensity profile obtained from the diffraction pattern in (b). .. 45
Figure 4.4 The AFM height image of a GO sheet on Si substrate and the corresponding height profile. 46
Figure 4.5 AFM height images of GO thin films with thicknesses of approximately (a) 2 nm, (b) 4 nm, and (c) 10 nm. Spin-coated from aqueous solution. 47
Figure 4.6 Tauc plot measurement obtained from the absorption spectrum of GO..... 48
Figure 4.7 The HOMO level of GO determined by Riken Keiki AC-2 photoionization measurement. 48
Figure 4.8 Energy level diagrams of the bottom electrode ITO, interlayer materials (ZnO), P3HT (donor), and PCBM (acceptor), interlayer materials (GO) and the top electrode Ag. 49
Figure 4.9 AFM height images of GO thin films spin-coated on a wafer from mixed solvent. From (a) to (c) shows the morphology of GO thin film using different concentration of GO solution which are 2mg/ml, 2.5mg/ml and 5mg/ml respectively. 50
Figure 4.10 Current-voltage characteristics of the inverted polymer solar cells consisting of various concentration of graphene oxide as a hole transport layer (A.M. 1.5 illumination, 100 mW cm^{-2}). 51
Figure 4.11 Current-voltage characteristics of the inverted polymer solar cells consisting of PEDOT:PSS and GO as a hole transport layer.(A.M. 1.5 illumination, 100 mW cm^{-2}). The device performance of the device without HTL was also shown. 53
Figure 4.12 Photograph of a 50-mm aperture partially covered by graphene and its bilayer. The line scan profile shows the intensity of transmitted white light along the yellow line. 54
Figure 4.13 The Raman spectra of graphene before and after vacuum annealing and exposed to air ambient. The numbers above each indicate the peak wavenumber and bandwidth.[28] 57
Figure 4.14 The doping process of SLG. Graphene sample is heated to 500 ◦C in

vacuum (step 1), and cooled down to room temperature (step 2), then exposed to air ambient (step 3). To check the stability, sample is introduced into vacuum for 2 h (step 4). It is then heated again to 500 ◦C (step 5) and cooled down (step 6), exposed to air ambient (step 7). The sample is checked after leaving in air for 15 days (step 8).[28] 57
Figure 4.15 Device architecture of an inverted polymer solar cell with a single layer graphene as a hole transport layer 58
Figure 4.16 Electrical properties of SLG with and without oxygen doping. 59
Figure 4.17 AFM image of graphene deposited on a glass substrate. 60
Figure 4.18 (a)(b) The current density–voltage (J-V) characteristics of inverted polymer solar cells (a) without graphene HTL and (b) with graphene HTL using different top metal electrodes. 61
Figure 4.19 Current-voltage characteristics of the inverted polymer solar cells consisting of PEDOT:PSS, GO and Graphene as a hole transport layer.(A.M. 1.5 illumination, 100 mW cm^{-2}). The device performance of the device without HTL was also shown. 62
Figure 5.1 A semitransparent inverted polymer solar cell with a structure of ITO/ZnO/P3HT:PCBM/ graphene oxide (GO)/graphene top electrode. 69
Figure 5.2 Raman spectroscopy of the graphene films consisting of one, two and three layers on glass substrates. 70
Figure 5.3 The transmittance of the graphene films on glass substrates consisting of various numbers of layers. 71
Figure 5.4 The sheet resistance of the graphene films on glass substrates consisting of various numbers of layers. 71
Figure 5.5 Fabrication of the ITO/ZnO/P3HT:PCBM/GO device before depositing the top electrode (Step A). Top lamination processes of graphene electrodes by the graphene film transferring (Step B) and thermal annealing/releasing processes (Step, C)..... 72
Figure 5.6 The cross-sectional SEM image of the device structure of ITO/ZnO/P3HT:PCBM/GO/graphene top electrode (6 layers)..... 74
Figure 5.7 (a) and (b) the morphological AFM image of the device structure of the ITO/ZnO/P3HT:PCBM/GO/graphene top electrode (1 layer) and (6 layers). 74
Figure 5.8 The transmittance of this semitransparent polymer solar cell. The picture of the semitransparent device was shown in the inset. 75
Figure 5.9 Current-voltage characteristics of the semitransparent polymer solar cells with light shining from the ITO side or the graphene side respectively and a standard cell with Ag electrode is also shown. (A.M. 1.5 illumination, 100 mW cm^{-2}). 76

Figure 5.10 EQEs of the standard cell and semitransparent cell consisting of eight layers of graphene as illuminated from the ITO side and the graphene side. 77
Figure 5.11 (a) and (b) The power flux distributions of incident light at the wavelength of 550nm and 400 nm inside the semitransparent device as illuminated from ITO side and graphene side respectively using the 3D-FDTD simulation.. 79
Figure 5.12 Optical reflection spectra of the semitransparent devices when illuminated from the ITO side and the graphene side. 81
Figure 5.14 Current-voltage characteristics of the semitransparent polymer solar cells using the modified transferring method with light shining from the ITO side or the graphene side respectively and a standard cell with Ag electrode is also shown. (A.M. 1.5 illumination, 100 mWcm^{-2}). 84
Figure 5.15 EQEs of the standard cell and semitransparent cell using the modified transferring process consisting of eight layers of graphene as illuminated from the ITO side and the graphene side 86
Figure 5.16 (a) and (b) Current-voltage characteristics of the semitransparent polymer solar cells consisting of various number of top graphene layers with light shining from the ITO side or the graphene side respectively (A.M. 1.5 illumination, 100 mW cm^{-2}). 88
Figure 5.17 The device performances of the standard cell and semitransparent cell using modified transferring method consisting of eight layers of graphene as illuminated from the ITO side and the graphene side. The device performance of the bifacial device illuminated from both sides is also shown. 91
Figure 5.18 The power flux distributions of incident light inside the semitransparent device as illuminated from two respective sides using the 3D-FDTD simulation. 91
Figure 5.19 Dark current-voltage characteristics of the standard cell and the semitransparent cell (8 layers) on a semi-logarithmic scale. 92
Figure 5.20 The transient photovoltage (TPV) decay curves of the standard cell and the semitransparent cell measured from two different illuminating directions. Devices were illuminated by white light with a power intensity of 50 mW cm^{-2}. 93

List of Tables

Table 4.1 Summaries of the device performances of the inverted polymer solar cells under illumination (A.M.1.5, 100 mW cm^{-2}) using different concentration of graphene oxide as a hole transport layer. 51

Table 4.2 Summaries of the device performances of the inverted polymer solar cells under illumination (A.M.1.5, 100 mW cm^{-2}) using PEDOT:PSS and GO as a hole transport layer. The device performance of the device without HTL was also shown. 53

Table 4.3 Summaries of the device performances of the inverted polymer solar cells under illumination (A.M.1.5, 100 mW cm^{-2}) using PEDOT:PSS, GO and Graphene as a hole transport layer. The device performance of the device without HTL was also shown. 63

Table 5.1 Summaries of the device performances of the semitransparent polymer solar cells under illumination (A.M.1.5, 100 mW cm^{-2}) from the ITO side and the graphene side. The device performance of the referenced standard opaque device was also shown. 77

Table 5.2 Summaries of the device performances of the semitransparent polymer solar cells under illumination (A.M.1.5, 100 mW cm^{-2}) using the modified transferring method and the old method (parenthesis). The device performance of the referenced standard opaque device was also shown. 84

Table5.3 Summaries of the device performances of the semitransparent polymer solar cells under illumination (A.M.1.5, 100 mW cm^{-2}) from the ITO side and the graphene side (parenthesis). The device performance of the referenced standard opaque device was also shown. 89

List of Publications

期刊論文(Journal paper)

1. **Yu-Ying Lee**, Kun-Hua Tu, Chen-Chieh Yu, Shao-Sian Li, Jeong-Yuan Huang, Chih-Cheng Lin, Kuei-Hsien Chen, Li-Chyong Chen, Hsuen-Li Chen, and Chun-Wei Chen*, Top Laminated Graphene Electrode in a Semitransparent Polymer Solar Cell by Simultaneous Thermal Annealing/Releasing Method, *ACS Nano*, in press (2011). **(SCI, impact factor 9.855)**
2. Yun-Yue Lin, **Yu-Ying Lee**, Liu-Wen Chang, Jih-Jen Wu and Chun-Wei Chen*, The influence of interface modifier on the performance of nanostructured ZnO/polymer hybrid solar cells, *Applied Physics Letters*, **94**, 063308 (2009). **(SCI, impact factor 3.820)**

研討會論文(Conference paper)

1. **Yu-Ying Lee**, Kun-Hua Tu, Jeong-Yuan Huang, Kuei-Hsien Chen and Li-Chyong Chen and Chun-Wei Chen*, Ultra Thin Graphene-Based Platform for the Optoelectronic and Photovoltaic Applications, **MRS spring 2011**, San Francisco, USA. **(Best Symposium Oral Presentation Award).**
2. **Yu-Ying Lee,** Yun-Yue Lin, Jih-Jen Wu, and Chun-Wei Chen*, Enhanced Carrier Transport in Vertical Oriented ZnO Nanorod/Polymer Hybrid Photovoltaic Devices, **PVSEC-19**, Jeju, South Korea. **(Best Paper Award).**
3. Yun-Yue Lin, **Yu-Ying Lee**, Wei-Fang Su and Chun-Wei Chen*, High Speed Response Organic Diode and Photodetector Application by Low Temperature Solution Process, **IUMRS-ICA 2008**, Nagoya, Japan. **(IUMRS Outstanding Work Award)**.

1

Introduction

Abstract

The global energy requirement continues to grow up gradually in these years. It's important to find out a way to generate energy without producing greenhouse gases which would result in global warming. Solar energy is a kind of renewable energy comes from natural sources, and it is naturally replenished without any pollution. Polymer solar cells (PSCs) based on a blend of conjugated polymers and fullerenes have attracted much attention because of their light weight, low cost, and promising applications in the future. However, the stability of PSCs is a critical issue for commercial applications. Therefore, an alternative type of a so-called inverted device architecture where the anode and cathode is reversed has been come up. We illustrate the components of the inverted devices and show the difference between the inverted PSCs and the conventional one.

1.1 Introduction

Global oil, the main energy source in the world, is estimated to last for only 40-50 years. Natural gas, uranium and coal reserves also have their limitation. However, the global energy requirement continues to grow up gradually in these years. In addition, the fossil oil burning will generate too much carbon dioxide (CO_2) and other greenhouse gases, which is the main reason resulting in global warning.[1] To diminish the pollution and to look for sustainable energy, scientists and engineers in the world are all eager to find a new alternative clean energy.

Renewable energy is energy which comes from natural resources such as sunlight, wind, rain, tides, and geothermal heat, which are naturally replenished. Compared to the conventional fossil oil, it is cleaner and could be renewed naturally. During the five-years from the end of 2004 through 2009, worldwide renewable energy capacity grew at rates of 10–60 percent annually for many technologies. Grid-connected PV increased the fastest of all renewables technologies, with a 60-percent annual average growth rate for the five-year period. Utilizing the power of the sun is one of the most viable ways to solve the foreseeable world's energy crisis.

Selected global indicators	2007	2008	2009
Investment in new renewable capacity (annual)	104	130	150 billion USD
Existing renewables power capacity, including large-scale hydro	1,070	1,140	1,230 GWe
Existing renewables power capacity, excluding large hydro	240	280	305 GWe
Wind power capacity (existing)	94	121	159 GWe
Solar PV capacity (grid-connected)	7.6	13.5	21 GWe
Solar hot water capacity	126	149	180 GWth
Ethanol production (annual)	50	69	76 billion liters
Biodiesel production (annual)	10	15	17 billion liters
Countries with policy targets for renewable energy use	68	75	85

Figure 1.1 Selected renewable energy indicators

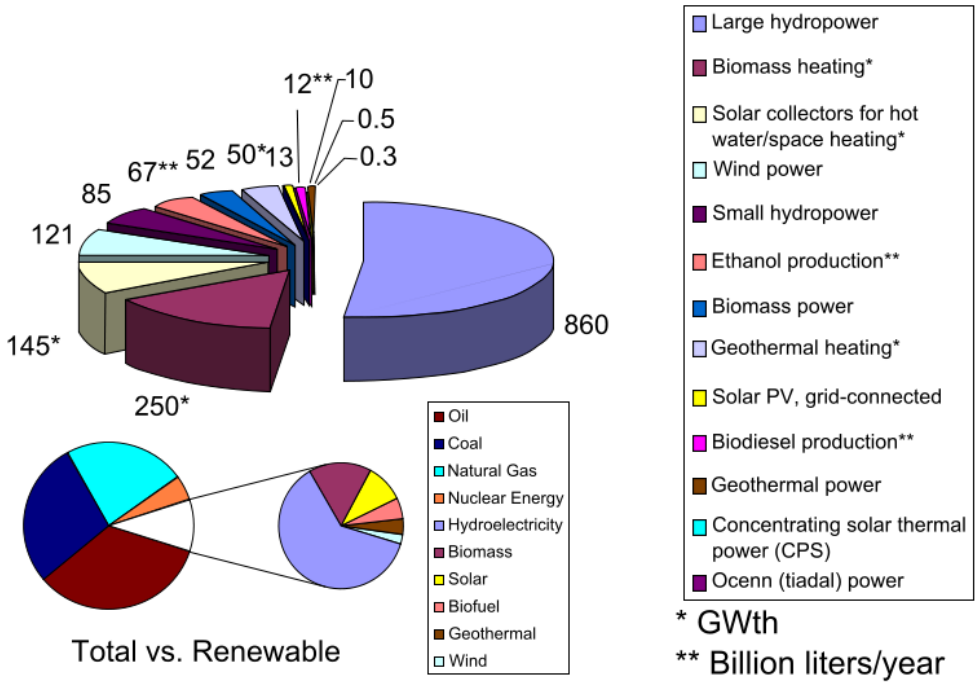

Figure 1.2 2008 worldwide renewable-energy sources. Source: REN21

1.2 Polymer solar cells

Solar cells based on inorganic materials such as Si and GaAs have been developed for over 50 years and reached high efficiency. However, the high cost and the confinement of this technology to niches have limited their widespread use as a source of power.

Polymer solar cells have attracted considerable interest for fabricating low-cost, large-area, and mechanically flexible photovoltaic devices, though the efficiency is still low compared to that of conventional inorganic counterparts. To be the next-generation renewable energy source, it's necessary to improve the energy conversion efficiency. The donor-acceptor heterojunction formed from a blend of a conjugated polymer with a fullerene derivative represents one of the most promising systems. Compared to inorganic systems, in which photon absorption directly produces free electrons and holes,[2] optical absorption in organic molecular and polymer semiconductors mainly creates electron-hole pairs (excitons) that are bound at room temperature.

In general, illumination of an organic semiconductor leads to the creation of excitons[3] with a binding energy of about 0.4 eV[4,5] , instead of free charges. The exciton can be separated when it reaches the interface between suited donor (D) and acceptor (A) materials, where the difference in the electron affinities and the ionization potentials between those two (A and D) materials are sufficiently large to overcome the exciton binding energy. Subsequent transport and collection of the photo-induced charges at the appropriate electrodes then provides the photovoltaic effect. Morphology manipulation of the photoactive layer is thus a key point to improve the device performance of polymer solar cells as shown in Figure 1.3.

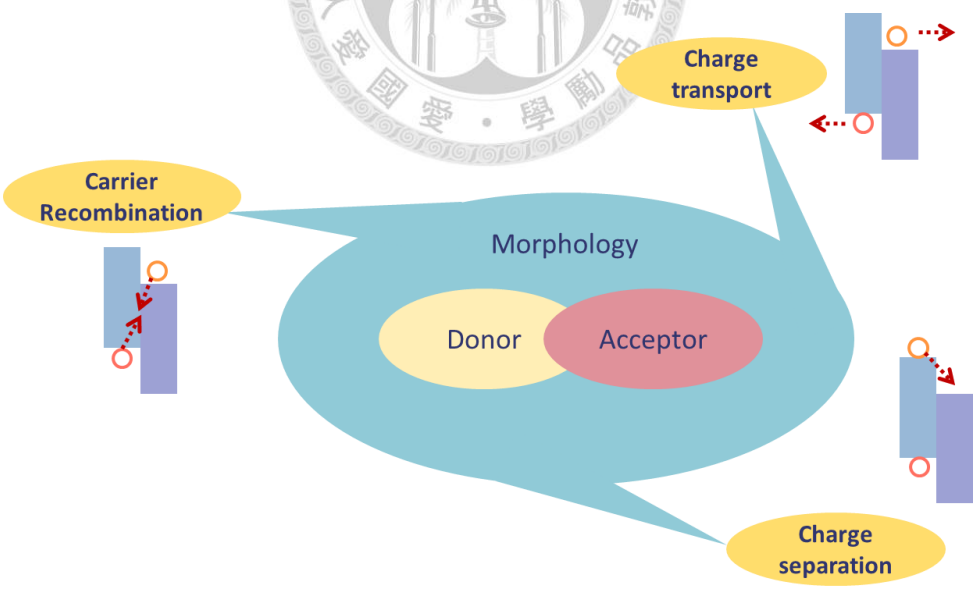

Figure 1.3 The schematic shows the effect of morphology to transport properties in polymer solar cells

1.2.1 Conventional type

Conventional polymer solar cells (PSCs) generally comprise a transparent metal oxide anode, such as indium tin oxide (ITO) with a thin hole transport layer (HTL) of conductive PEDOT:PSS to increase its work function for effective hole collection, a photoactive layer consisting of an electron donor and an electron acceptor, and a low work function metal such as Al as the cathode.[6,7] The device structure consisting of ITO/PEDOT:PSS/P3HT:PCBM/Al is shown in Figure 1.4.

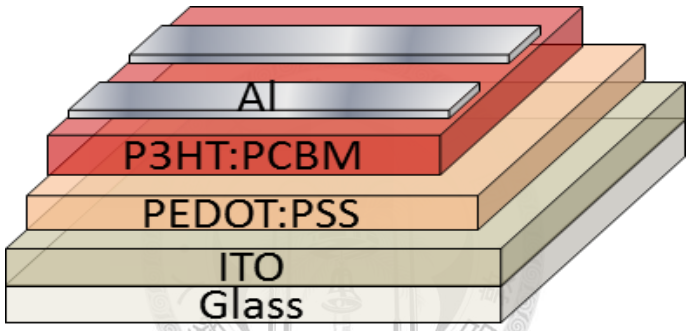

Figure 1.4 Device architecture of a conventional polymer solar cell

However, several components of conventional devices are highly sensitive to moisture and air. For example, PEDOT:PSS is hygroscopic which would absorb water and further reduce the conductivity of the buffer layer.[8] Moreover, the low work function cathode is also easily oxidized when exposed to air. The oxidation leads to the formation of an insulating barrier resulting in the increase of the serial resistance in the devices and further causes the degradation of the device performance[9] as shown in Figure 1.5. Exposing conventional devices to air for a day can almost lead to complete failure of the device.

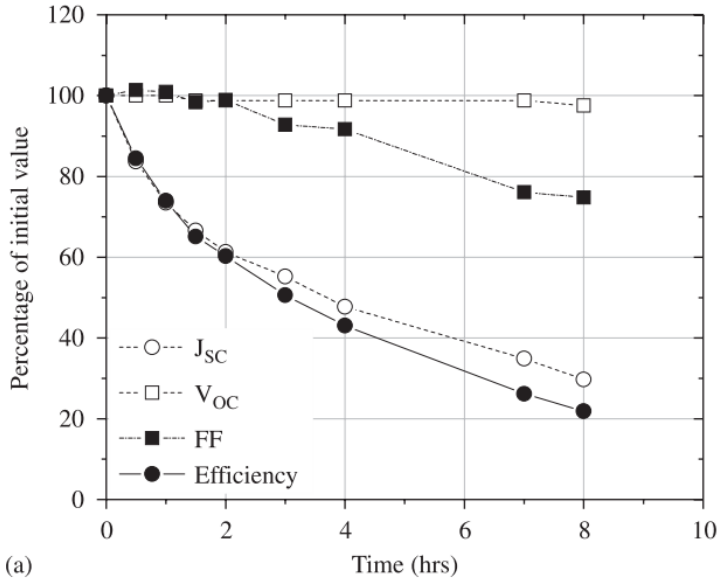

Figure 1.5 Rapid degradation of conventional PSCs exposed to air.[8]

1.2.2 Inverted type

To overcome the rapid oxidation of the Al top electrode which causes the instability and degrading of device performance, an alternative type of a so-called inverted device architecture where the anode and cathode is reversed has attracted great attention as shown in Figure 1.6. The inverted structure is implemented by inserting an electron transporting/ hole blocking layer (such as titanium dioxide, TiO_2, or zinc oxide, ZnO) between ITO and the active layer to selectively collect electrons, while a more air-stable, high work function metal is used as the top electrode for hole collection.[10] A hole transporting/electron blocking buffer layer can also be inserted between the BHJ layer and the high-work-function metal electrode to facilitate efficient hole collecting. Figure 1.7 shows the comparison of the air stability between conventional type and inverted type PSCs.

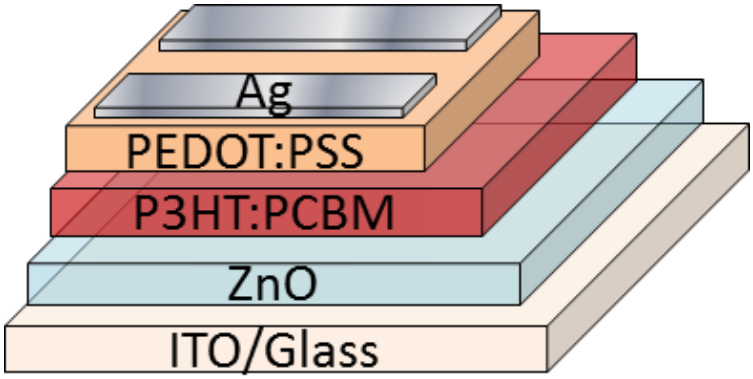

Figure 1.6 Device architecture of an inverted polymer solar cell

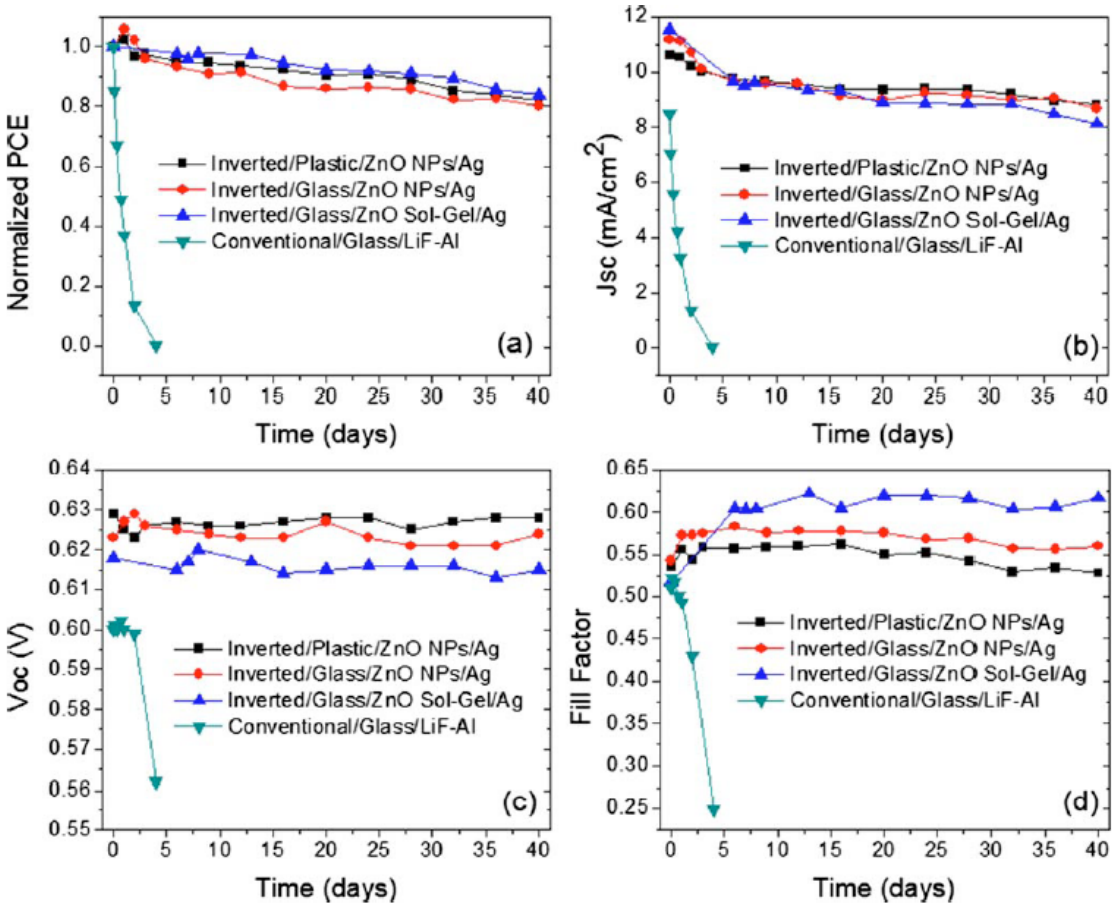

Figure 1.7 Device performance of unencapsulated conventional and inverted solar cells stored 40 days in air under ambient conditions. (a) Normalized PCE, (b) short-circuit current density (J_{sc}), (c) open-circuit voltage, and (d) FF[11]

1.3 Components of inverted organic solar cells

1.3.1 Photoactive layer

The photoactive layer in the organic solar cells plays an important role to absorb the incident light and produce photo-generated current. To create driving force for charge separation, a suitable energy level alignment between the donor and acceptor is necessary. Figure 1.8 shows the typical conjugated polymer absorption region. A large ratio of interfacial area to volume is the prerequisite for charge dissociation. According to the experimental results and simulation techniques, a bicontinuous pathway must be formed for the photo-generated holes and electrons to reach their respective contacts for efficient collection.[12,13]

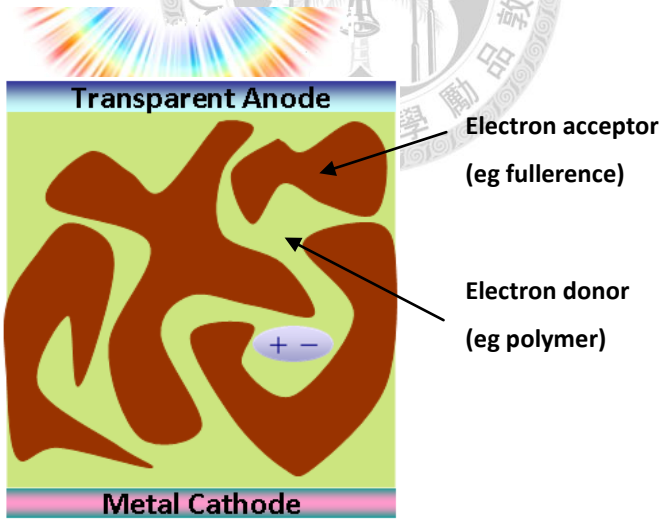

Figure 1.8 Schematic illustrations of the light absorption and excitons generation step from incident light in an organic donor-acceptor heterojunction

1.3.2 Electron transport layer

Recently, TiO_2 and ZnO thin films have been explored as electron selecting layers for inverted solar cells. The Fermi level of ZnO (4.3 eV) matches well with the LUMO of PCBM (4.3 eV), which facilitates efficient electron transfer and extraction from the polymer : fullerene blend, and the low-lying valence band of ZnO can also prevent hole carriers in the BHJ from reaching the cathode. Waldauf et al. have demonstrated that inverted solar cells can be fabricated by using a thin (10 nm) sol-gel-processed titanium suboxide (TiO_x) layer as the electron selecting layer on ITO.[14] Alkali metal salts also could be used as an interfacial modifier to tune the work function of ITO for electron collection. Among different metal salts that have been studied, cesium carbonate (Cs_2CO_3) has been found to be the most promising modifier to reduce the work function of ITO.[15,16] The PCE of inverted solar cells based on solution-processed Cs_2CO_3 could reach as high as 4.2%.

1.3.3 Hole transport layer

The most widely used hole transport layer (HTL) in organic solar cells is poly(ethylenedioxythiophene):poly(styrene sulfonate) (PEDOT:PSS), which is a kind of conducting polymer. However, its electrical inhomogeneity[17] limits the capability for electron blocking,[18] and its acidic nature is another drawback for device chemical stability. These promote the development for better HTLs.

NiO, a p-type oxide semiconductor, has been demonstrated to replace PEDOT:PSS as a HTL in organic solar cells as shown in Figure 1.9 and showed a dramatic performance increase with an excellent device stability.[19] Several inorganic materials such as V_2O_5 and MoO_3[20] are also promising choices for HTLs. However, the high vacuum deposition of these inorganic materials is incompatible with solution-processable and printable advantages of OPVs. Therefore, researchers are working hard on seeking an alternative HTL which is useful and also solution-processable.

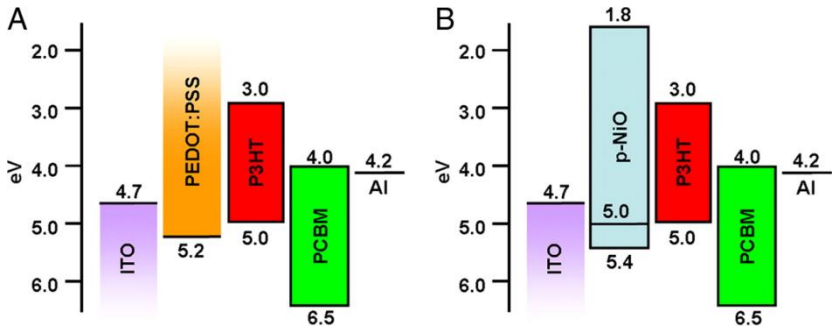

Figure 1.9 Energy level diagrams of device components referenced to the vacuum level. (a) Typical P3HT:PCBM BHJ OPV with a PEDOT:PSS hole transport layer. (b) With NiO as a hole transport layer. The published valence band, conduction band, and the Fermi level energies of NiO are shown.[19]

1.3.4 Electrode

Indium tin oxide (ITO) is commonly used in different photoelectronic devices for transparent electrodes. It has low sheet resistance and high optical transparency which are the most necessary properties for electronic applications. Nevertheless, due to the dwindling supplies of indium, the price of ITO is increasing constantly.

To satisfy future demand and to reduce costs, Aluminum doped ZnO (AZO) has emerged as an attractive alternative transparent conduction oxide (TCO) for photoelectronic devices.[21,22] The electrical and optical properties of AZO are comparable to those of ITO, and the most importance is that it's inexpensive, nontoxic and abundant materials. AZO layers could be prepared by various techniques such as magnetron sputtering and PLD. Furthermore, to meet the thirst for flexibility and large-area production, some carbon based materials are also in developing for transparent electrodes.

1.4 Reference

[1] Energy Information administration, official energy statics from U.S. government

[2] Bube, R. H. Photoelectronic Properties of Semiconductors; Cambridge University Press: Cambridge, **1992**.

[3] M. Pope, C. E. Swenberg, Electronic Processes in Organic Crystals and Polymers, 2nd ed., Oxford University Press, New York **1999**.

[4] S. Barth, H. Bässler, *Phys. Rev. Lett.* **1997**, *79*, 4445.

[5] P. G. Dacosta, E. M. Conwell, *Phys. Rev. B* **1993**, *48*, 1993.

[6] A. J. Morfa, K. L. Rowlen, T. H. Reilly, M. J. Romero, and J. Lagemaat, *Appl. Phys. Lett.* **2008**, *92*, 013504.

[7] L. Li, G. Lu, and X. Yang, *J. Mater. Chem.* **2008**, *18*, 1984.

[8] K. Kawano, R. Pacios, D. Poplavskyy, J. Nelson, D. D. C. Bradley, and J. R. Durrant, *Sol. Energy Mater. Sol. Cells* **2006**, *90*, 3520.

[9] M. Jorgensen, K. Norrman, and F. C. Krebs, *Sol. Energy Mater. Sol. Cells* **2008**, *92*, 686.

[10] M. Glatthaar, M. Niggemann, B. Zimmermann, P. Lewer, M. Riede, A. Hinsch, J. Luther, *Thin Solid Films* **2005**, *491*, 298.

[11] S. K. Hau, H. L. Yip, N. S. Baek, J. Zou, K. O'Malley, A. K. Y. Jen, *Appl. Phys. Lett.* **2008**, *92*, 253301.

[12] B. Lei, Y. Yao, A. Kumar, Y. Yang, V. Ozolins, *J. Appl. Phys*. **2008**, *104*, 024504.

[13] P. Watkins, A. Walker, G. Verschoor, *Nano Lett*. **2005**, *5*, 1814.

[14] C. Waldauf, M. Morana, P. Denk, P. Schilinsky, K. Coakley, S. A. Choulis, C. J. Brabec, *Appl. Phys. Lett.* **2006**, *89*, 233517.

[15] J. S. Huang, G. Li, Y. Yang, *Adv. Mater*. **2008**, *20*, 415.

[16] H. H. Liao, L. M. Chen, Z. Xu, G. Li, Y. Yang, *Appl. Phys. Lett.* **2008**, *92*, 173303.

[17] L. S. C. Pingree, B. A. MacLeod, D. S. Ginger, *J. Phys. Chem. C* **2008**, *112*,7922.

[18] H. Yan, P. Lee, N. R. Armstrong, A. Graham, G. A. Evmenenko, P. Dutta, T. J. Marks, *J. Am. Chem. Soc*. **2005**, *127*, 3172.

[19] M. D. Irwin, B. Buchholz, A. W. Hains, R. P. H. Chang, T. J. Marks, *Proc. Natl. Acad. Sci. USA* **2008**, *105*, 2783.

[20] V. Shrotriya, G. Li, Y. Yao, C. W. Chu, Y. Yang, *Appl. Phys. Lett.* **2006**, *88*, 073508.

[21] Y. Tomita, C. May, M. Toerker, J. Amelung, M. Eritt, F. Loeffler, C. Luber, K. Leo, K. Walzer, K. Fehse, and Q. Huang, *Appl. Phys. Lett.* **2007**, *91*, 063510.

[22] K. Schulze, B. Maennig, K. Leo, Y. Tomita, C. May, J. Hüpkes, E. Brier, E. Reinold, and P. Bäuerle, *Appl. Phys. Lett.* **2007**, *91*, 073521.

2

Experimental Setup

Abstract

To investigate device performance and spectral response, we described how to use a solar simulation to analyze the device performance of solar cells and we have also constructed a system of external quantum efficiency (EQE). We used UV-Visible absorption spectroscopy to measure the transmittance of materials and we also investigated surface potential and morphology by AFM technique. Carrier transport behavior such as recombination rate in a working device was measured by transient photovoltage (TPV). Raman spectroscopy is a powerful technique for understanding molecular composition and structure of materials so we also used Raman spectroscopy to characterize graphene.

2.1 Solar cell characteristics

2.1.1 Solar spectrum (I-V curve)

Figure 2.1 shows the definition of the solar spectrum. Solar radiation closely matches a black body radiator at about 5,800 K. As it passes through the atmosphere, sunlight is attenuated by scattering and absorption; the more atmosphere through which it passes, the greater the attenuation. The air mass coefficient (AM) defines the direct optical path length through the Earth's atmosphere, expressed as a ratio relative to the path length vertically upwards.

$$AM = \frac{L}{L_0} = \frac{1}{\cos\theta} \tag{2.1}$$

where L_0 is the zenith path length (i.e. normal to the Earth's surface) at sea level

θ is the zenith angle in degrees

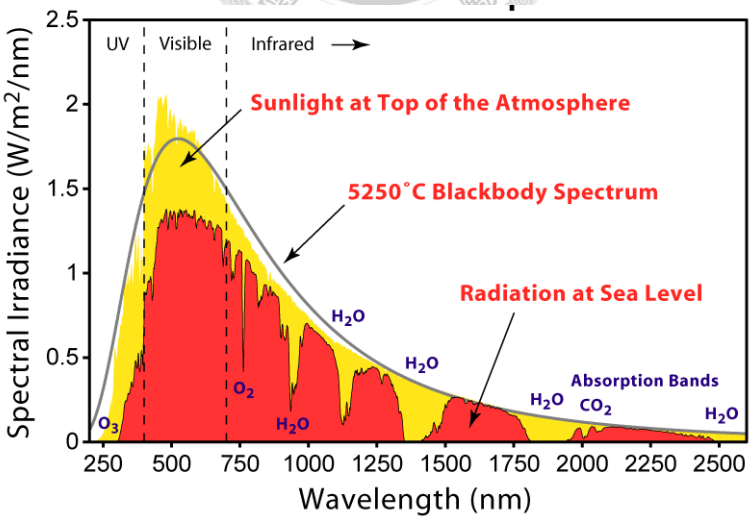

Figure 2.1 Solar radiation spectrum

The air mass coefficient can be used to characterize the solar spectrum after solar radiation has traveled through the atmosphere and is commonly used to represent the performance of solar cells under standardized conditions. It is often referred to using the syntax "AM" followed by a number. "AM1.5", 1.5 atmosphere thickness, corresponds to a solar zenith angle of θ=48.2°. While the summertime AM number for mid-latitudes during the middle parts of the day is less than 1.5, higher figures apply in the morning and evening and at other times of the year. Therefore AM1.5 is useful to represent the overall yearly average for mid-latitudes. Therefore, "AM1.5" is universal when characterizing terrestrial power-generating panels.

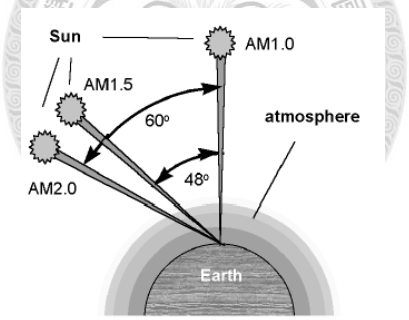

Figure 2.2 The path length of the solar radiation through the Earth's atmosphere in units of Air Mass (AM) increases with the angle from the zenith.

To analyze the device performance of solar cells, a Newport-Oriel solar simulator simulating AM 1.5 sun spectrum was used to illuminate from the transparent side of the device. Then, the I-V characteristics were recorded by keithley 2410 sourcemeter unit.

2.1.2 External quantum efficiency (EQE)

In this study the organic photoactive material spectral response is measured by in house built external quantum efficiency instrument. The lamp source is oriel 500W Xe-Hg light source, and we use Oriel cornerstone 1/4 monochromater. The measured spectral range is from 250 nm to 1100 nm. Optical power is calibrated by silicon diode. Figure 2.3 shows the instrument setup.

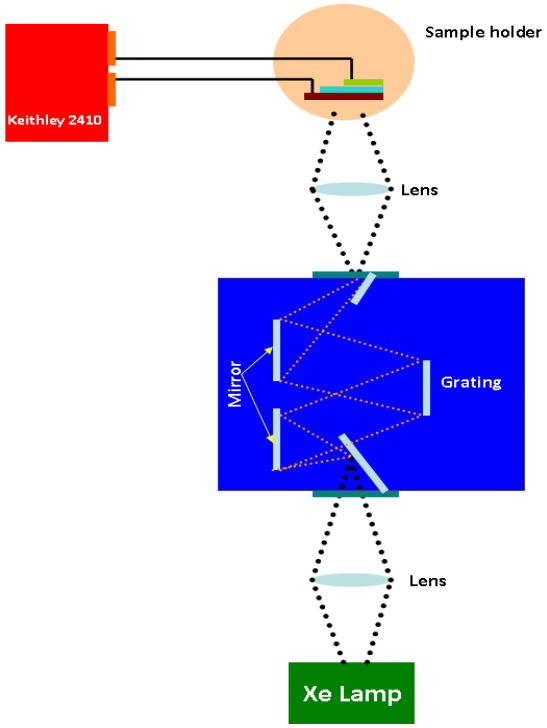

Figure 2.3 External quantum efficiency (EQE) system setup

2.2 UV-Visible absorption spectroscopy

The absorption spectra shown in this study were recorded by Jasco V570 UV-Visible System. Before the measurement, we correct the baseline to normalize the incident light. Then, the sample and the reference glass were put into each holder as illustrated in Figure 2.4.

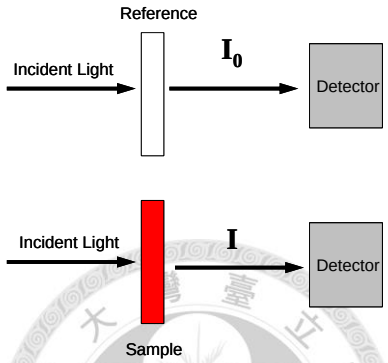

Figure 2.4 Schematic illustration of absorption spectroscopy setup

The absorbance (A) and transmittance (T) are defined as:

$$T = -\frac{I}{I_0} \tag{2.2}$$

$$A = -\log T = -\log\left(\frac{I}{I_0}\right) \tag{2.3}$$

where I and I_0 are the intensity of light at a certain wavelength passing through the sample and the reference, respectively. The absorption spectra were obtained by plotting A as a function of wavelength.

2.3 AFM measurement

The Atomic Force Microscope (AFM) is used to image the surface topography of a sample down to the sub-nanometer scale. The AFM however requires no conductivity; here tip sample interactions are based on mechanic short or long-range forces.

The basic setup of an AFM consists of a measuring unit, a controller and a computer, which is collecting the data, as shown in Figure 2.4. To accomplish a full image, the sample is scanned line-by-line over a rectangular area with typically some few hundred lines using a sharp tip. There are three basic measurement modes for the AFM: Contact mode, non-contact mode and tapping mode. The difference of which lies in the different tip sample interactions used to control a constant distance between tip and sample. In the contact mode the tip is touching the sample with a certain pressure, leading to a bending of the cantilever at which end the tip is mounted. Both the non-contact and tapping mode use extended tip sample interactions via van der Waals long-range forces over several nm distances.

For soft organic materials the tapping mode offers destruction less measurements at high resolutions. In the case of tapping or non-contact mode, a quartz piezo is used to excite the cantilever to oscillations. The amplitude of these oscillations is depending on the interactions with the sample surface and is basically the more damped the closer the tip approaches to the surface. To keep a constant distance to the surface, the feed back

loop maintains constant amplitude of the cantilever oscillation, which lies typically between 20 and 100 nm for the tapping mode and less for the non-contact mode. The amplitude is detected via a reflected laser spot unto a split photodiode detector, and the controller electronics applies a corresponding correction signal to the z-piezo of the scanner

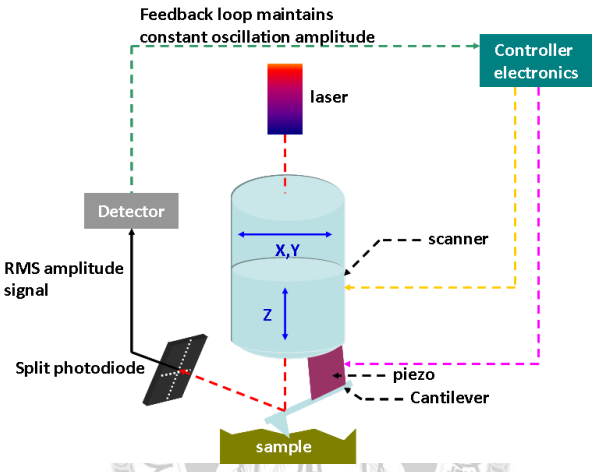

Figure 2.5 Feedback loop controlled scanning of the sample topography for tapping mode.

Kelvin Probe Force Microscopy (KPFM) applies the Kelvin Probe technique in combination with non-contact (NC) Atomic Force Microscopy (AFM) to determine local electronic work function of a sample. Similar to the tapping mode, the NC mode uses an oscillating cantilever for scanning over the sample surface. A constant distance between tip and sample surface is here controlled by a constant frequency shift from the resonance frequency, by which a damped oscillation is accompanied (compare: damped driven harmonic oscillator). Generally long-range interactions like van der Waals,

electrostatic and magnetic forces determine the tip sample interaction. Here the frequency shift is approximately proportional to the force gradient. Since no magnetic samples were investigated, the magnetic force will be omitted. For a tip radius of curvature of r, a Hamaker constant C_H between sample and tip, the van der Waals force (F_{vdW}) is calculated as

$$F_{vdW} = -\frac{C_H r}{6z^2{}_{min}} \tag{2.4}$$

With Z_{min} being the minimal tip-sample distance

If actually there is a voltage V applied between tip and sample, the resulting electrostatic force can be written as

$$F_{electrostatic} = -\frac{1}{2}\frac{\partial C}{\partial z}V^2 \tag{2.5}$$

where C denotes the capacitance and z the tip-sample distance

If two materials are brought into contact with each other, a contact potential U_{CP} between them will result from their difference in work functions (Φ1 – Φ2):

$$U_{CP} = -\frac{1}{e}(\Phi_1 - \Phi_2) = \frac{\Delta\Phi}{e} \tag{2.6}$$

Where e is the elementary charge and Φ_1, Φ_2 the work functions of these materials

2.4 Transient Photovoltage(TPV)

In this study, in order to quantify carrier recombination in organic photovoltaic devices, we have constructed a transient photovoltage system. In transient photovoltage measurement, the devices are held at a steady state open circuit voltage, the magnitude of which is adjusted by varying the intensity of a bias lamp, the setup schematics are shown in Figure 2.6(a). A pulsed light is then introduced to create a small perturbation to the open circuit voltage due to the transiently generated electron and hole carriers altering the quasi Fermi levels. At open circuit voltage, these additional carriers decay with the lifetime determined by the rate of charge carrier recombining across the heterojunction interface. A typical photovoltage transient curve is shown in Figure 2.6(b). The decay curve can be fitted to a monoexponential decay, from which a characteristics lifetime τ can be extracted. The effective recombination rate, K_{rec} is simply $1/\tau$. As quasi Fermi level approach the band edges or V_{oc} increases, the hole and electron concentration increase exponentially.

(a)

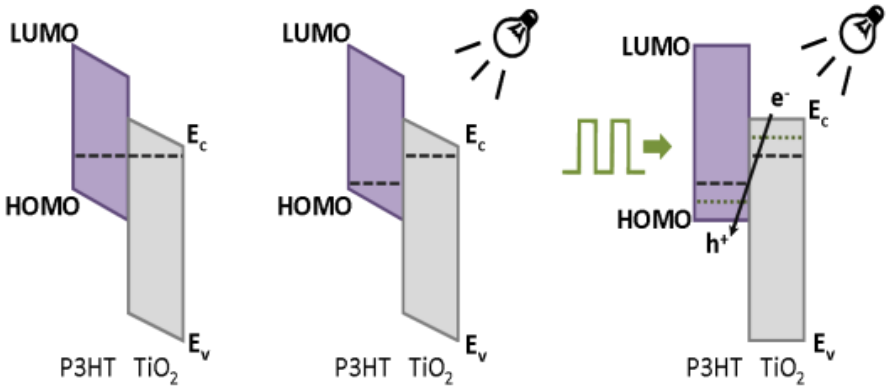

Energy band diagram of donor and acceptor under
(a).dark,
(b).illumination of bias lamp,
(c).illumination of bias lamp and pulse light, and applied open circuit voltage.

(b)

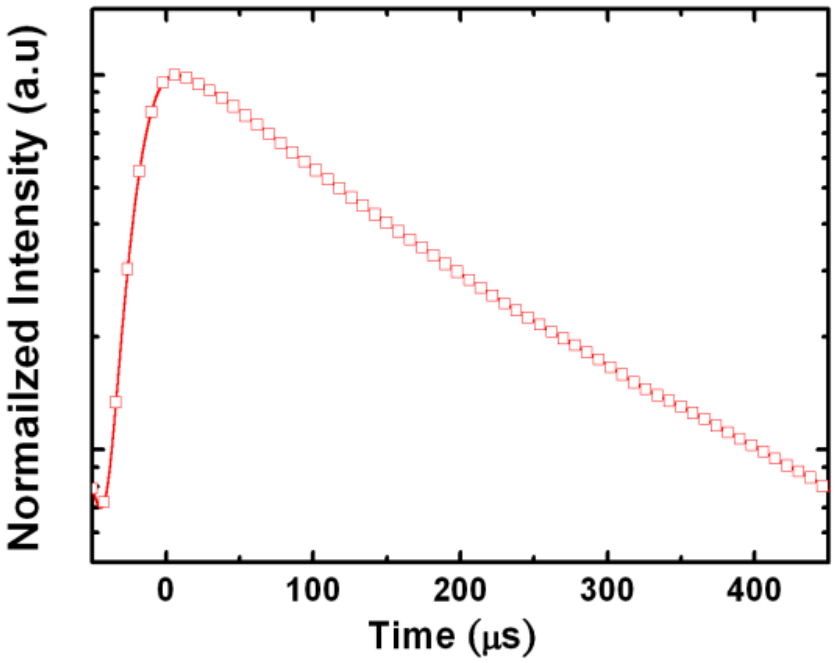

Figure 2.6 (a) schematic of a band diagram in transient photovoltage setup (b) a typical transient photovoltage decay curve.

2.5 Raman spectroscopy

Raman spectroscopy is a powerful technique for understanding molecular composition and structure of materials. The technique measures the wavelength and intensity of inelastic scattered light from the light from sample to obtain information about the rotational and vibrational modes of the material. Typically we use monochromatic light source to excite the molecule from the ground state to a virtual energy state. And when the molecule relaxes it emits a photon and it returns to a different rotational or vibrational state. The difference in energy between the original state and this new state leads to a shift in the emitted photon's frequency away from the excitation wavelength. If the emitted photon is less energetic than the incident photon, the resulted shift toward to lower frequency is designated as a Stokes shift. Inversely, if the emitted photon is more energetic than the incident photon, the resulted shift toward to higher frequency is designated as an Anti-Stokes shift. Figure 2.7 shows the related states of Raman signal in the energy level diagram.

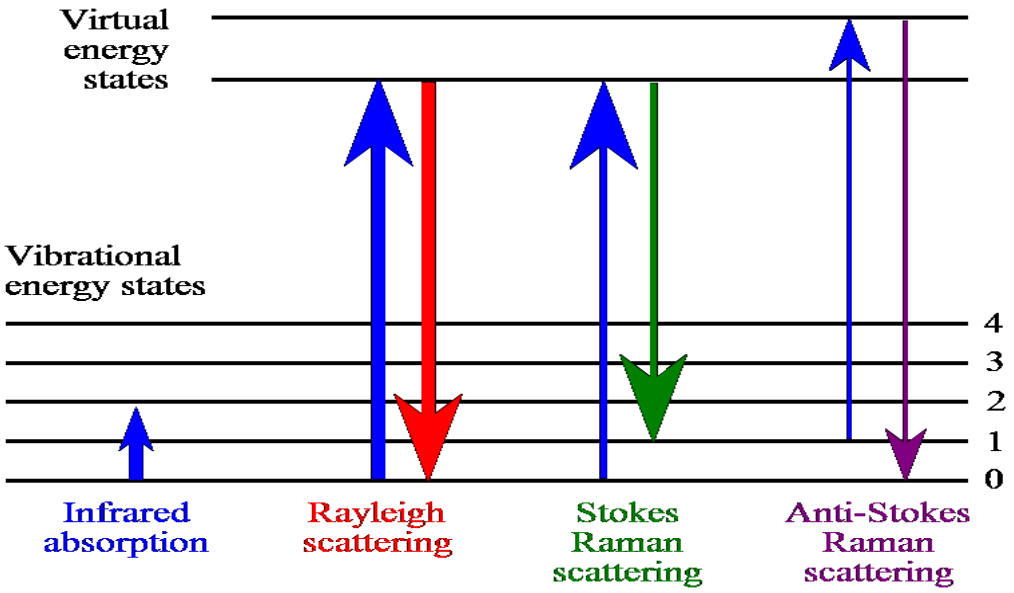

Figure 2.7 Schematic of energy level diagram related to Raman scattering. (http://en.wikipedia.org/wiki/Raman_spectroscopy)

In our Raman system setup, we use 632.8nm He-Ne laser as the monochromatic light source, and use the confocal microscope system to focus the laser spot. The spot size was 2μm. Raman signals were recorded by using HORIBA iHR550 spectrometer and Symphony CCD detectors. The sample/materials for Raman spectroscopy were deposited on 300nm SiO_2/Si wafer, for obtaining the best signal strength and signal to noise ratio.

3

UV sensitive electron transport layer in inverted polymer solar cell

Abstract

To fabricate an inverted polymer solar cell, an electron transport layer was introduced on ITO cathode to reverse the layer sequence of conventional PSCs. An inverted polymer solar cell with a structure of ITO/ZnO/P3HT:PCBM/PEDOT:PSS/Ag was fabricated. However, incorporating UV-sensitive electron transport layers (ETLs) into organic bulk heterojunction (BHJ) photovoltaic devices dramatically impacts short-circuit current (J_{sc}) and fill factor (FF) characteristics. UV illumination in the electron transport layer of inverted polymer solar cells would reduce the resistivity of ETLs and suppress bimolecular recombination. To further clarify UV effect and to find out the influence on transport properties in a working device, we have also investigated the recombination rate by transient photovoltage measurement.

3.1 Inverted polymer solar cell

The fabrication of a PSC device with an inverted geometry, in which the charge collecting nature of the electrodes is reversed, removes the need for the low-work-function, air-sensitive electrode. However, the challenge to reverse the layer sequence of PSCs is to prepare a selective contact bottom cathode.[1] A highly efficient bulk heterojunction polymer solar cell with an inverted device structure has been reported[2], which modified the organic/ITO interface by introduction of a low-temperature annealed interfacial buffer layer, cesium carbonate (Cs_2CO_3). Titanium oxide (TiO_x), as an electron-transporting and hole-blocking layer[3], was also used for modification of the surface between the organic layer and the ITO cathode. All these studies indicated that the performance of inverted type polymer solar cell is sensitive to the electron transport layer between the cathode and the active layer. Recently, zinc oxide (ZnO) has drawn much attention because of good transparency in the whole visible region and good electron mobility.[4] Moreover, the ZnO thin film can be easily deposited from corresponding solution via various solution processes, following thermal annealing treatment. All these features make ZnO an ideal material as an electron transport layer for inverted polymer solar cells.[5,6]

3.1.1 Preparation of ZnO thin film for electron transport layer

Zinc oxide (ZnO) is an inexpensive n-type semiconductor with a wide band gap of 3.3 eV, which crystallizes in the hexagonal wurtzite structure (c=5.205Å and a=3.249 Å). Several techniques were employed to produce pure ZnO films, including pulsed laser deposition[7], sputtering[8,9], chemical vapor deposition[10,11], and the sol-gel process[12-14]. Sol-gel process is an easy process to deposited ZnO thin film from corresponding solution via solution processes, following thermal annealing treatment. The procedure of sol-gel method for preparing ZnO thin films is shown in Figure 3.1. In this work, we use sol-gel ZnO thin films as an electron transport layer to fabricate inverted OPVs.

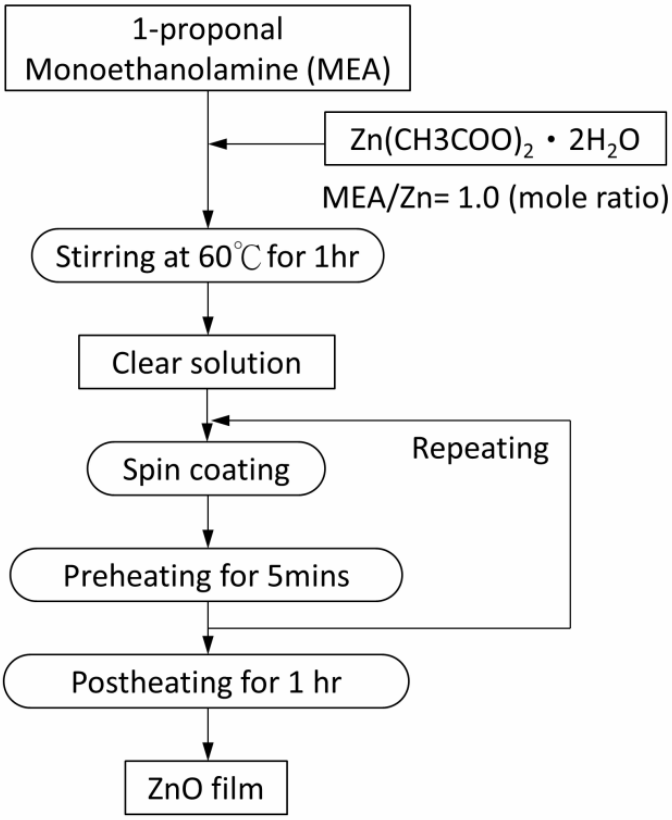

Figure 3.1 The flow chart shows the procedure for preparing ZnO films.

3.1.2 Fabrication of inverted type polymer solar cell

An inverted type polymer solar cell with a structure of ITO/ZnO/P3HT:PCBM/ PEDOT:PSS/Ag was fabricated as following procedures. ITO substrates were etched and cleaned with solvents. Substrates were then treated with oxygen plasma for 5 mins before the deposition of the ZnO layer which acted as an electron selective layer and was prepared by sol–gel method as shown in Figure 3.1. Zinc acetate dihydrate ($Zn(CH_3COO)_2 \cdot 2H_2O$) was dissolved in a mixture of 1-propanol ($CH_3CH_2CH_2OH$) and ethanolamine ($NH_2CH_2CH_2OH$) solution under stirring at 60^0C for 1 hour for hydrolysis reaction. The molar ratio of ethanolamine to zincacetate was maintained at 1 and the concentration of zinc acetate was 0.02 M. The as-prepared ZnO precursor was spin-coated on ITO substrates, following annealed at 100°C for 5 mins. The thin films were then continuously annealed in air at 200 °C for 1 h. The resulting film was rinsed in isopropanol and then dried at 200 ℃ for 5 min to remove any residual organic material from the surface.

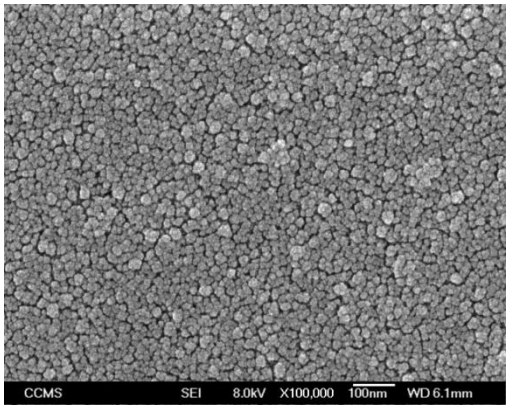

Figure 3.2 SEM image of the ZnO thin film deposited by sol-gel method.

The photoactive layer was deposited on top of the ZnO layer by spin coating using a 1:1 weight ratio blend consisting of P3HT (Rieke metal) and PCBM (Nano C) dissolved in chlorobenzene followed by the deposition of PEDOT:PSS diluted in isopropanol and then, annealed at 120℃ prior to the deposition of Ag electrode. Figure 3.3 shows the SEM cross-sectional image of the resulting device structure.

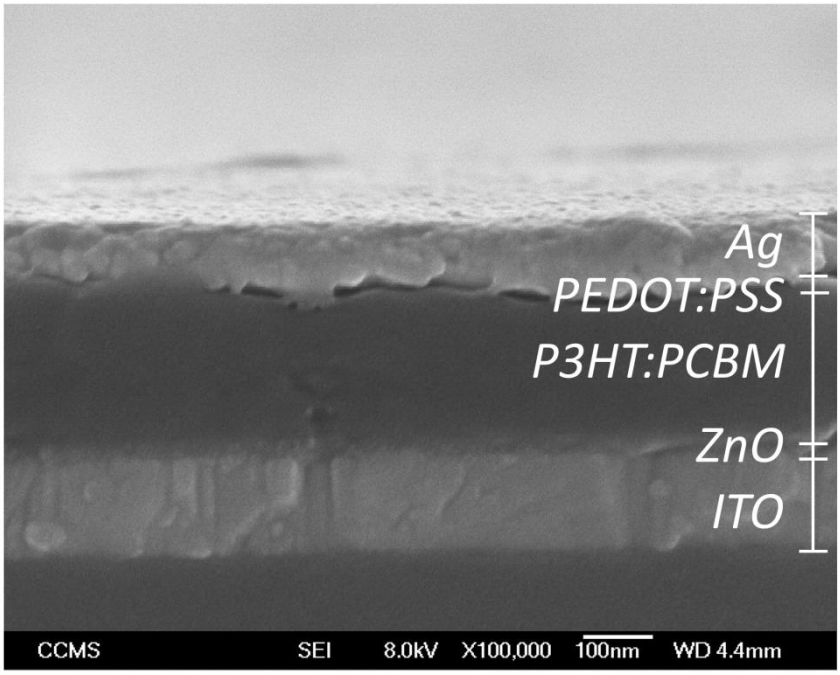

Figure 3.3 The cross-sectional SEM image of the device structure of the ITO/ZnO/P3HT:PCBM/PEDOT:PSS/Ag.

3.2 Suppression of recombination by UV illumination

3.2.1 Device performance due to UV effect

The electron transport layer such as TiO_x[15-17], TiO_2[18,19], ZnO[20,21] and Cs_2CO_3[22] for inverted type polymer solar cell are necessary to operate the device by matching energy levels with the photoactive layer. However, the UV response of ETL such as TiO_x has been known to have a great effect on device performance.[17,23] The J-V characteristics of a representative inverted OPV with Zinc oxide ETL is shown in Figure 3.5. We have observed that the device characteristic was further improved with continuous illumination for 2 mins. To investigate how UV illumination influences the interface between ETL and the photoactive layer, we used a 400 nm UV cut-off filter which was sufficient to block UV light from the solar simulator to compare the difference in the current-voltage characteristics as shown in Figure 3.4.

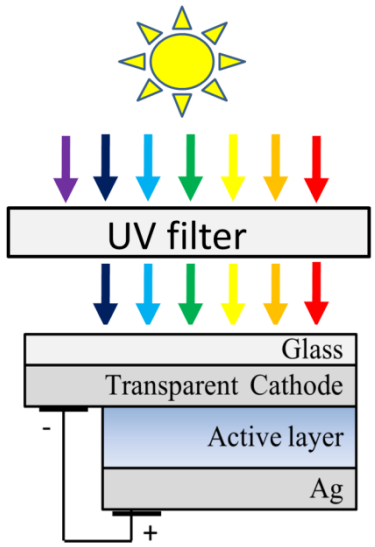

Figure 3.4 Schematic of the installation to illuminate the device by a solar simulator with a UV filter

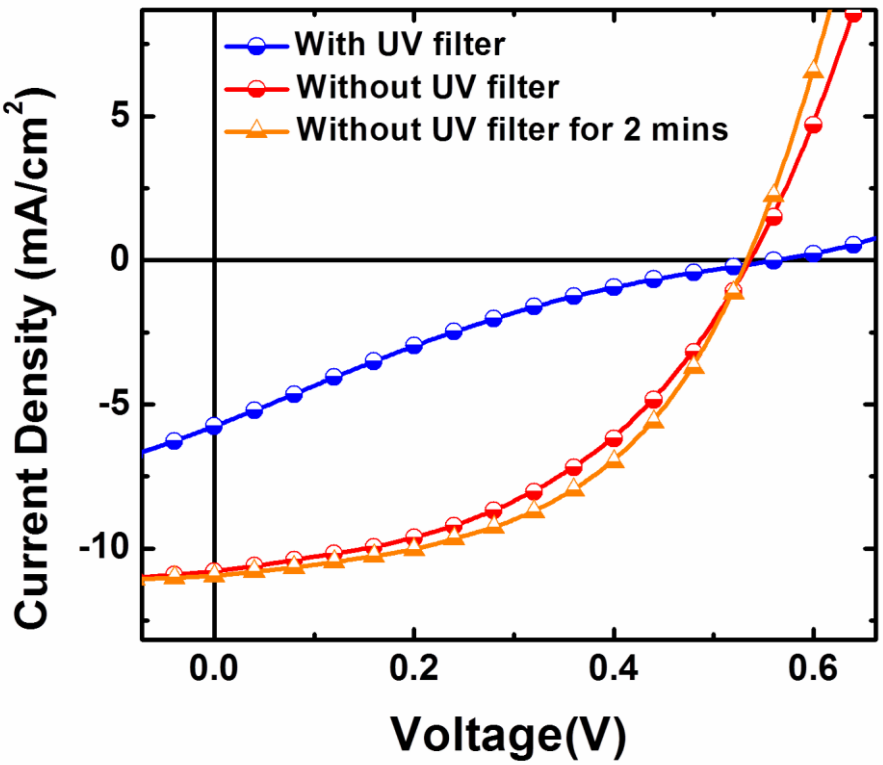

Figure 3.5 Current-voltage characteristics of inverted type polymer solar cell with and without an UV filter during illumination.

We have observed that an S-shape I-V curve was produced without UV exposure as shown in figure 3.5. This result is consistent with previous publications.[17,23] Compared to the device without the UV filter, the change was most notable in J_{sc} which increased from 5.77 mA/cm^2 to 10.8 mA/cm^2. The FF was also dramatically improved from 0.18 to 0.44 yielding an efficiency of 2.59%. A successive 2 mins of UV illumination has further improved the device performance with J_{sc} of 10.9 mA/cm^2 and FF of 49.1 yielding an efficiency of 2.88%.

We have further implement the same measurement on the conventional device to confirm this phenomenon as shown in Figure 3.6. We found that the UV illumination does not cause so large difference in the conventional device. With the UV filter, due to the loss of light at near UV region, J_{sc} was slightly decreased from 9.23 mA/cm^2 to 8.02 mA/cm^2; however, fill factor didn't change a lot and remained at about 0.55. This result supports the perspective that UV exposure somehow influences the electron transport layer such as ZnO which does not exist in conventional devices.

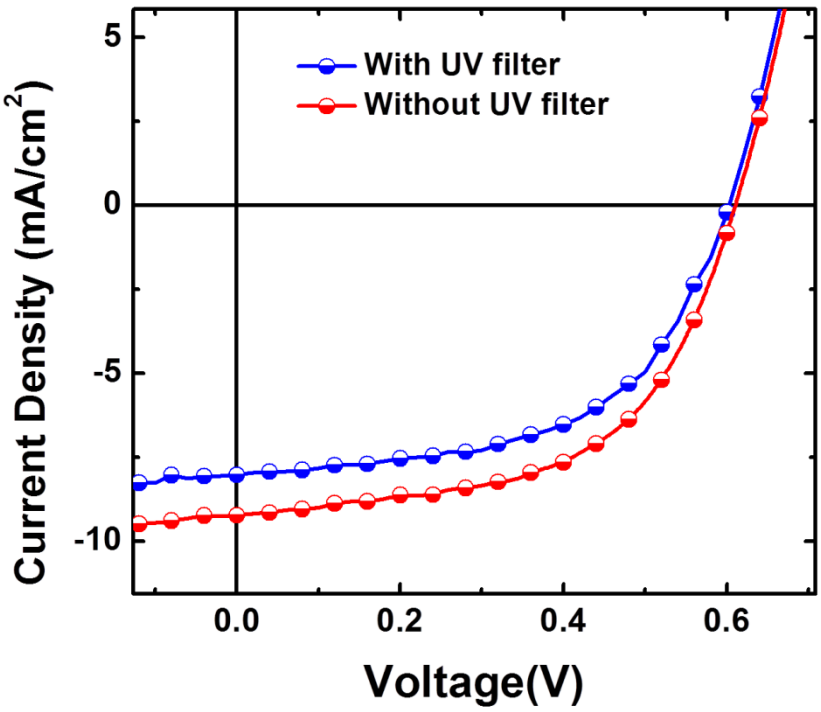

Figure 3.6 Current-voltage characteristics of conventional polymer solar cell with and without an UV filter during illumination.

3.2.2 Discussion and Transport properties

UV illumination on Zinc oxide leads to direct excitation of electrons from valence band to conduction band. These excited electrons, however, must first fill the shallow electron traps in Zinc oxide which leads to enhancement of photoconductivity of ZnO films. The evidence can be shown in the reduction of device series resistance, R_{series} (defined as the inverse slope of the current-voltage curves at V_{oc}), which decreased from 8.9Ω cm^2 to 3.68Ω cm^2 when exposed to UV. Under continuous illumination for 2 minutes, more traps were filled and led to further enhancement of device performance (Figure 3.5). The device series resistance has also decreased to 3.29Ω cm^2. Figure 3.7 shows the possible mechanism for this phenomenon.

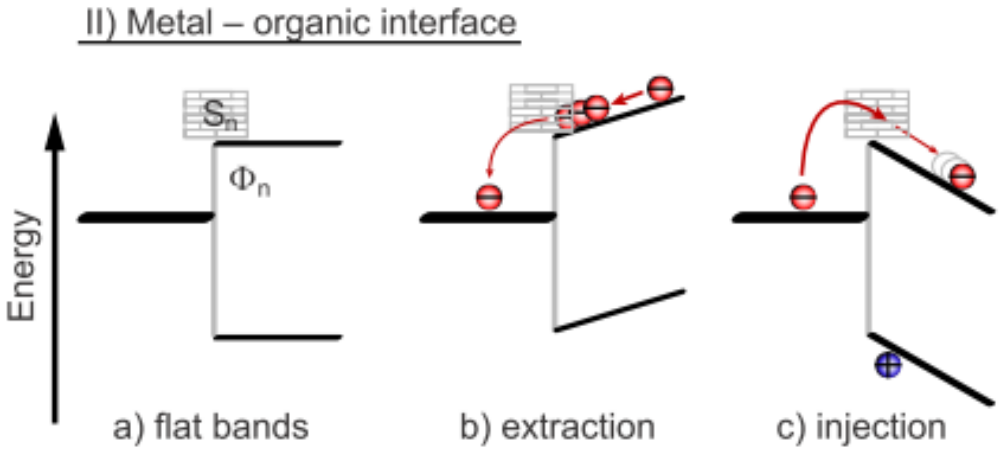

Figure 3.7 Space-charge accumulation in semiconductor devices.[24]

Under extraction conditions, charges are transported faster toward the interface than they can extract because of lower conductivity of the electron transport layer without UV exposure. Those charges will pile up creating a space charge depending upon the applied electric field thus causes the dramatic decrease in fill factor. This can explain the S-shape I-V curve of the device without UV exposure.

To clarify this effect and find out the transport property in a working device with and without UV exposure, we have further executed a transient photovoltage measurement (TPV). Figure 3.8 plots the charge recombination rate versus open circuit voltage under different power of incident light. For a comparison, we have also measured recombination rate of the conventional device. From Figure 3.8, we found that the slope of recombination rate to V_{oc} of the inverted device without UV exposure is different to that of the other two devices. This result indicated the different recombination mechanism at the interface of ETL and the photoactive layer as shown in Figure 3.9. With UV exposure, the slope of the inverted device is similar to that of the conventional cell, indicating the fill of traps which results in a trap-less recombination mechanism just like the device without ETL.

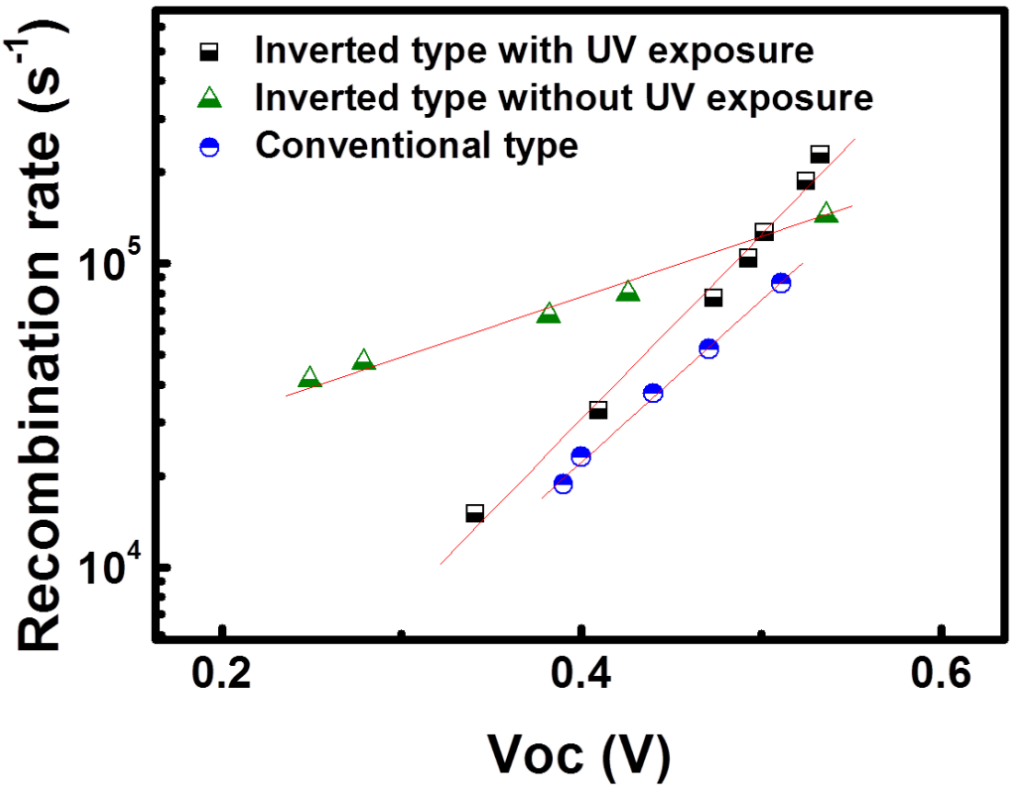

Figure 3.8 Charge recombination rate at Voc in different light intensity determined by TPV measurement.

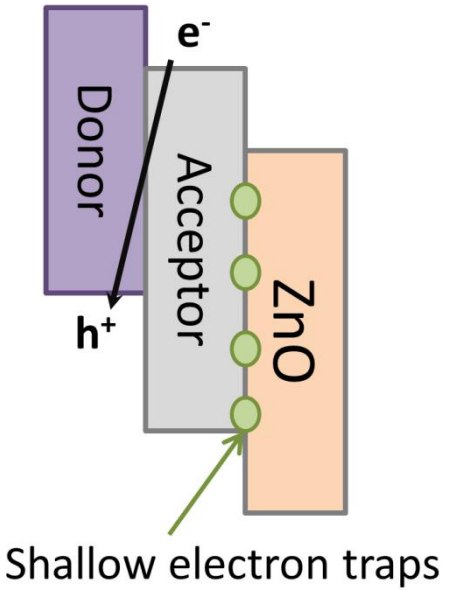

Figure 3.9 Recombination mechanism of inverted polymer solar cell with ZnO as an electron transport layer without UV exposure

We have known that the electrical properties of electron transport layer significantly affect device performance of inverted type solar cell. The resistivity of ZnO has profound effect on series resistance, which effectively controls bimolecular recombination. By TPV measurement, we have analyzed the recombination rate in the working device, and the results support the supposition that there are more traps in ZnO without UV exposure forming a different recombination mechanism and reducing the device performance.

3.3 Reference

[1] Waldauf, C.; Morana, M.; Denk, P.; Schilinsky, P.; Coakley, K.; Choulis, S. A.; Brabec, C. J. *Appl. Phys. Lett*. **2006**, *89*, 233517.

[2] Liao, H. H.; Chen, L. M.; Xu, Z.; Li, G.; Yang, Y. *Appl. Phys. Lett*. **2008**, *92*, 173303.

[3] Hayakawa, A.; Yoshikawa, O.; Fujieda, T.; Uehara, K.; Yoshikawa, Y. *Appl. Phys. Lett.* **2007**, *90*, 163517.

[4] Park, J. H.; Kang, G. S.; Kwon, S. I.; Lim, D. G.; Choi, Y. J.; Park, J. G. J. *Nanosci. Nanotechnol.* **2008**, *8*, 4658.

[5] White, M. S.; Olson, D. C.; Shaheen, S. E.; Kopidakis, N.; Ginley, D. S. *Appl. Phys. Lett.* **2006**, *89*, 143517.

[6] Hau, S. K.; Yip, H. L.; Baek, N. S.; Zou, J.; O'Malley, K.; Jen, A. K. Y. *Appl. Phys. Lett.* **2008**, *92*, 253301.

[7] F. K. Shan, Y. S. Yu, *J. Eur. Ceram. Soc.* **2004**, *24*, 1869.

[8] N. K. Shan, R. Greef, K. Rogers, A. J. C. Grellier, C. N. Pannell, *Thin Solid Films* **1999**, *352*, 179.

[9] W. T. Lim, C. H. Lee, *Thin Solid Films* **1999**, *353*, 12.

[10] K. H. Bang, D. K. Hwang, S. W. Lim, J. M. Myoung, *J. Cryst. Growth* **2003**, *250*, 437.

[11] N. Oleynik, M. Adam, A. Krtschil, J. Bläsing, A. Dadgar, F. Bertram, D. Forster, A. Diez, A. Greiling, M. Seip, J. Christen, A. Krost, *J. Cryst. Growth* **2003**, *248*, 14.

[12] T. Fukudome, A. Kaminaka, H. Isshiki, R. Saito, S. Yugo, T. Kimura, *Nucl. Instrum. Methods Phys. Res., Sect. B* **2003**, *206*, 287.

[13] L. Armelao, M. Fabrizio, S. Gialanella, F. Zordan, *Thin Solid Films* **2001**, *394*, 90.

[14] Y. Natsume, H. Sakata, *Mater. Chem. Phys.* **2002**, *78*, 170.

[15] C. Waldauf, M. Morana, P. Denk, P. Schilinsky, K. Coakley, S. A. Choulis, C. J. Brabec, *Appl. Phys. Lett*. **2006**, *89*, 233517.

[16] T. Ameri, G. Dennler, C. Waldauf, P. Denk, K. Forberich, M. C. Scharber, C. J. Brabec, and K. Hingerl, *J. Appl. Phys*. **2008**, *103*, 084506.

[17] R. Steim, S. A. Choulis, P. Schilinsky, C. J. Brabec, *Appl. Phys. Lett*.**2008**, *92*, 093303.

[18] C. Tao, S. Ruan, G. Xie, X. Kong, L. Shen, F. Meng, C. Liu, X. Zhang, W. Dong, and W. Chen, *Appl. Phys. Lett*. **2009**, *94*, 043311.

[19] C. Y. Li, T. C. Wen, T. H. Lee, T. F. Guo, J. C. A. Huang, Y. C. Lin, Y. J. Hsu, *J. Mater. Chem*. **2009**, *19*, 1643.

[20] S. K. Hau, H.-L. Yip, N. S. Baek, J. Zou, K. O'Malley, and A. K. Y. Jen, *Appl. Phys. Lett.* **2008**, *92*, 253301.

[21] M. S. White, D. C. Olson, S. E. Shaheen, N. Kopidakis, and D. S. Ginley, *Appl. Phys. Lett*. **2006**, *89*, 143517.

[22] G. Li, C. W. Chu, V. Shrotriya, J. Huang, and Y. Yang, *Appl. Phys. Lett*. **2006**, *88*, 253503.

[23] D. H. Ko, J. R. Tumbleston, M. R. Ok, H. Chun, R. Lopez, E. Samulski, *J. Appl. Phys.* **2010**, *108*, 083101.

[24] A. Wagenpfahl, D. Rauh, M. Binder, C. Deibel, V. Dyakonov, *Phys. Rev. B: Condens. Matter* **2010**, *82*, 115306.

4

Using Graphene and Graphene oxide as a hole transport layer for inverted type PSCs

Abstract

In our previous publish, we have reported the use of graphene oxide (GO) to replace PEDOT:PSS as a hole transport layer and our results indicated that GO could be a simple solution-processable alternative to PEDOT:PSS as an effective hole transport and electron blocking layer in conventional polymer solar cell.[1] In this section, we will investigate the device performance of using GO as a hole transport layer between the photoactive layer and the metal anode in inverted polymer solar cells. Furthermore, we have also introduced using graphene which is p-type prone in air to be another choice of the hole transport layer in inverted polymer solar cells. According to the results, we have found that graphene oxide and graphene are two promising materials to substitute for PEDOT:PSS to make a high efficiency inverted polymer solar cell.

4.1 Graphene oxide (GO)

Graphene oxide is a graphene sheet functionalized with oxygen groups in the form of epoxy and hydroxyl groups on the basal plane and various other types at the edges.[2,3] The C-O bonds are covalent and thus disrupt the sp^2 conjugation of the hexagonal graphene lattice, making GO an insulator. The electronic structure of GO is heterogeneous due to presence of mixed sp^2 and sp^3 hybridizations and therefore cannot be readily explained by traditional valence and conduction band states.[4] Rather, lateral transport occurs by hopping between localized states (sp^2 sites) at the Fermi level.[5] The density of such localized states can be increased by removing oxygen using a variety of chemical and thermal treatments, which facilitate the transport of carriers,[6,7] making reduced GO a semimetal.[5,6] Figure 4.1 shows photographs of GO thin films on different substrates.

Figure 4.1 Thin films of solution-processed GO, Photographs of GO thin films on filtration membrane (a), glass (b) and plastic (c) substrates[6]

4.1.1 Synthesis of graphene oxide

GO was obtained from purified natural graphite powder (SP-1, Bay Carbon) using the modified Hummers method[8] and the following procedures are shown in Figure 4.2. First, 2 g graphite powder and 1.5 g $NaNO_3$ were placed in a flake, with 70 ml of H_2SO_4 (98%) adding to the mixture. Then, use stirring magnet to stir the mixture under cooling in an ice water bath. 9 g $KMnO_4$ (99%) was gradually added over 1 hour. Cooling was completed in 2 hours and then kept the mixture with gentle stirring at room temperature for 5 days. During the stirring, the mixture would change from dark green to dark brown and become a highly viscous liquid. After 5 days, the viscous liquid was gradually added to 200ml H_2SO_4 (5 wt% aqueous solution) over about 1 hour with stirring, and the resultant mixture was further stirred 2 hours. Then, 9 ml H_2O_2 (35 wt% aqueous solution) was added to the mixture and the mixture was stirred for 1 hours. To remove the ions of oxidant origin and get GO, the mixture was further purified by the following four procedures cycle 15 times: (a) centrifugation, (b) removal of the supernatant liquid, (c) adding mixed aqueous solution of 3 wt% H_2SO_4/0.5 wt% H_2O_2 and (d) shaking to re-disperse. After that, we repeated the procedures 3 times more while changing the mixed aqueous solution into DI water. A concentration of 2mg/ml in DI water was prepared for deposition of GO thin films.

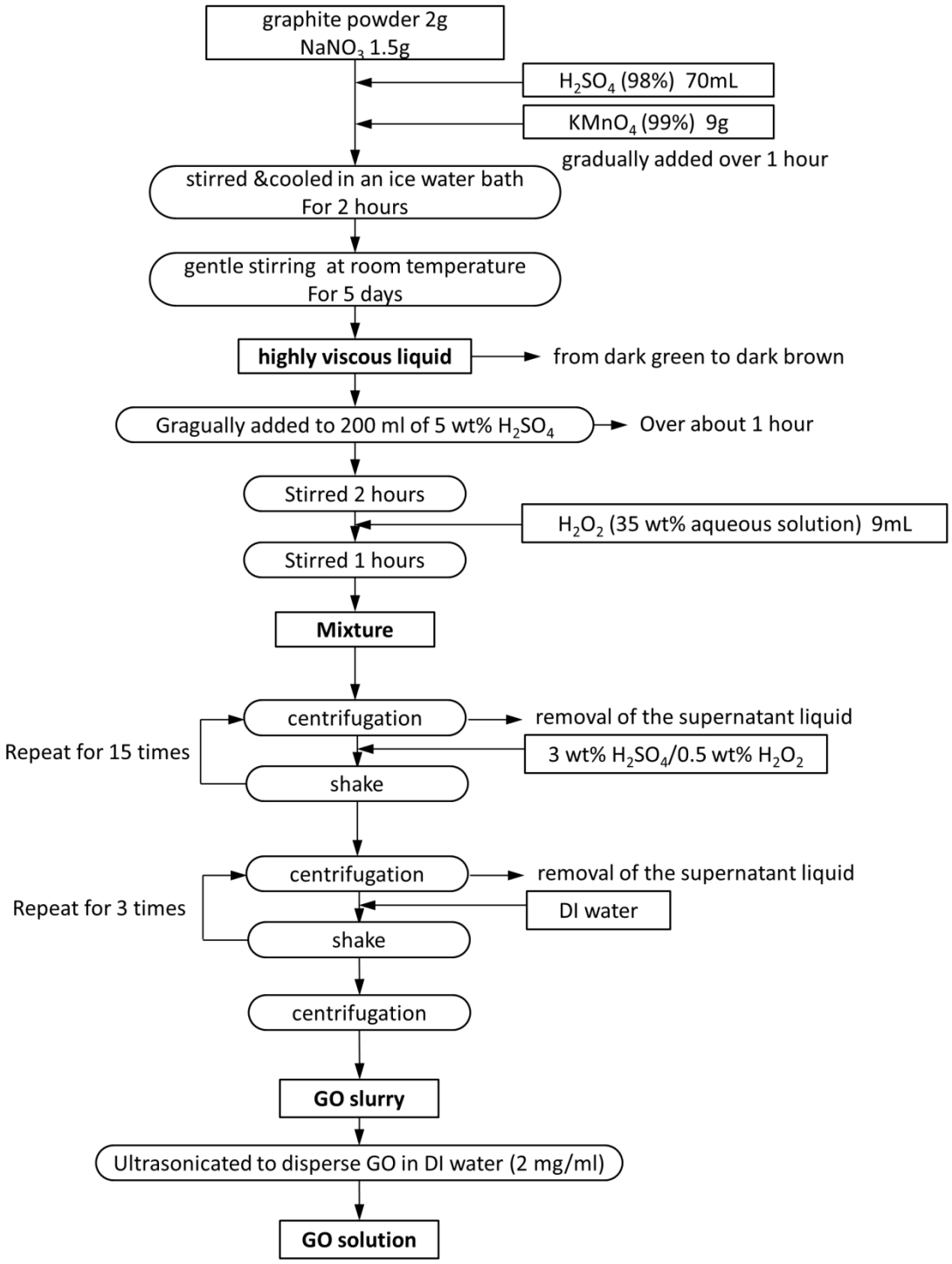

Figure 4.2 The flow chart shows the procedure for preparing graphene oxide.

4.1.2 Characterization of graphene oxide

A typical transmission electron microscopy (TEM) image and diffraction results have been shown to confirm the structure of GO sheets in as-prepared suspensions. A TEM image of a GO sheet and the corresponding selected area electron diffraction pattern (SAED) are shown in Figure 4.3 (a) and (b). The 6-fold symmetry in the diffraction pattern is consistent with the hexagonal structure, and the relative intensity of the inner $1\bar{1}00$-type and outer $2\bar{1}\bar{1}0$-type reflections shown in Figure 4.3(c) are consistent with that of a monolayer. [9]

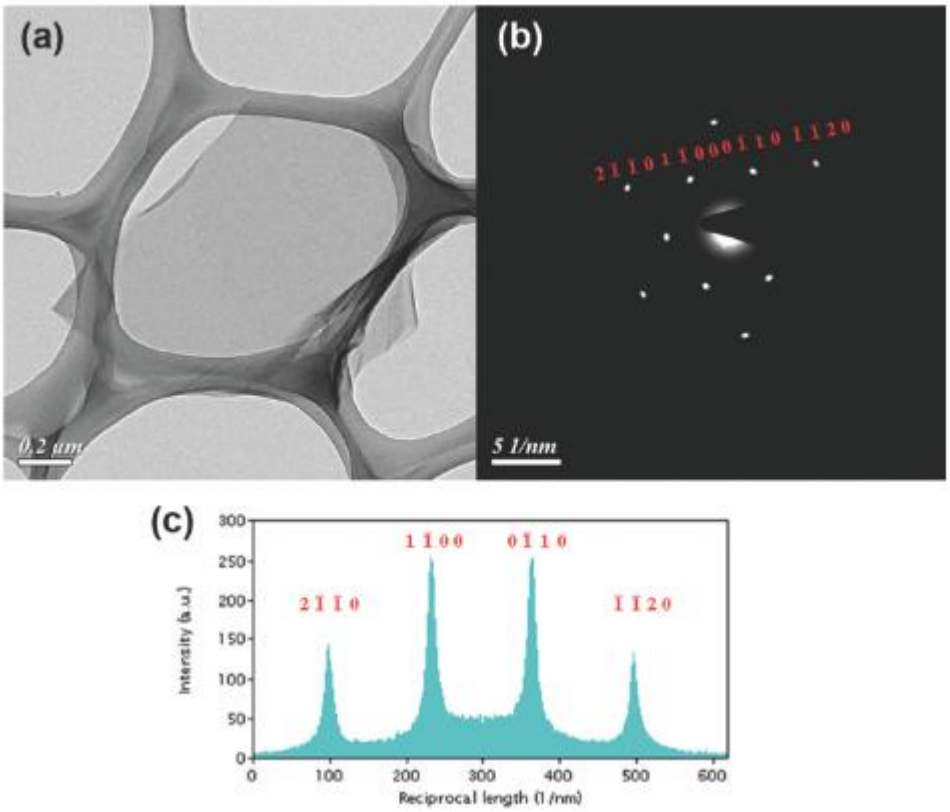

Figure 4.3 (a) TEM image of as-prepared GO sheet on a lacey carbon support. (b) SAED pattern; the diffraction spots are labeled with MillerBravais indices. (c) Relative intensity profile obtained from the diffraction pattern in (b).

We have also used the atomic force microscopy (AFM) to obtain the surface morphology of GO sheets. Figure 4.4 shows a single GO sheet deposited on a flat silicon substrate from GO aqueous solution. The lateral dimensions of GO flakes are ranged from 1-5 μm and the height was measured to be about 1 nm, which corresponds to an atom-layer thickness of a single GO sheet.

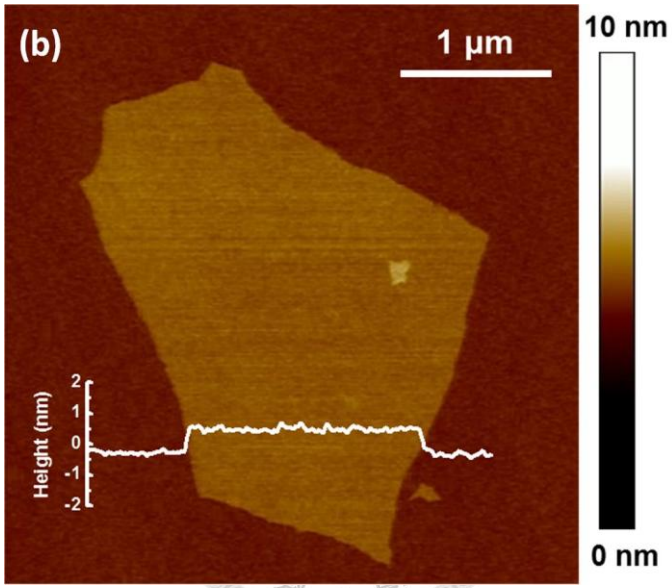

Figure 4.4 The AFM height image of a GO sheet on Si substrate and the corresponding height profile.

To substitute for PEDOT:PSS as a hole transport layer, GO should be deposited on the substrate to form a uniform thin film. Atomic force microscope (AFM) topography images of GO thin films of three different thicknesses are shown in Figure 4.5. Uniform thin films were deposited on top of silicon wafers by spin coating. The average thicknesses of the three samples were estimated to be ~2, ~4, and ~10 nm with corresponding rms roughness values of 0.70, 0.97, and 1.40 nm, respectively.

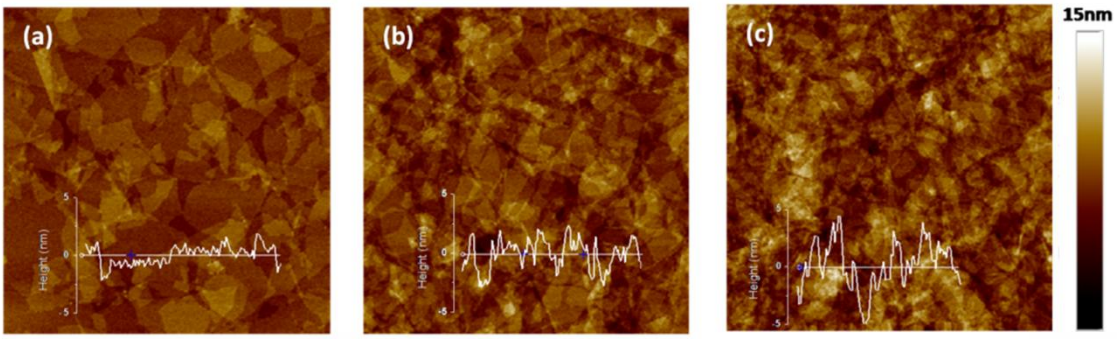

Figure 4.5 AFM height images of GO thin films with thicknesses of approximately (a) 2 nm, (b) 4 nm, and (c) 10 nm. Spin-coated from aqueous solution.

To investigate the hole transporting properties of GO, we have analyzed the energy level of GO. However, it's difficult to assign a specific band gap to GO because of the heterogeneous sp^2/sp^3 structure. The band gap represents potential barrier for transport formed by covalent sp^3 bonds. To obtain information about the sp^3 potential barriers, the optical gap of GO can be obtained from the Tauc plot [10] using the relation:

$$\alpha h\nu \propto (h\nu - E_g)^{1/2}$$

where α is the absorption coefficient, hν is the photon energy, and E_g is the optical gap. The Tauc plot for the 2 nm thick GO films shown in the Figure 4.6 indicates that Eg is 3.6 eV. Since GO can be considered as an insulator, we have further employed the photoionization measurement (Riken AC-2) to determine the highest occupied molecular orbital (HOMO) of GO. Figure 4.7 shows the HOMO level of GO fitted to ~5.2 eV, which is only ~0.2 eV below the HOMO level of P3HT lying at 5.0 eV. Considering with the band gap (3.6 eV), the lowest unoccupied molecular orbital

(LUMO) of GO was calculated to be ~1.6eV. This LUMO level of GO hinders the electrons to transport from the P3HT or PCBM to the anode. These electron blocking and hole transporting properties make GO a promising material to be a hole transport layer in polymer solar cells as shown in Figure 4.8.

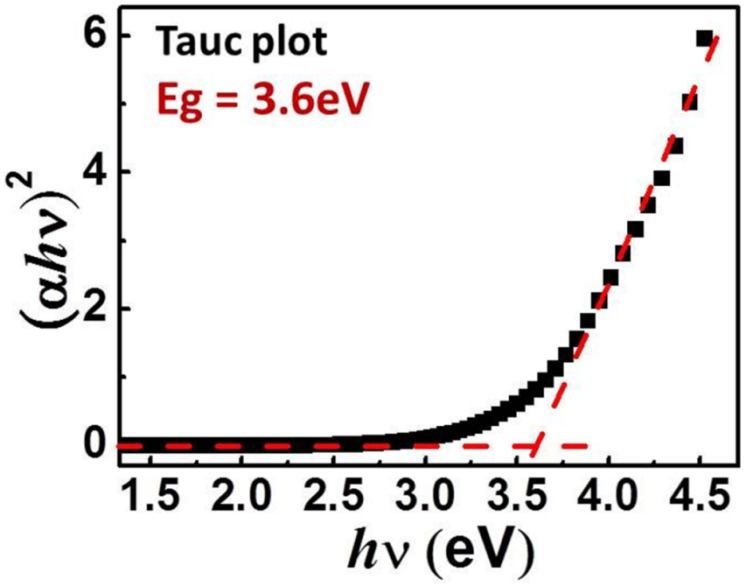

Figure 4.6 Tauc plot measurement obtained from the absorption spectrum of GO

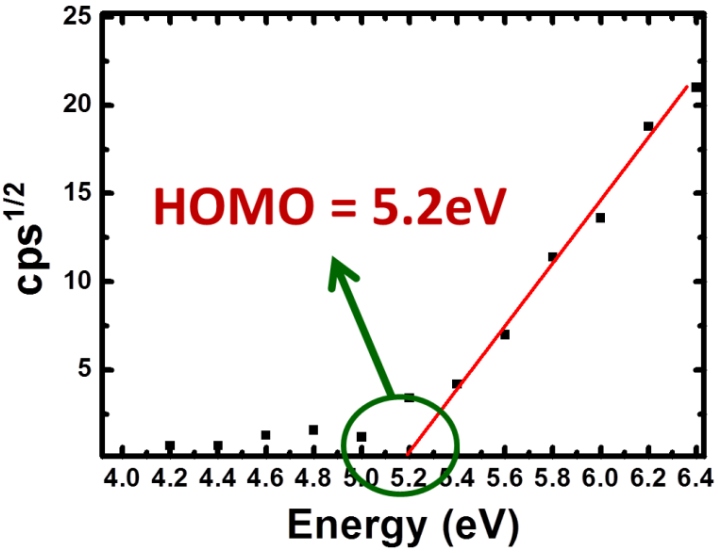

Figure 4.7 The HOMO level of GO determined by Riken Keiki AC-2 photoionization measurement.

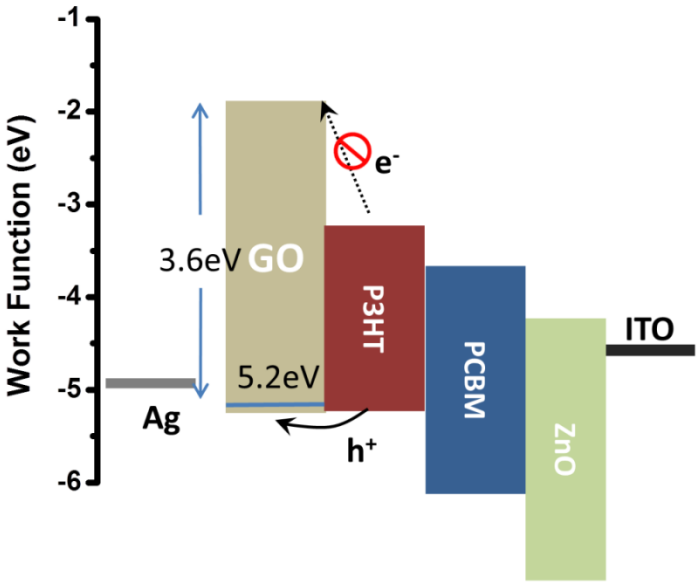

Figure 4.8 Energy level diagrams of the bottom electrode ITO, interlayer materials (ZnO), P3HT (donor), and PCBM (acceptor), interlayer materials (GO) and the top electrode Ag.

4.1.3 Fabrication of inverted devices with GO as a hole transport layer

In our previous publish, we have known that to be a great hole transport layer, the thickness of GO needs to be as thin as possible due to the high resistivity of GO thin film, and the uniformity is another critical issue. To be applied to an inverted type OPVs, GO should be spin-coated on top of the P3HT:PCBM active layers. Therefore, we mixed the GO aqueous solution with iso-propanol (mixed solvent) to improve the wetting with the hydrophobic layer. We have also used AFM image to investigate the thickness and uniformity of GO thin films (in mix solvent). Figure 4.9 shows that we can control the uniformity easily by spin-coating different concentration of GO on the substrates.

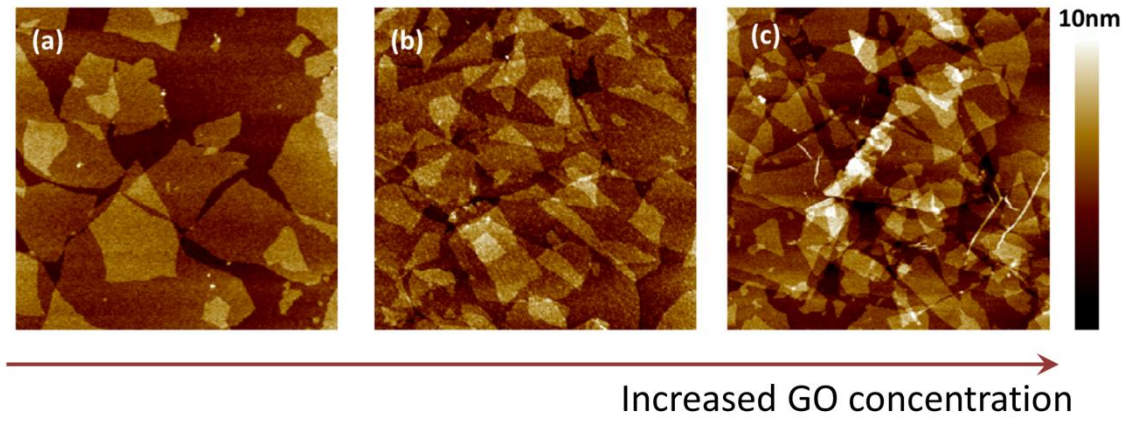

Figure 4.9 AFM height images of GO thin films spin-coated on a wafer from mixed solvent. From (a) to (c) shows the morphology of GO thin film using different concentration of GO solution which are 3mg/ml, 3.5mg/ml and 6mg/ml respectively.

However, it is difficult to directly measure the morphology of the GO layer prepared under different deposition conditions because the thickness of a single layer GO nanosheet (~1 nm) is less than the roughness of the BHJ. To find out the best condition of graphene oxide, we try the different concentration of GO solution ranging from 2 mg/ml to 10mg/ml. J-V characteristics of these devices are shown in Figure 4.10 and the summaries of the device performance are also shown in Table 4.1. The thickness of the GO layer is an important factor that affects the device performance. Since graphene oxide has high electrical resistivity, the thicker films of GO greatly increased the series resistance of the device and led to the lower fill factor and short circuit current. With decreasing the concentration of GO, the device performance was enhanced. However, 2mg/ml GO is too diluted to make a uniform thin film on the active layer resulting in the decrease of device performance. From these results, we could find that

2.5mg/ml of graphene oxide may have formed a complete coverage of the BHJ layer, which provides the optimized conditions for high performance devices.

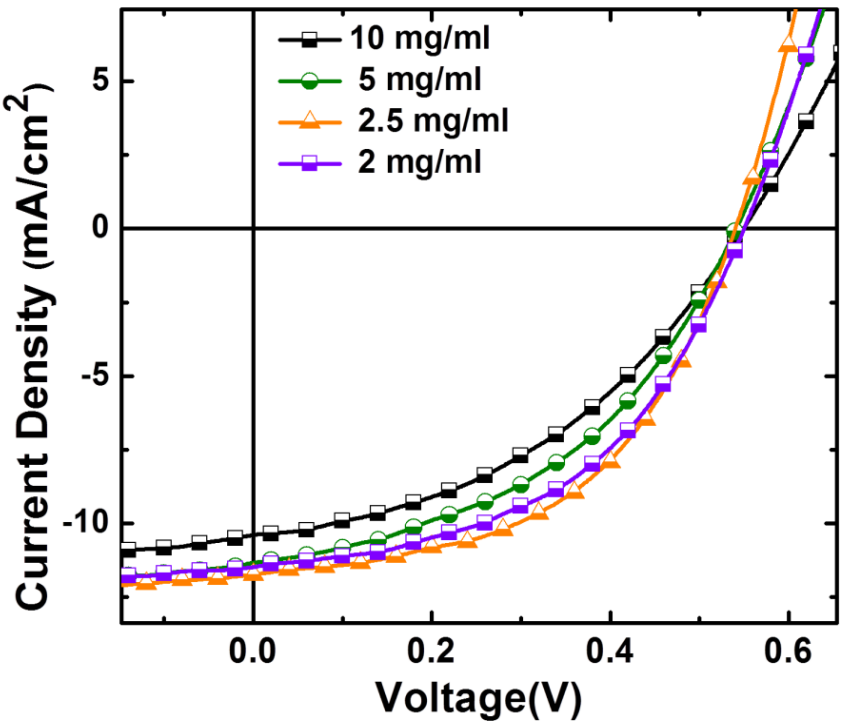

Figure 4.10 Current-voltage characteristics of the inverted polymer solar cells consisting of various concentration of graphene oxide as a hole transport layer (A.M. 1.5 illumination, 100 mW cm^{-2}).

Table 4.1 Summaries of the device performances of the inverted polymer solar cells under illumination (A.M.1.5, 100 mW cm^{-2}) using different concentration of graphene oxide as a hole transport layer.

GO(mix solvent)	V_{oc} (V)	J_{sc} ($mAcm^{-2}$)	FF	PCE (%)
10mg/ml	0.55	10.36	41.6	2.37
5mg/ml	0.54	11.33	44.1	2.70
2.5mg/ml	0.54	11.73	50.8	3.22
2mg/ml	0.55	11.48	48.1	3.04

4.1.4 Device performance and discussion

Figure 4.11 shows the comparison of the device performance using different hole transport layers. The short-circuit current density (J_{sc}), open-circuit voltage (V_{oc}), fill factor (FF), and power conversion efficiency values for each set of devices are summarized in Table 4.2. It can be seen that the device without HTL exhibits power conversion efficiency (η) of 0.7%. The insertion of GO thin film between active layer and Ag electrode results in a substantial increase in V_{oc} and J_{sc}, leading to an enhancement in the power conversion efficiency (3.22%). A typical device with PEDOT:PSS as a hole transport layer has a conversion efficiency of 3.37% which shows that GO is a promising material to substitute for PEDOT:PSS and yielding a comparable performance. Furthermore, using GO thin film could avoid several undesired properties existing on PEDOT:PSS, including their acidic and hygroscopic nature[11], electrical and structural inhomogeneity[12] and poor electron blocking property[13] which may undermine its potential as a HTL. The potential for large scale synthesis of inexpensive GO and its compatibility for solution processes makes it a promising HTL for low-cost PSCs.

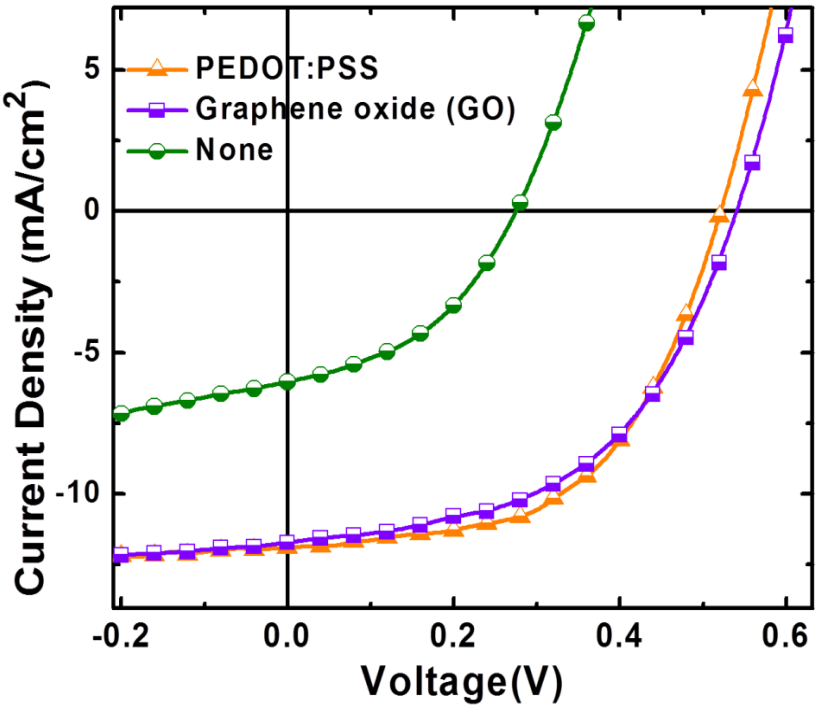

Figure 4.11 Current-voltage characteristics of the inverted polymer solar cells consisting of PEDOT:PSS and GO as a hole transport layer.(A.M. 1.5 illumination, 100 mW cm^{-2}). The device performance of the device without HTL was also shown.

Table 4.2 Summaries of the device performances of the inverted polymer solar cells under illumination (A.M.1.5, 100 mW cm^{-2}) using PEDOT:PSS and GO as a hole transport layer. The device performance of the device without HTL was also shown.

HTL	**V_{oc} (V)**	**J_{sc} ($mAcm^{-2}$)**	**FF**	**PCE (%)**
PEDOT:PSS	0.52	11.9	54.3	3.37
GO	0.54	11.7	50.8	3.22
None	0.28	6.03	41.5	0.70

4.2 Graphene

Graphene as shown in Figure 4.12, which consists of a single atom-thick plane of carbon atoms arranged in a honeycomb lattice, has been experimentally studied for over 40 years. Due to some excellent properties, it has aroused great interest in recent years. For example, it has a large theoretical specific surface area (2630 m^2g^{-1}), high intrinsic mobility (200000$cm^2v^{-1}s^{-1}$),[14,15] high Young's modulus (~1.0 TPa)[16] and good thermal conductivity (~5000 $Wm^{-1}K^{-1}$).[17] Its optical transmittance (~97.7%) and good electrical conductivity make it a promising material for transparent conducting electrode applications.[18] The 2D structure and high electrical conductivity let graphene a good sensor for gas detection.[19] Lots of researches also focus on the application of Graphene transistors.[20]

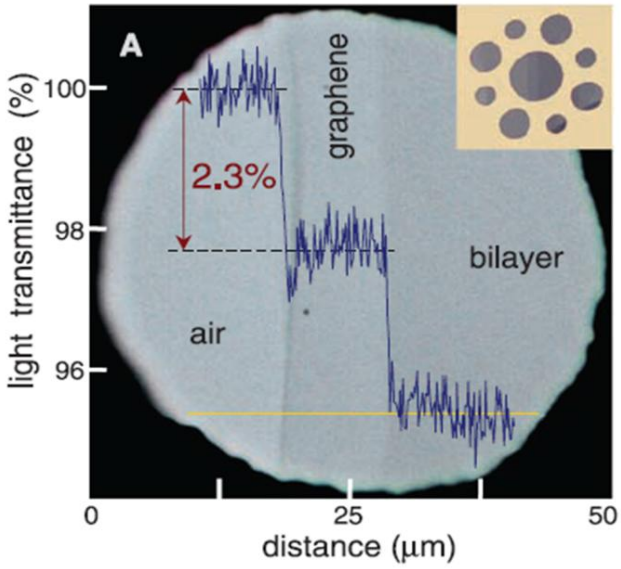

Figure 4.12 Photograph of a 50-mm aperture partially covered by graphene and its bilayer. The line scan profile shows the intensity of transmitted white light along the yellow line.

4.2.1 Synthesis of graphene

Mechanical exfoliation

In 2004, the Manchester group used cohesive tapes to split graphite crystals to obtain graphene by mechanical exfoliation. The flakes were dissolved in acetone and then were deposited on a silicon wafer. After a year, dry deposition process was demonstrated which could avoid the stage for graphene to float in the liquid. By this technique, relatively larger graphene sheets were obtained. This is the very beginning process to get the isolated graphene sheets, which were often presumed not to exist.[21]

Epitaxial growth on silicon carbide

This method is to heat silicon carbide (SiC) up to 1100℃ to reduce it to graphene.[22] Dimensions of graphene produced by this method is highly dependent on the size of SiC substrates. The face of the SiC used for graphene formation also has great influences on the thickness, mobility and carrier density of the graphene.

Epitaxial growth on metal substrates

The commonly used method is to use the atomic structure of a metal substrate to seed the growth of the graphene. High quality of few layers graphene could be synthesized via chemical vapor deposition on nickel films. For further improvement, growth of graphene on copper foils was demonstrated. At very low pressure, when a single layer of graphene was formed, the growth was automatically stopped. Therefore, this method provides us single layer graphene films and after growth, these graphene

sheets could be successfully transferred to different substrates for further analysis and numerous electronic applications.[23,24]

4.2.2 P-doped graphene due to adsorption of H_2O and O_2 in air

The large surface-to-volume ratio makes graphene extremely sensitive to the environment. The influence of the surroundings has been taken into account in many ways in the literature, such as the influence of substrate[25], metal contacts[26] and shot noise.[27] The doping of graphene is most likely caused by the molecular adsorption such as NH_3, NO_2, CO, and H_2O. The adsorbed H_2O and NO_2 molecules work as acceptors whereas NH_3 and CO work as donors. Because of the direct impact of the surroundings, there could be H_2O and O_2 molecules adsorbed on graphene when exposed to air. According to previous researches, graphene is even more heavily doped simply after annealing in vacuum and exposed to an air ambient.[28]

Raman spectroscopy has been historically used to probe structural and electronic characteristics of graphite materials, and is also sensitive to the doping in graphene. Figure 4.13 shows the Raman spectra of graphene before and after annealing. The blue shift of G and 2D bands indicates the doping when exposed to air ambient after vacuum annealing. Figure 4.14 is the doping process of graphene, and the sample is also checked after leaving in air for 15 days. The result shows that the doping molecules are stable in air and can be removed after vacuum annealing.

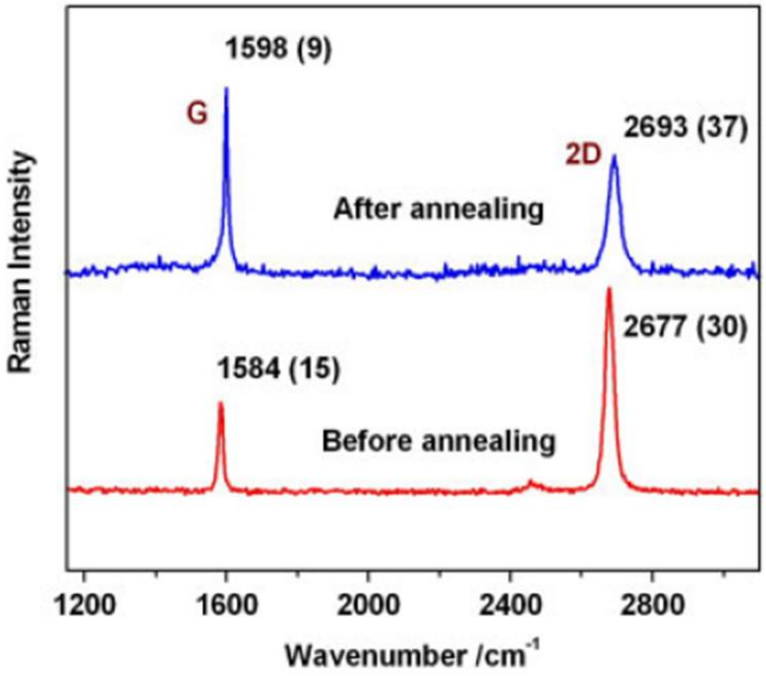

Figure 4.13 The Raman spectra of graphene before and after vacuum annealing and exposed to air ambient. The numbers above each indicate the peak wavenumber and bandwidth.[28]

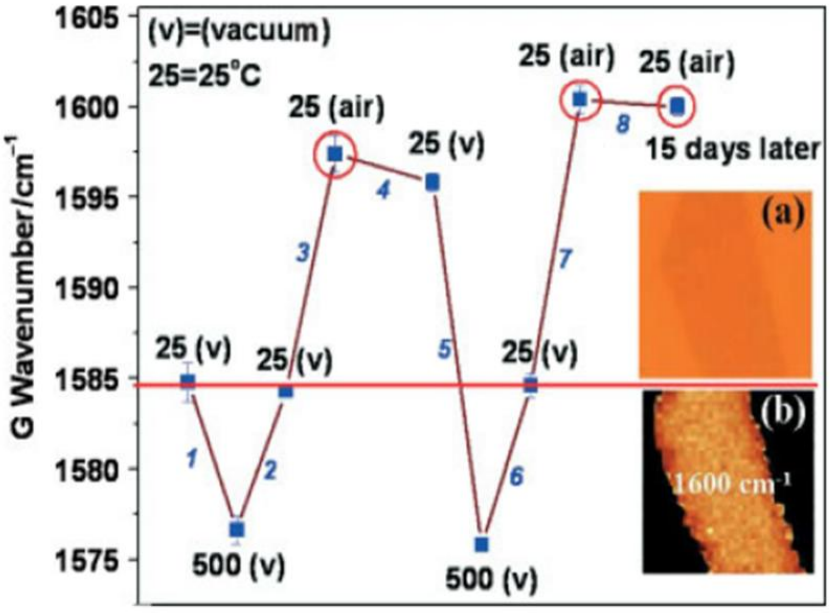

Figure 4.14 The doping process of SLG. Graphene sample is heated to 500 ◦C in vacuum (step 1), and cooled down to room temperature (step 2), then exposed to air ambient (step 3). To check the stability, sample is introduced into vacuum for 2 h (step 4). It is then heated again to 500 ◦C (step 5) and cooled down (step 6), exposed to air ambient (step 7). The sample is checked after leaving in air for 15 days (step 8).[28]

4.2.3 Experimental step

In this section, we introduced using a single layer graphene to substitute for PEDOT:PSS as a hole transport layer in inverted polymer solar cells as shown in Figure 4.15. After the deposition of ZnO electron transport layer and the P3HT:PCBM blend film, the following transferred process was carried out in the glove box. We used a thermal released process, which attached the CVD graphene grown on a copper foil to a thermal released tape, and then etched the copper by immersing the tape with graphene in the $Fe(NO_3)_3$. After the etching process, we got a single layer graphene on a thermal released tape. Then, we attached the tape with graphene onto the top of the device and rolled by the roller. Then, the whole device was put on the hot plate at 120℃. After a minute, a device with a single layer graphene as a hole transport layer was prepared. Different metal top electrodes were deposited by thermal evaporation for comparison.

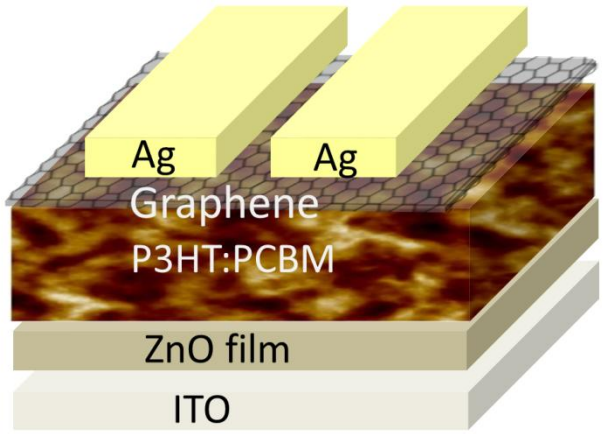

Figure 4.15 Device architecture of an inverted polymer solar cell with a single layer graphene as a hole transport layer

4.2.4 Device performance and discussion

Electrical transport characteristic of single layer graphene with and without oxygen doping is shown in Figure 4.16. The two devices were measured in air and in vacuum respectively. After exposed to air ambient, the Dirac point of the device shifted to higher voltage as illustrated by the curve with circle points in Figure 4.16, indicating increased hole doping in the graphene device due to the adsorption of H_2O and O_2. This phenomenon makes graphene another candidate to replace PEDOT:PSS for hole transporting. Figure 4.17 is AFM image of single layer graphene transferred on a glass. The continuity and uniformity of graphene on the substrate give graphene a great possibility to overcome the inhomogeneity of PEDOT:PSS which leads to the poor electron blocking property.

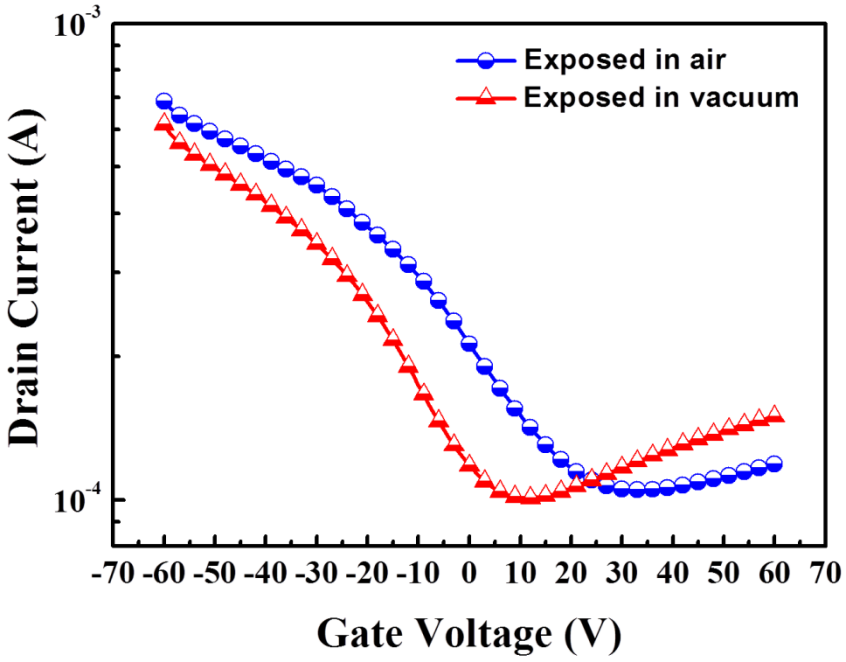

Figure 4.16 Electrical properties of SLG with and without oxygen doping.

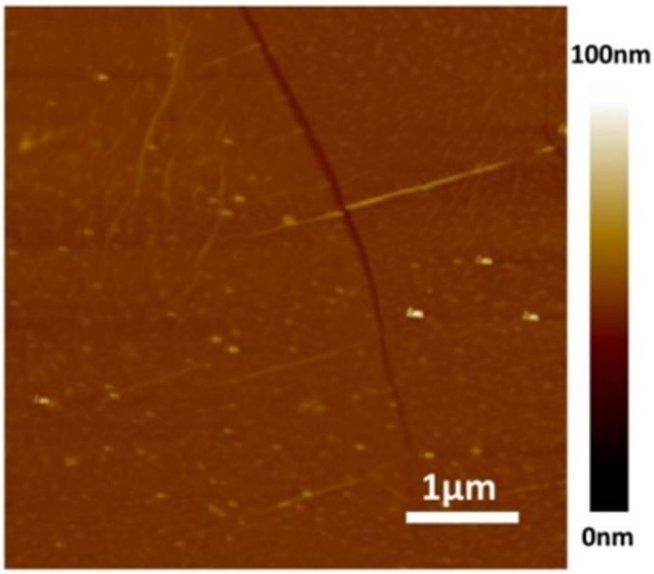

Figure 4.17 AFM image of graphene deposited on a glass substrate.

The effect of single layer graphene hole transport layer on the performance of inverted P3HT:PCBM PSCs using metals with different work functions as the top anodes (Ag, Al) was investigated. The current density-voltage curves under illumination are shown in Figure 4.18(a) and (b). Devices without graphene single layer between BHJ and the metal electrodes showed quite poor performance with low short circuit currents (J_{sc}) and open circuit voltages (V_{oc}). Since the upper bound of V_{oc} is governed by the difference between the work functions of the electrodes, a clear trend of increased V_{oc} with increasing anode work function was observed. However, when a graphene HTL was introduced, the two devices showed improved performance with a Voc of ~0.5V in two kinds of metal electrodes.

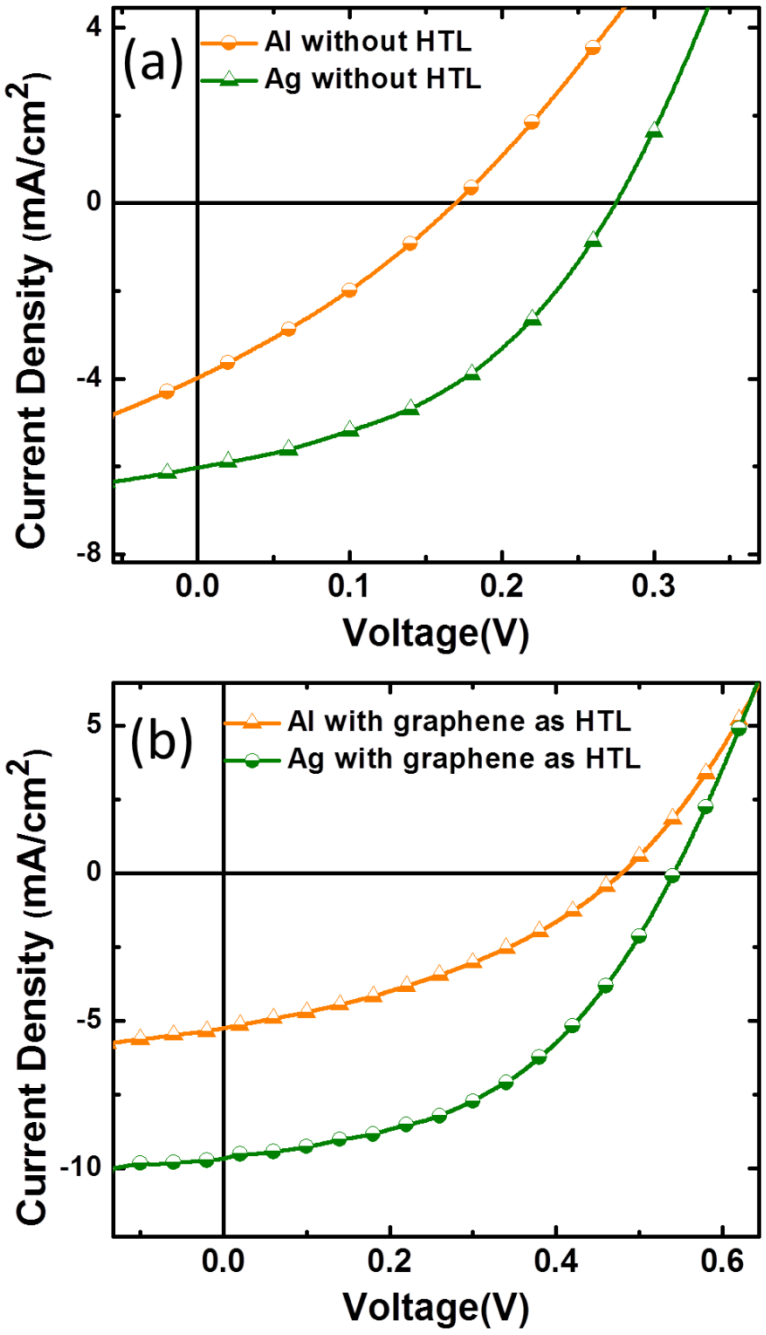

Figure 4.18 (a)(b) The current density–voltage (J-V) characteristics of inverted polymer solar cells (a) without graphene HTL and (b) with graphene HTL using different top metal electrodes.

The J-V curves of devices with no HTL and with different HTLs including PEDOT:PSS, GO and Graphene are shown in Figure 4.19. Although efficiency of the device with graphene HTL is still lower compared to that of PEDOT:PSS and GO, it still has a great improvement of the performance compared to the device without HTL. The possible reason for the lower J_{sc} and fill factor of the device with graphene may be the residual organic impurity between the graphene and the top electrode which leads to the poor contact between the graphene layer and the top anode.

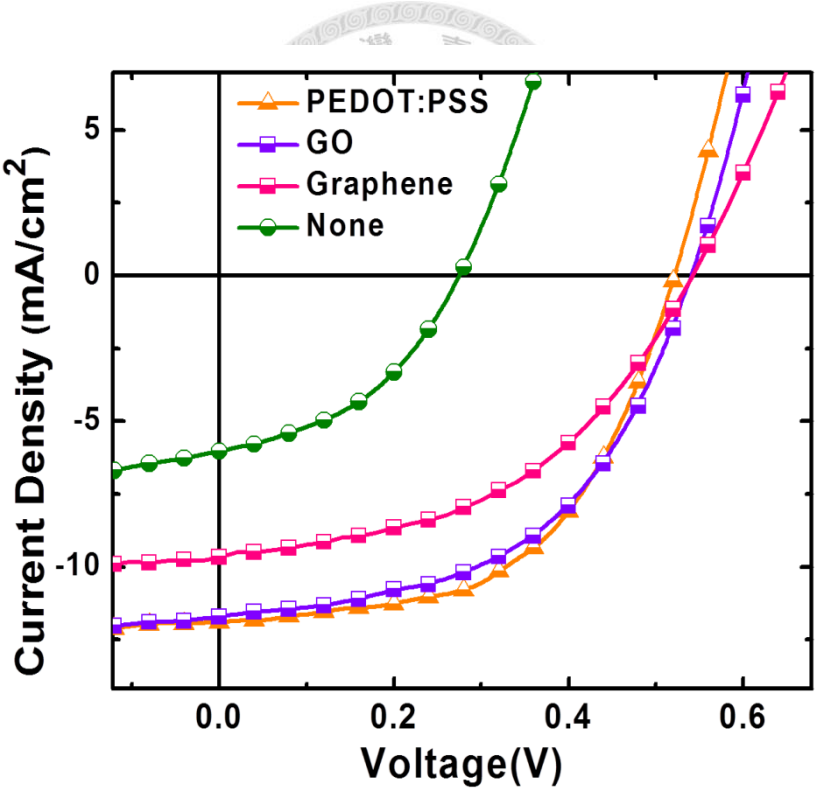

Figure 4.19 Current-voltage characteristics of the inverted polymer solar cells consisting of PEDOT:PSS, GO and Graphene as a hole transport layer.(A.M. 1.5 illumination, 100 mW cm^{-2}). The device performance of the device without HTL was also shown.

Table 4.3 Summaries of the device performances of the inverted polymer solar cells under illumination (A.M.1.5, 100 mW cm^{-2}) using PEDOT:PSS, GO and Graphene as a hole transport layer. The device performance of the device without HTL was also shown.

HTL	V_{oc} (V)	J_{sc} ($mAcm^{-2}$)	FF	PCE (%)
PEDOT:PSS	0.52	11.9	54.3	3.37
GO	0.54	11.7	50.8	3.22
Graphene	0.54	9.7	46.2	2.42
None	0.28	6.03	41.5	0.70

In summary, we have demonstrated that GO and Graphene can also be used as an hole transport layer (HTL) in inverted type polymer solar cell to improve the device performance as shown in Table 4.3. The optimized device performance with GO HTL is comparable to those using PEDOT:PSS as the HTL. However, graphene is another promising material to replace PEDOT:PSS. To overcome the impurity during transferred procedure for better performance is the first priority for further optimization.

4.3 Reference

[1] S. S. Li, K. H. Tu, C. C. Lin, C. W. Chen, M. Chhowalla, *ACS Nano* **2010**, *4*, 3169.

[2] H. C. Schniepp, J. L. Li, M. J. McAllister, H. Sai, M. Herrera-Alonso, D. H. Adamson, R. K. Prud'homme, R. Car, D. A. Saville, I. A. Aksay, *J. Phys. Chem. B* **2006**, *110*, 8535.

[3] H. Y. He, J. Klinowski, M. Forster, A. Lerf, *Chem. Phys. Lett.* **1998**, *287*, 53.

[4] C. Mattevi, G. Eda, S. Agnoli, S. Miller, K. A. Mkhoyan, O. Celik, D. Mastrogiovanni, G. Granozzi, E. Garfunkel, M. Chhowalla, *Adv. Funct. Mater.* **2009**, *19*, 2577.

[5] G. Eda, C. Mattevi, H. Yamaguchi, H. Kim, M. Chhowalla, *J.Phys. Chem. C* **2009**, *113*, 15768.

[6] G. Eda, G. Fanchini, M. Chhowalla, *Nat. Nanotechnol*. **2008**, *3*,270.

[7] S. Wang, P. J. Chia, L. L. Chua, L. H. Zhao, R. Q. Png, S. Sivaramakrishnan, M. Zhou, R. G. S. Goh, R. H. Friend, A. T. S. Wee, P. K. H. Ho, *Adv. Mater.* **2008**, *20*, 3440.

[8] M. Hirata, T. Gotou, S. Horiuchi, M. Fujiwara, M. Ohba, Carbon **2004**, *42*, 2929.

[9] Meyer, J. C.; Geim, A. K.; Katsnelson, M. I.; Novoselov, K. S.; Obergfell, D.; Roth, S.; Girit, C.; Zettl, A. *Solid State Commun*. **2007**, *143*, 101.

[10] Tauc, J. *Mater. Res. Bull.* **1968**, *3*, 37.

[11] M. Jørgensen, K. Norrman, and F. C. Krebs, Sol. *Energy Mater. Sol. Cells* **2008**, *92*, 686.

[12] L. S. C. Pingree, B. A. MacLeod, and D. S. *Ginger, J. Phys. Chem. C* **2008**, *112*,7922.

[13] S. K. Hau, H. L. Yip, J. Y. Zou, and A. K. Y. Jen, *Org. Electron*. **2009**, *10*, 1401.

[14] K. I. Bolotin, K. J. Sikes, Z. Jiang, M. Klima, G. Fudenberg, J. Hone, P. Kim, H. L.

Stormer, *Solid State Commun*. **2008**, *146*, 351.

[15] S. V. Morozov, K. S. Novoselov, M. I. Katsnelson, F. Schedin, D. C. Elias, J. A. Jaszczak, A. K. Geim, *Phys. Rev. Lett*. **2008**, *100*, 016602.

[16] C. Lee, X. D. Wei, J. W. Kysar, J. Hone, *Science* **2008**, *321*, 385.

[17] A. A. Balandin, S. Ghosh, W. Z. Bao, I. Calizo, D. Teweldebrhan, F. Miao, C. N. Lau, *Nano Lett*. **2008**, *8*, 902.

[18] Y. Wang, S. W. Tong, X. F. Xu, B. Ö zyilmaz, K. P. Loh, *Adv. Mater.* **2011**, *23*, 1514

[19] F. Schedin, A. K. Geim, S. V. Morozov, E. W. Hill, P. Blake, M. I. Katsnelson, K. S. Novoselov, *Nature Mater.* **2007**, *6*, 652.

[20] R. Sordan, F. Traversi, V. Russo, *Appl. Phys. Lett.* **2009**, *94*, 073305.

[21] K. S. Novoselov, A. K. Geim, S. V. Morozov, D. Jiang, Y. Zhang, S. V. Dubonos, I. V. Grigorieva, A. A. Firsov, Science **2004**, *306*, 666.

[22] P. Sutter, *Nature Mater.* **2009**, *8*, 171.

[23] S. Bae, H. Kim, Y. Lee, X. Xu, J. S. Park, Y. Zheng, J. Balakrishnan, T. Lei, H. R. Kim, Y. I. Song, Y. J. Kim, K. S. Kim, B. Ö zyilmaz, J. H. Ahn, B. H. Hong, S. Iijima, Nat. Nanotechnol. 2010, 5, 574.

[24] [d] K. S. Kim, Y. Zhao, H. Jang, S. Y. Lee, J. M. Kim, Kwang. S. Kim, J. H. Ahn, P. Kim, J. Y. Choi, B. H. Hong, *Nature* **2009**, *457*, 706.

[25] J. Sabio, C. Seoanez, S. Fratini, F. Guinea, A. H. Castro, F. *Sols*, *Phys. Rev. B* **2008**, *77*, 195409.

[26] E. J. H. Lee, K. Balasubramanian, R. T. Weitz, M. Burghard, K. Kern, *Nat. Nano* **2008**, *3*, 486.

[27] L. DiCarlo, J. R. Williams, Y. M. Zhang, D. T. McClure, C. M. Marcus, *Phys. Rev. Lett.* **2008**, *100*, 156801.

[28] Z. H. Ni, H. M. Wang, Z. Q. Luo, Y. Y. Wang, T. Yu, Y. H. Wu, Z. X. Shen, *J. Raman Spectrosc.* **2010**, *41*, 479.

5

Bifacial semitransparent inverted OPV with graphene/GO top electrode

Abstract

In this section, we demonstrated a semitransparent inverted polymer solar cell using a top laminated graphene electrode without damaging the underlying organic photoactive layer. The lamination process involves the simultaneous thermal releasing deposition of the graphene top electrode during thermal annealing of the photoactive layer. The resulting semitransparent polymer solar cell exhibits a promising power conversion efficiency of approximately 76 % of that of the standard opaque device using an Ag metal electrode. The asymmetric photovoltaic performances of the semitransparent solar cell while illuminated from two respective sides were further analyzed using optical simulation and photocarrier recombination measurement. The devices consisting of the top laminated transparent graphene electrode enable the feasible roll-to-roll manufacturing of low-cost semitransparent polymer solar cells and can be utilized in new applications such as power-generated windows, or multi-junction or bifacial photovoltaic devices.

5.1 Introduction

5.1.1 Graphene electrode

Graphene, which consists of a single atom-thick plane of carbon atoms arranged in a honeycomb lattice, has demonstrated excellent carrier transport arising from a unique two-dimensional (2D) energy dispersion.[1] In addition, graphene also exhibits a high transparency with a transmittance of 97.7% from a single layer graphene,[2] making it a promising candidate for transparent electrode applications.

Although several studies have reported on the graphene based electrode for replacing the ITO bottom electrode in organic photovoltaic devices,[3-5] until now, the use of the graphene top electrode in organic photovoltaics is still very limited. In this section, we would like to demonstrate a simple lamination process for depositing the graphene electrode on top of a polymer photovoltaic device, resulting in a semitransparent polymer solar cell with a power conversion efficiency of over 75% of that of the standard opaque device using an Ag metal electrode

5.1.2 Semitransparent solar cell

In polymer solar cells, to find a polymer that has the required properties such as strong and broad absorption, high carrier mobility, and appropriate energy levels is a critical issue for making high efficiency devices; however, it's nearly impossible to find a polymer that meets all the demand. To avoid such a restriction, a semitransparent solar cell with high absorption coefficient at its absorption wavelength range, while high transparency in the complementary range, shows the superiority. Because of the semitransparent property, it's feasible to stack two or more devices with different spectral responses, which enables efficient utilization of solar energy in different polymers.

One critical issue in the fabrication of semitransparent organic solar cells is that the electrode must be deposited on top of the cell without damaging the underlying organic photoactive layer to establish a good electrode contact. To reach the goal of fabricating a semitransparent and also indium tin oxide-free, metal-free polymer solar cell, a group used high-conductivity PEDOT:PSS film (PH1000) as both the bottom and the top electrodes.[6] The Yang's group also demonstrated a lamination process to use conductive polymer glue as medium to form a semitransparent device with ITO as both sides of electrodes.[7] In this work, we used graphene as a top electrode and ITO as a bottom electrode to construct a semitransparent inverted PSC as shown in Figure 5.1.

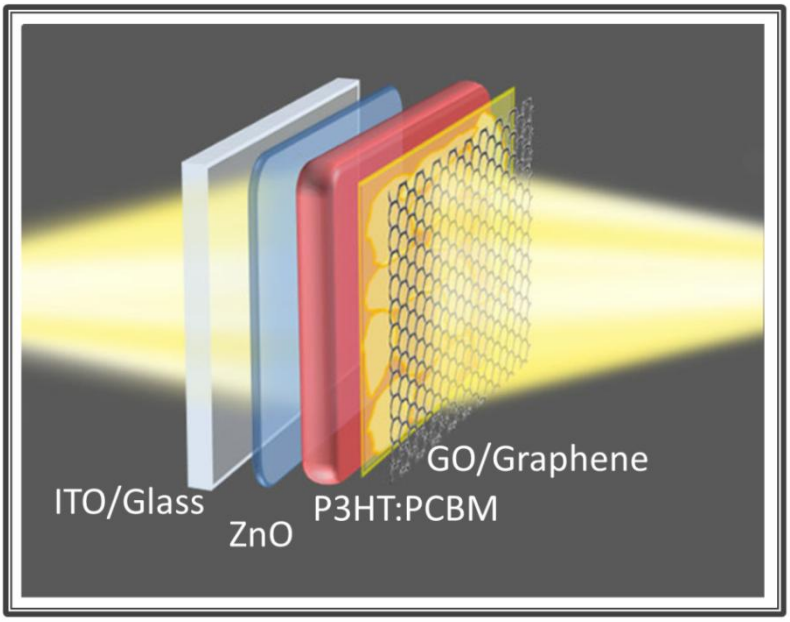

Figure 5.1 A semitransparent inverted polymer solar cell with a structure of ITO/ZnO/P3HT:PCBM/ graphene oxide (GO)/graphene top electrode.

5.2 Characterization of graphene

The crystalline quality of graphene films consisting of different layers as transferred onto a 300nm SiO_2/Si substrate was first analyzed by Raman spectroscopy as shown in Figure 5.2. The G peak (~1583 cm^{-1}) of the graphene Raman spectrum corresponds to the E_{2g} phonon at the Brillouin zone center whereas the D peak(~1320 cm^{-1}) is caused by the breathing mode of sp^2 atoms and is activated by the existence of defects.[8] Because the width and shape of a 2D peak (~2642 cm^{-1}) are highly related to the layer number and stacking order, no obvious change in the intensity ratios of I2D/IG suggests that the sequentially transferred graphene layers were of random stacking order.[9] In addition, a low defect-related D-band peak was observed, indicating that the as-grown graphene films are of high crystalline quality.

The transmittance of the graphene film is reduced about 2~3 % as each layer of graphene was added as shown in Figure 5.3 and the sheet resistance of the graphene film decreases with increasing number of layers as shown in Figure 5.4. The high transmittance and high conductivity make it a good candidate for transparent conducting electrodes. Even though the sheet resistance of graphene films is not as low as that of ITO, it could still fulfill the requirements for some applications such as electrostatic dissipation, cathode ray tubes, touch screens, and flat panel displays.

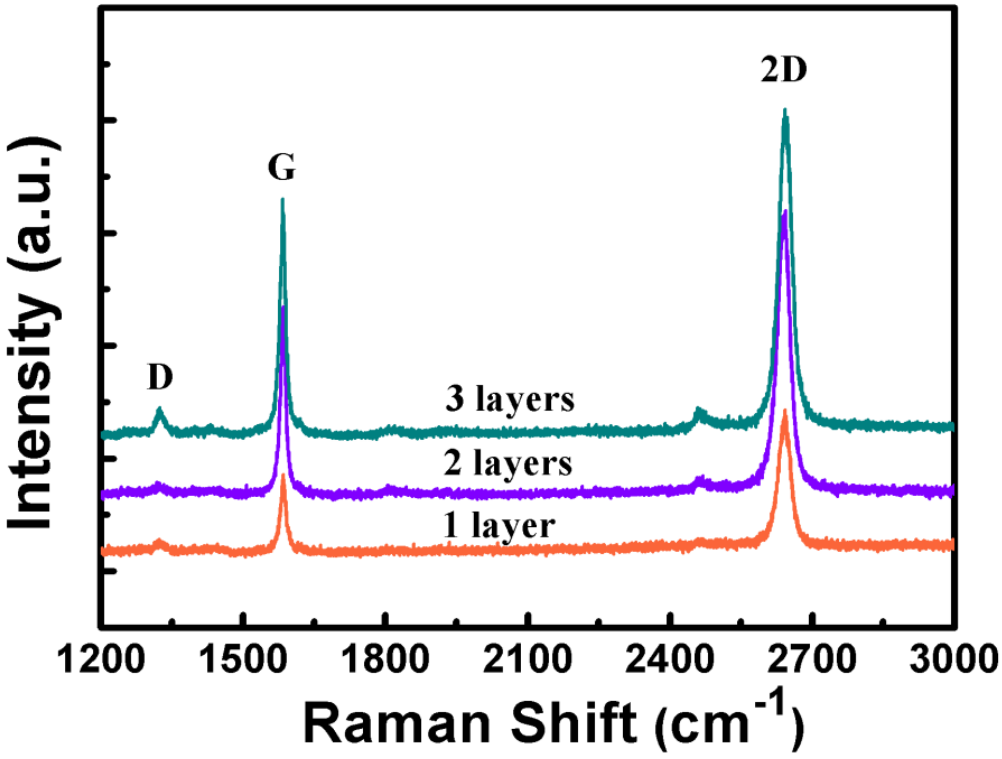

Figure 5.2 Raman spectroscopy of the graphene films consisting of one, two and three layers on glass substrates.

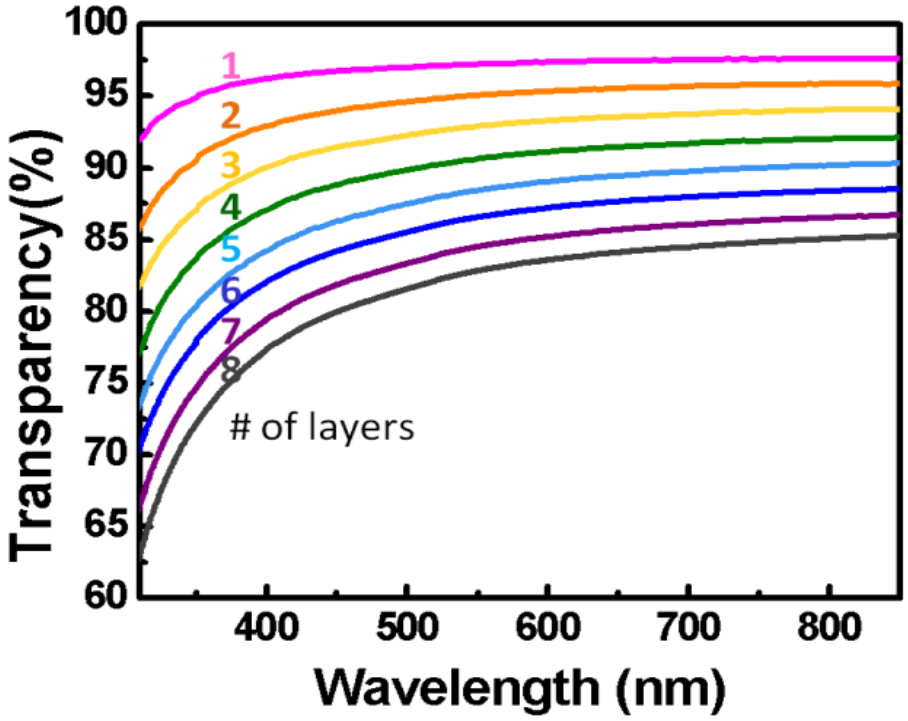

Figure 5.3 The transmittance of the graphene films on glass substrates consisting of various numbers of layers.

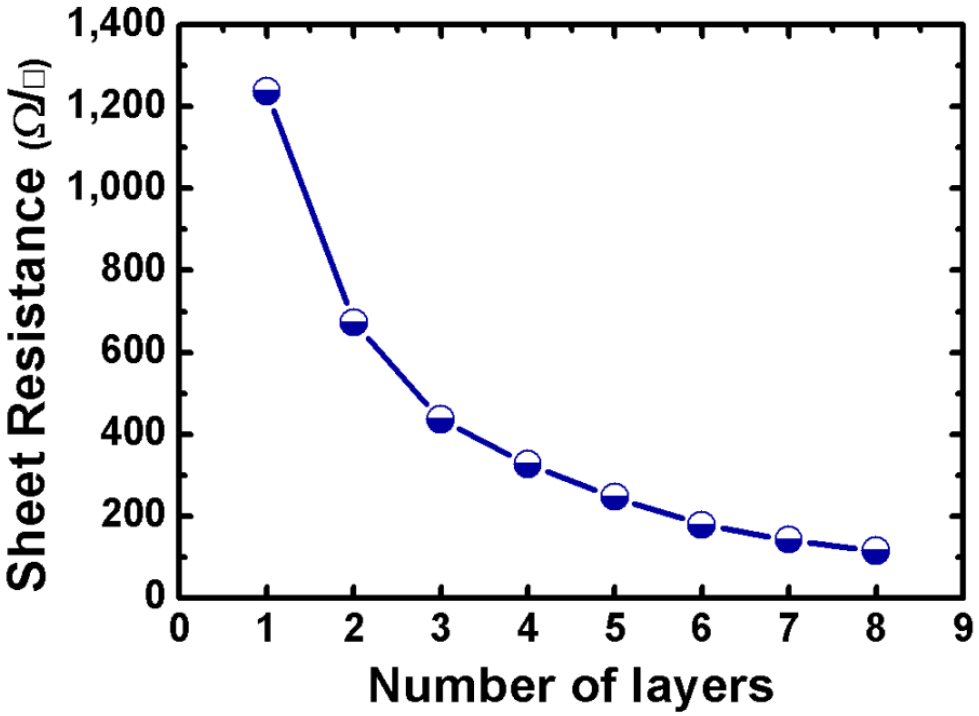

Figure 5.4 The sheet resistance of the graphene films on glass substrates consisting of various numbers of layers.

5.3 Lamination process for graphene top electrode

5.3.1 Thermal release transferring method

For the preparation of the graphene top electrodes, we synthesized graphene films grown on copper foils using the chemical vapor deposition (CVD) processes.[10] Here, we used the roll-to-roll production method which was reported by S. Bae et al.[11] to transfer the graphene film. After growth, the surface of the graphene film with copper foil was attached to a thermal release tape (Nitto Denko). Then, the copper foil was etched by immersing the sample into iron nitrate solution (0.4 g/mL). (Figure 5.5, Step B) The graphene film with thermal release tape was rinsed with deionized water to remove the residual etchant and then dried by N_2 flow for further removal process.

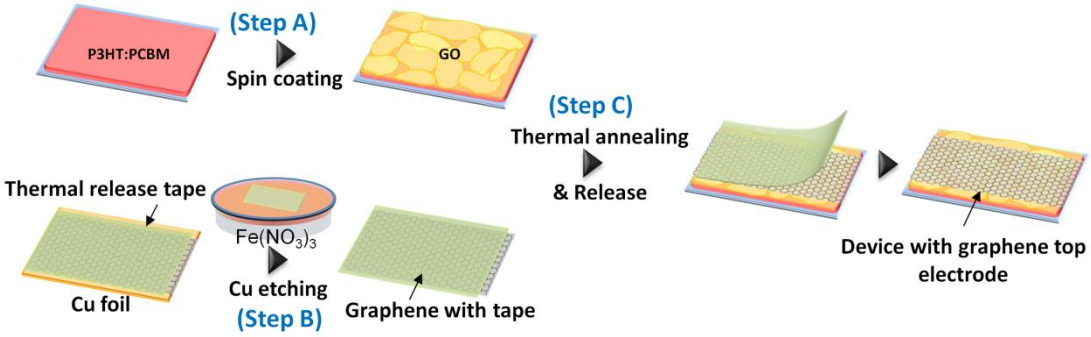

Figure 5.5 Fabrication of the ITO/ZnO/P3HT:PCBM/GO device before depositing the top electrode (Step A). Top lamination processes of graphene electrodes by the graphene film transferring (Step B) and thermal annealing/releasing processes (Step, C).

For the deposition of the top graphene electrode, the graphene film with thermal release tape was thus placed on top of the ITO/ZnO/P3HT:PCBM/GO device followed by the removal process (Figure 5.5, Step C). In the fabrication of polymer solar cells, thermal annealing is a widely used approach for improving the power conversion efficiency of devices by controlling the nanoscaled morphology of a P3HT:PCBM blend.[12] The removal of the thermal release tape from the graphene film was thus simultaneously conducted during thermal annealing treatment, where the entire device of ITO/ZnO/P3HT:PCBM/GO/graphene film with thermal release tape was heated on the hotplate at 120 ^{o}C. All simultaneous thermal annealing/releasing procedures were conducted in the glove box. Repeat the removal process, we can get multilayer graphene which provided better conductivity and the total annealing/releasing time of the device was controlled to be 10 minutes.

5.3.2 Device characterization

The cross-sectional SEM image of the semitransparent solar cell consisting of a device structure of ITO/ZnO/P3HT:PCBM/GO/graphene top electrode (6 layers) is shown in Figure 5.6. Figures 5.7(a) and (b) shows the morphological image of P3HT:PCBM blend film with 1 layer and 6 layers of the top laminated graphene electrode respectively by atomic force microscope (AFM). It reveals that with increasing the layer of graphene, the roughness is also increased.

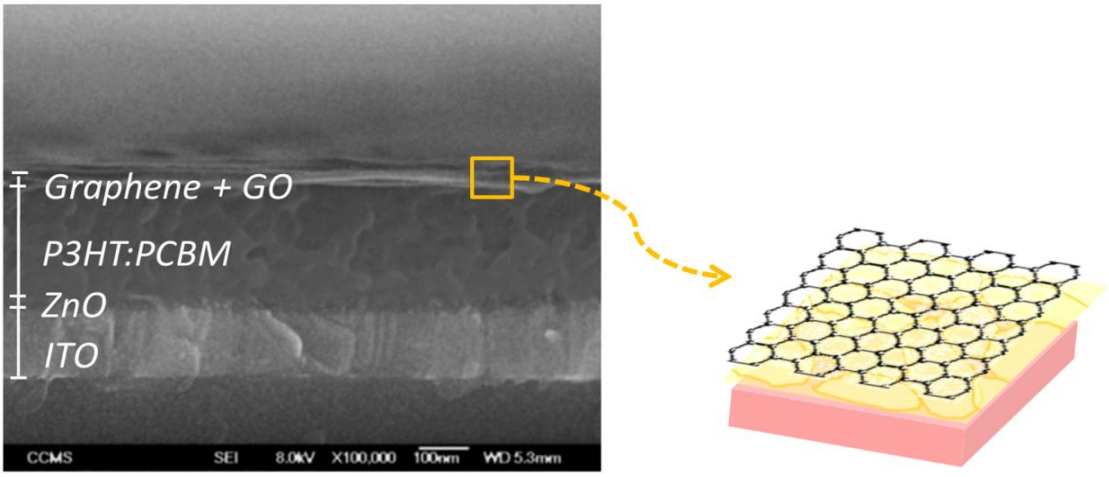

Figure 5.6 The cross-sectional SEM image of the device structure of ITO/ZnO/P3HT:PCBM/GO/graphene top electrode (6 layers)

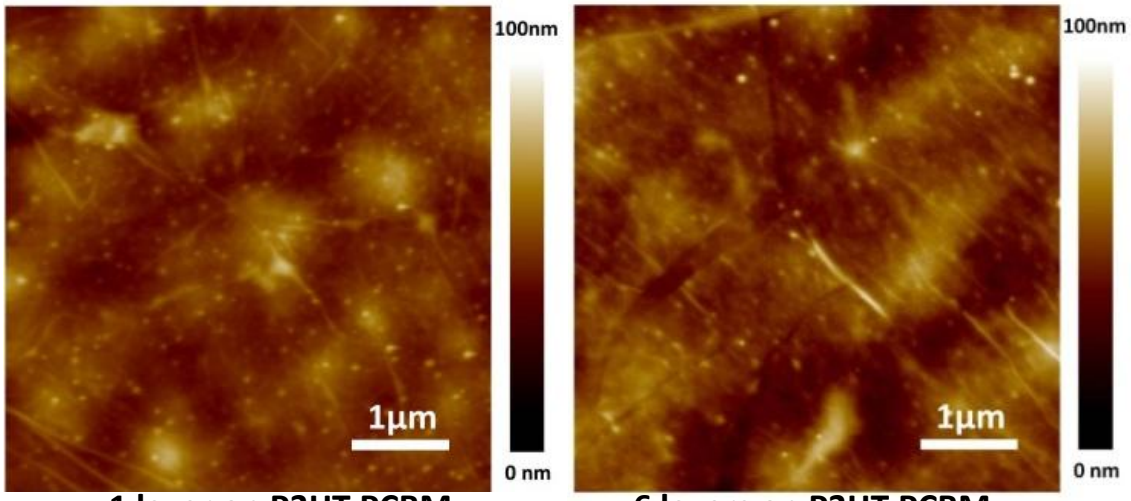

Figure 5.7 (a) and (b) the morphological AFM image of the device structure of the ITO/ZnO/P3HT:PCBM/GO/graphene top electrode (1 layer) and (6 layers).

The semitransparent polymer solar cell with both cathode (ITO) and anode (graphene) being transparent is shown in the inset of Figure 5.8. The area of each device is about 10 mm^2. The transmittance spectrum of the semitransparent solar cell is shown in Figure 5.8 and a high transparency with wavelengths beyond 700 nm was obtained where P3HT/PCBM has no absorption, which makes the graphene-based semitransparent solar cells a promising candidate for the applications of power-generated windows or multi-junction solar cells.

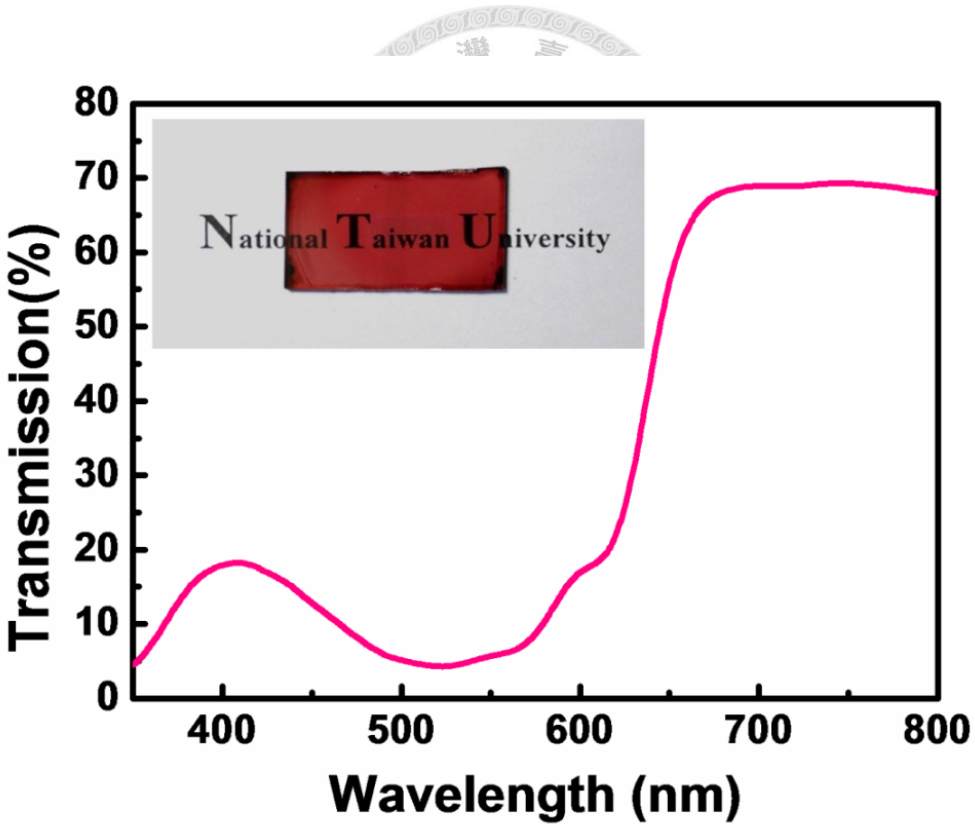

Figure 5.8 The transmittance of this semitransparent polymer solar cell. The picture of the semitransparent device was shown in the inset.

5.3.3 Device performance

The current-voltage characteristics of semitransparent polymer solar cells are shown in Figure 5.9, and Table 5.1 also summarizes the device performance. Compare the device performance to the standard cell, one reason for the higher J_{sc} of the standard opaque cell is attributed to the lager optical absorption since the incident light passes twice through the active layer due to reflection on metal electrodes. The lower fill factor is the mainly limiting parameter on the current device performance of the graphene-based semitransparent solar cell.

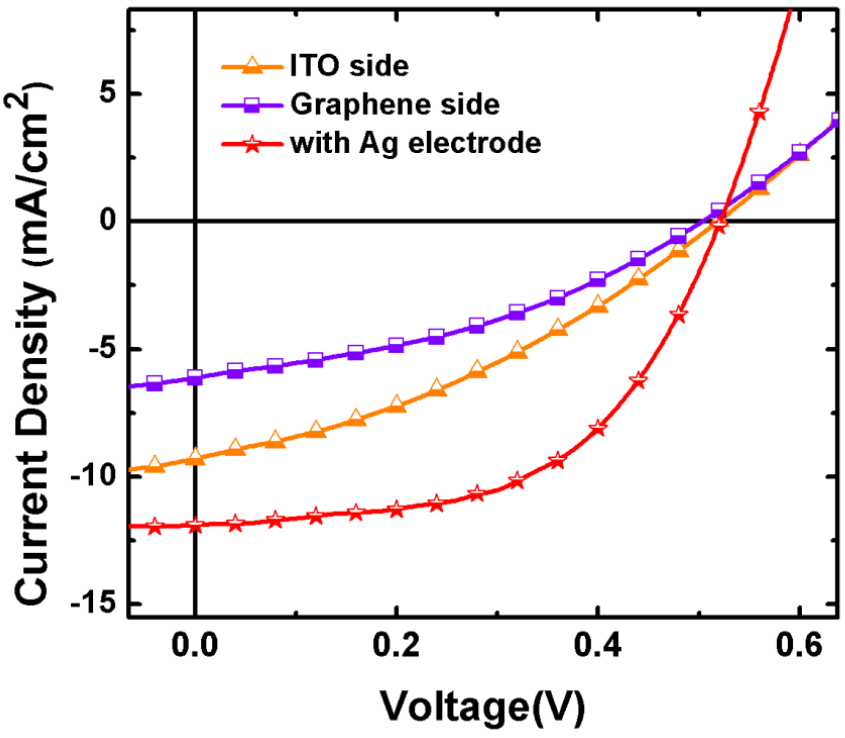

Figure 5.9 Current-voltage characteristics of the semitransparent polymer solar cells with light shining from the ITO side or the graphene side respectively and a standard cell with Ag electrode is also shown. (A.M. 1.5 illumination, 100 mW cm^{-2}).

Table 5.1 Summaries of the device performances of the semitransparent polymer solar cells under illumination (A.M.1.5, 100 mW cm^{-2}) from the ITO side and the graphene side. The device performance of the referenced standard opaque device was also shown.

	V_{oc} (V)	J_{sc} ($mAcm^{-2}$)	FF	PCE (%)
ITO side	0.52	9.3	0.34	1.66
Graphene side	0.50	6.1	0.37	1.16
Standard cell (Ag electrode)	0.52	11.5	0.55	3.30

In addition, we have observed asymmetric photovoltaic performance of the semitransparent device as illuminated from two respective sides with different values of J_{sc} accompanied with different shapes of EQE spectra as shown in Figure 5.10.

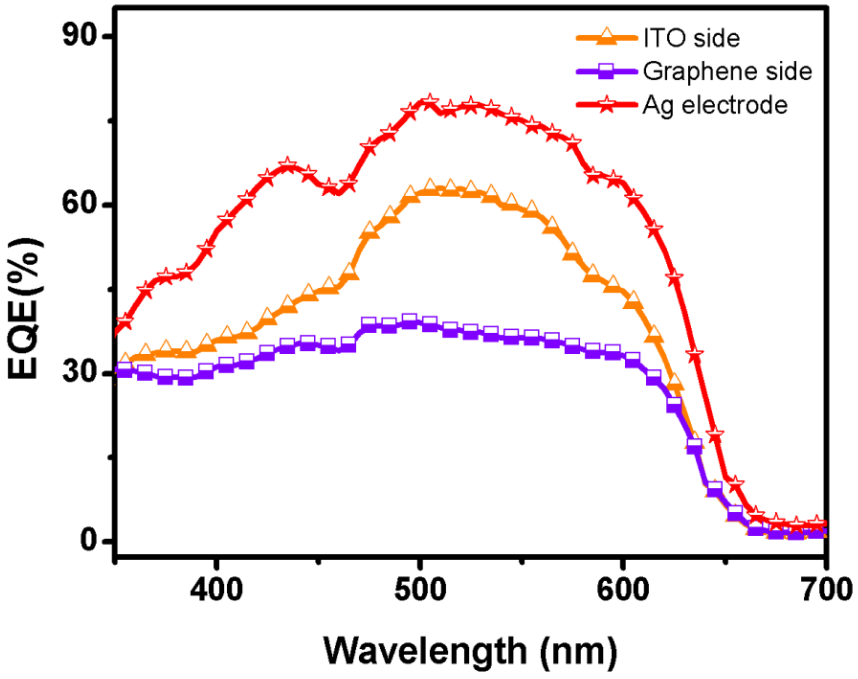

Figure 5.10 EQEs of the standard cell and semitransparent cell consisting of eight layers of graphene as illuminated from the ITO side and the graphene side.

Therefore, we have further performed the optical power-flux simulation of the device with incident light at different wavelength from the ITO side and the graphene side to clarify the asymmetric photovoltaic performance. We examined the power flux distribution of incident light inside the as-fabricated device using the three-dimensional finite difference time domain (3D-FDTD) simulation. The FDTD method discretized Maxwell's equations by central difference in time and space and numerically solved the equations to provide an insight of near-field optical behaviors. The quantity of power flux gives the time-average magnitude of Poynting vector, representing the energy flow in the near field.

The simulated structure was based on the multilayer device model of ITO (150nm)/ZnO(10nm)/P3HT:PCBM(250nm)/GO(2nm)/graphene(8nm) and all the simulated optical parameters of refractive indexes were obtained from the values reported in literatures.[13-17] Incident light having wavelengths of 400nm and 550 nm were used in the simulation as shown in Figures 5.11(a) and (b) respectively.

(a)

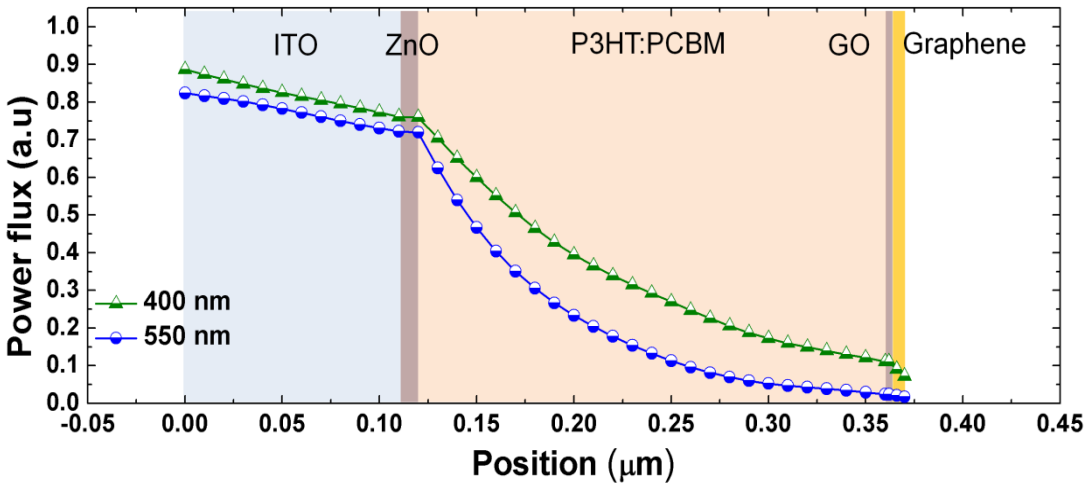

(b)

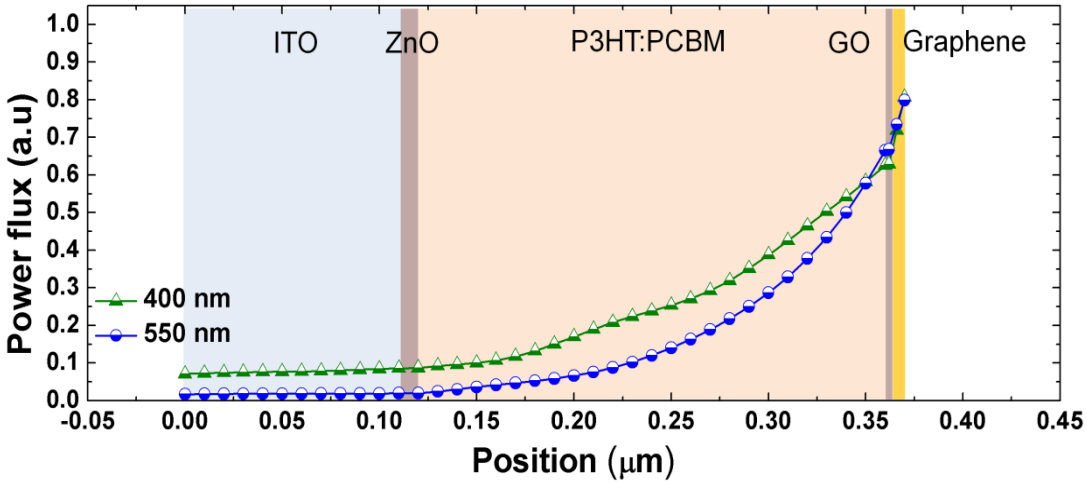

Figure 5.11 (a) and (b) The power flux distributions of incident light at the wavelength of 550nm and 400 nm inside the semitransparent device as illuminated from ITO side and graphene side respectively using the 3D-FDTD simulation.

Due to the stronger absorption coefficient of P3HT at the wavelength of 550 nm, the penetration depth of the incident light is shorter as compared to that using 400 nm illumination, no matter the light was incident from the ITO or graphene side. The power flux in the midway of the active layer had been reduced to below 10% and nearly no transmitted power reached the other side under incident light of 550 nm. In contrast, when the incident light having a wavelength 400 nm away from the absorption peak of the active layer, a nearly 21% of incident power was remained in the midway of the active layer and the incident power was not completely absorbed in the active layer. From the above power flux distribution result, the discrepancy of the light harvesting efficiencies while illuminated from two different electrodes alone can't account for their large difference in J_{sc} and EQEs. Since the concentrations of photogenerated carriers of electrons and holes decrease exponentially with absorption depths, the device performance is also expected to strongly depend on the collection efficiency of the incident electrode.

By the simulation results, we can find that the effect of the asymmetric photovoltaic performance on the incident electrodes is expected to be stronger when the incident light has a shorter penetration depth. This can explain that the difference in EQE values under two different side illuminations is larger at the higher absorption region of the active layer as shown in Figure 5.10.

Figure 5.12 shows the optical reflection spectrum when light illuminated from ITO side and graphene side respectively. The decrease of reflectance at the wavelength below 500nm when light illuminated from graphene side is also a source which caused the different shapes in EQE spectra.

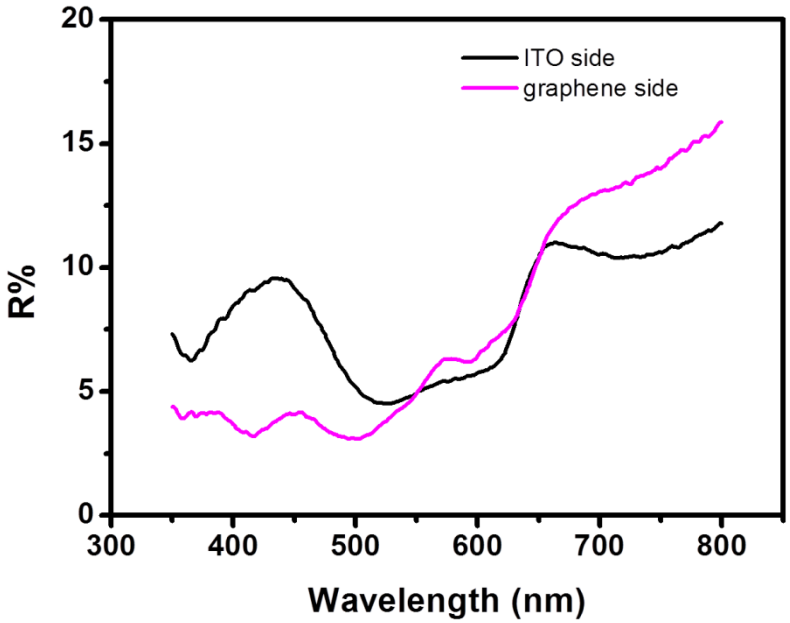

Figure 5.12 Optical reflection spectra of the semitransparent devices when illuminated from the ITO side and the graphene side.

5.4 Modification of the lamination process

5.4.1 Thermal release tape with multilayer graphene

To further enhance the device performance, we have demonstrated a modified method to transfer multilayer graphene through a thermal release tape. Because a single layer of graphene does not have sufficiently high sheet conductivity, multilayer stacking of graphene films is usually required to obtain higher sheet conductance. However, in the conventional roll-to-roll production process which used the thermal release tape while transferring each layer of graphene, there is residual organic impurity between each layer of graphene. It may be the main reason for the lower fill factor which caused the low power conversion efficiency in graphene electrode system. Therefore, instead of following the conventional process, we used only the first-layer of graphene with thermal release tape to be attached onto the second layer of graphene on copper foil (Step C ,Figure 5.13(a)), which was subsequently rolled by the roller. After etching the copper foil, the two-layer graphene film with thermal release tape was further attached to another graphene on copper foil to obtain a three-layer graphene, which can minimize the possible contamination of residual organic impurities between graphene layers during film transferring.[4]

Here, we used a maximum of four layers of graphene with one thermal release tape during each transfer to other substrates or devices, followed by the removal of the top thermal release tape. The procedures were repeated to obtain the graphene electrode with optimal conductance and transparency. The device performance was shown in Figure 5.14, and Table 5.2 summarizes the photovoltaic performances of these devices.

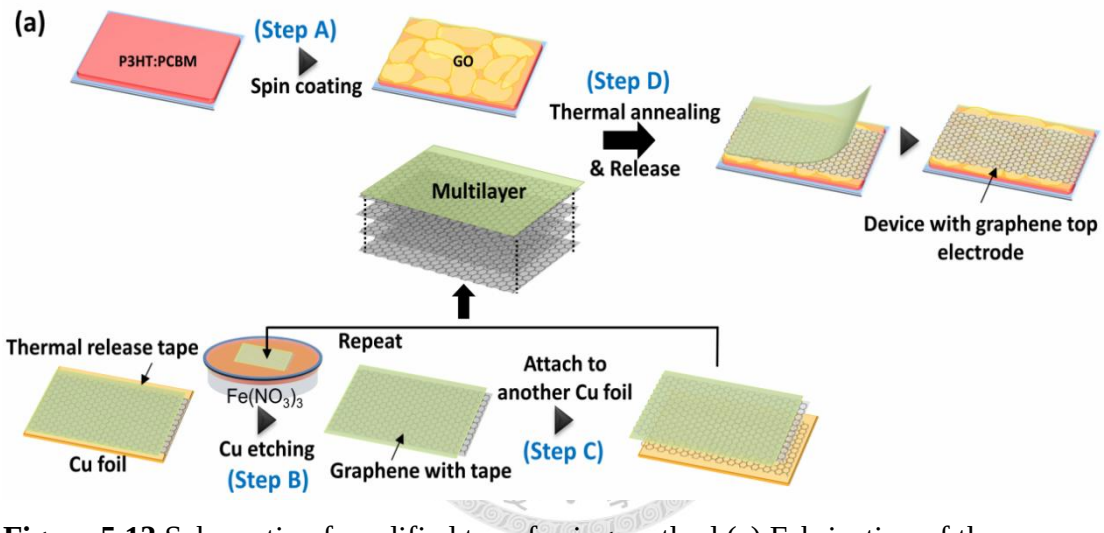

Figure 5.13 Schematic of modified transferring method (a) Fabrication of the ITO/ZnO/P3HT:PCBM/GO device before depositing the top electrode (Step A). Top lamination processes of graphene electrodes by the graphene film transferring (Step B,C) and thermal annealing/releasing processes (Step, D).

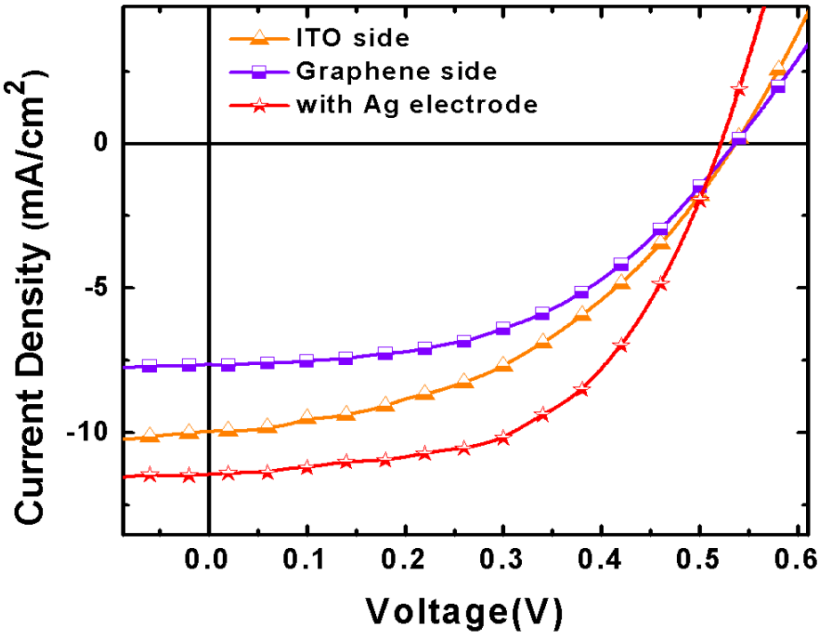

Figure 5.14 Current-voltage characteristics of the semitransparent polymer solar cells using the modified transferring method with light shining from the ITO side or the graphene side respectively and a standard cell with Ag electrode is also shown. (A.M. 1.5 illumination, 100 mWcm^{-2}).

Table 5.2 Summaries of the device performances of the semitransparent polymer solar cells under illumination (A.M.1.5, 100 mW cm^{-2}) using the modified transferring method and the old method (parenthesis). The device performance of the referenced standard opaque device was also shown.

	V_{oc} (V)	J_{sc} (mAcm^{-2})	FF	PCE (%)
ITO side (old method)	0.54 (0.52)	10.1 (9.3)	0.44 (0.34)	2.40 (1.66)
Graphene side (old method)	0.54 (0.50)	7.7 (6.1)	0.49 (0.37)	2.04 (1.16)
Standard cell	0.52	11.5	0.55	3.30

Using this modified transferring method, the device of semitransparent polymer solar cell through illumination from the ITO side exhibits a power conversion efficiency of 2.4 % which is about 73 % of that of the standard cell, with a J_{sc} of 10.0mA/cm^2, a V_{oc} of 0.54 V, and a FF of 0.44. The semitransparent device while illuminated from the graphene side led to a device performance of a J_{sc} of 7.7mA/cm^2, a V_{oc} of 0.54 V, and a FF of 0.49, yielding a PCE of 2.04 %.

Compared the device performance to that of the old method which has been introduced before, there is a significant enhancement of fill factor which revealed that we have successfully rminimized the residual organic impurity between each layer of graphene. Fill factor is one of the most significant parameters for the energy yield of a solar cell and has a great correlation to charge transport and collection properties, which further influence the device performance. Using the modified transferring method, when the residual organic impurity was reduced, the charge collecting efficiency of the graphene electrode was improved. Therefore, the overall device performance has a significant enhancement.

In Figure 5.15, we can see that the shapes of EQE spectra while light illuminated from different sides are more similar compared to Figure 5.10 which used the old transferring method. This is another evidence of the improved collecting efficiency of graphene electrode.

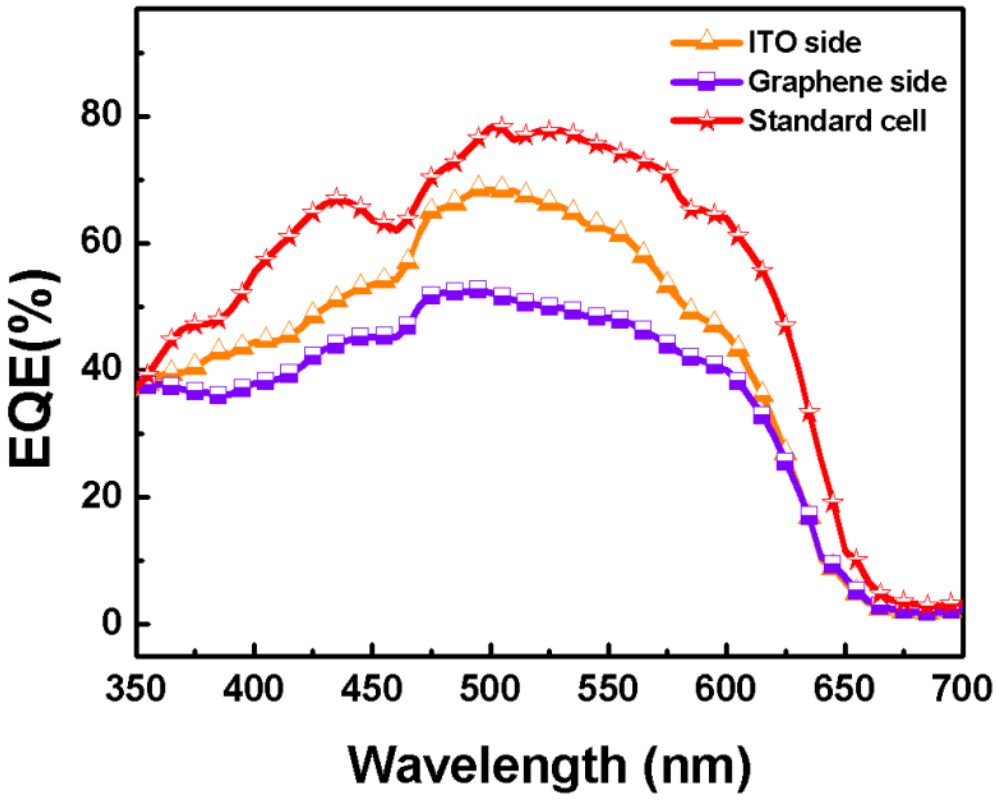

Figure 5.15 EQEs of the standard cell and semitransparent cell using the modified transferring process consisting of eight layers of graphene as illuminated from the ITO side and the graphene side

5.4.2 Layer dependent of graphene

Figures 5.16(a) and (b) plot the current-voltage characteristics of the semitransparent polymer solar cells consisting of the top laminated graphene electrodes with various number of graphene layers with light shining from the ITO side or the graphene side respectively (A.M. 1.5 illumination, 100 mW cm^{-2}). Table 5.3 summarizes the photovoltaic performances of these devices. All the semitransparent devices show a similar V_{oc} of 0.54 V, regardless of whether the light was incident from the ITO or graphene side. The semitransparent devices through illumination from the ITO side exhibit larger J_{sc} and higher PCEs compared to devices illuminated from the graphene side. As illuminated from the ITO side, the semitransparent device achieves the best PCE of 2.50% when the device consists of a top electrode with ten layers of graphene, corresponding to 76% of that of the standard opaque cell. Further increase in the layer number of the graphene electrode does not cause a remarkable change in the PCE as illuminated from the ITO side. By contrast, while illuminated from the graphene side, the semitransparent device consisting of eight layers of graphene exhibits an optimal PCE of 2.04 %, which is approximately 62 % of that of the standard cell; however, further increase in the layer number will decrease the transmittance of incident light and cause the decrease in device performance.

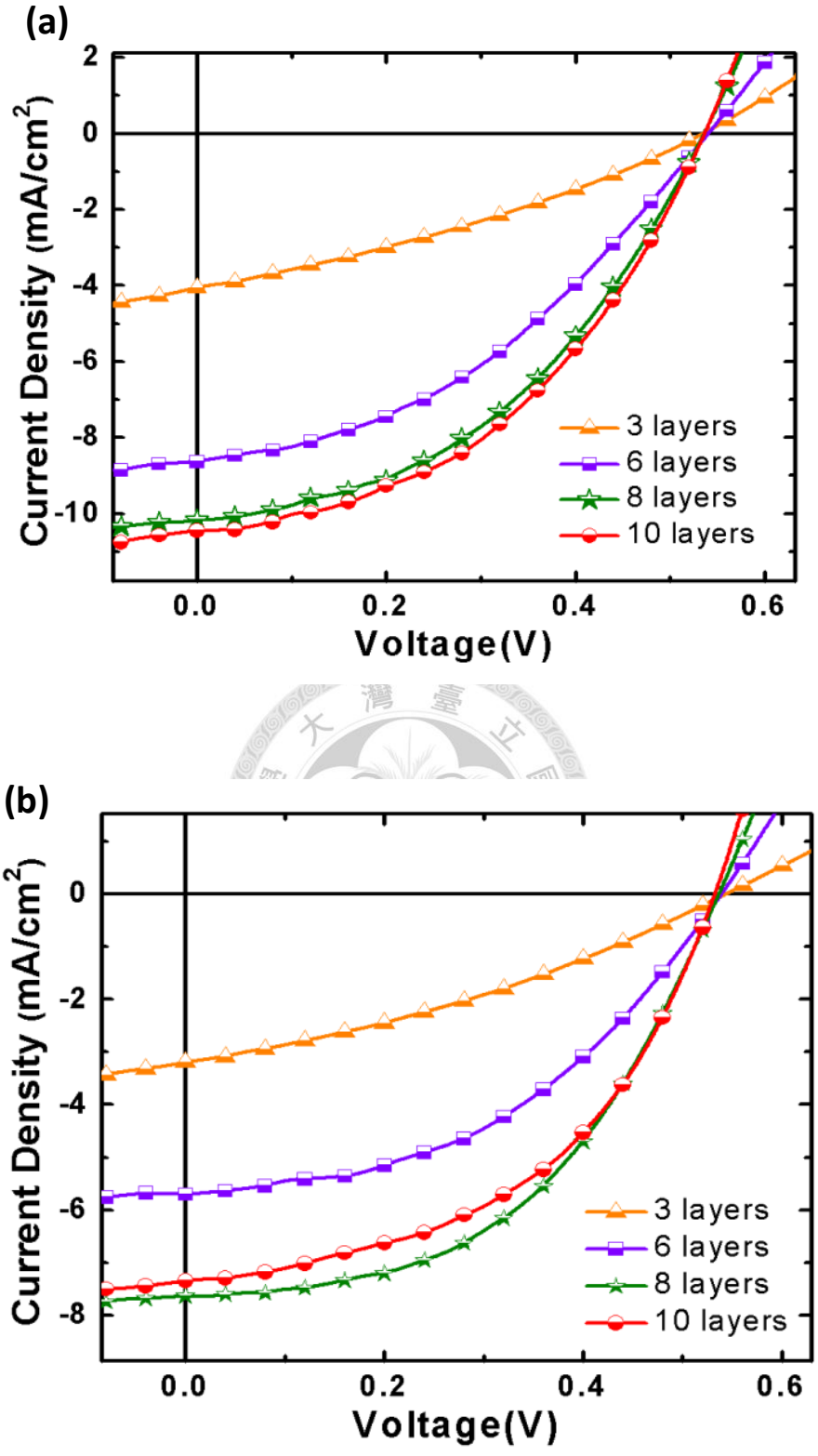

Figure 5.16 (a) and (b) Current-voltage characteristics of the semitransparent polymer solar cells consisting of various number of top graphene layers with light shining from the ITO side or the graphene side respectively (A.M. 1.5 illumination, 100 mW cm^{-2}).

Table5.3 Summaries of the device performances of the semitransparent polymer solar cells under illumination (A.M.1.5, 100 mW cm^{-2}) from the ITO side and the graphene side (parenthesis). The device performance of the referenced standard opaque device was also shown.

ITO(Graphene)	V_{oc} (V)	J_{sc} ($mAcm^{-2}$)	FF	PCE (%)
10 layers	0.54(0.54)	10.5(7.35)	0.44(0.47)	2.50(1.88)
8 layers	0.54(0.54)	10.1(7.70)	0.44(0.49)	2.40(2.04)
6 layers	0.54(0.54)	8.62(5.71)	0.39(0.44)	1.82(1.36)
3 layers	0.54(0.54)	4.05(3.19)	0.32(0.33)	0.69(0.57)
Standard cell (Ag electrode)	0.52	11.5	0.55	3.30

5.4.3 Bifacial polymer solar cell

Interestingly, when both sides of the semitransparent device were simultaneously illuminated (100 $mWcm^{-2}$) using a reflected mirror set, the J_{sc} and V_{oc} of the device were further increased to 14.8 $mAcm^{-2}$ and 0.55 V respectively while the FF slightly decreased to the value of 0.41 as shown in Figure 5.17.

The J_{sc} of the bifaicial device with simultaneous shining from both sides is about 84% of the total sum of the current density of the device illuminated from the two respective sides, suggesting the potential application of the graphene based semitransparent solar cells in the bifacial photovoltaic devices.[18] For further discussion of this effect, we can see from the Beer–Lambert law:

$$T = \frac{I}{I_0} = e^{-\alpha l}$$

Because of the large absorption coefficient of P3HT ($\alpha \simeq 10^5\, cm^{-1}$), the light penetration depth of polymer solar cell (about 100nm) is relative thin compared to other systems. It's useless to enhance the absorption light by further increasing the thickness of the P3HT:PCBM blend. Because the active layer of the semitransparent is relatively thicker (~250 nm), a higher density of excited carriers are close to the incident electrodes, regardless of whether the light was incident from the ITO or graphene side. The power flux in the midway of the active layer was reduced to be about 10% and nearly no transmitted power reached the other side. However, using graphene to substitute for the metal electrode in inverted type polymer solar cell, due to the both side illumination, we can find that an additional absorption was produced as shown in Figure 5.18. This structure gives us another possibility for further improvement of device efficiency in OPV.

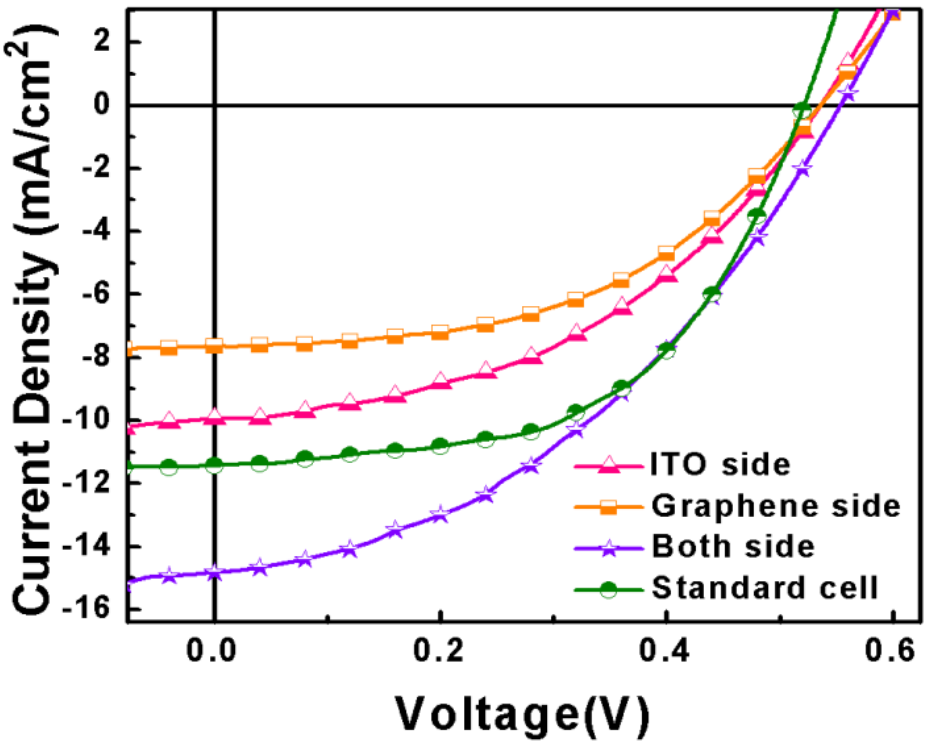

Figure 5.17 The device performances of the standard cell and semitransparent cell using modified transferring method consisting of eight layers of graphene as illuminated from the ITO side and the graphene side. The device performance of the bifacial device illuminated from both sides is also shown.

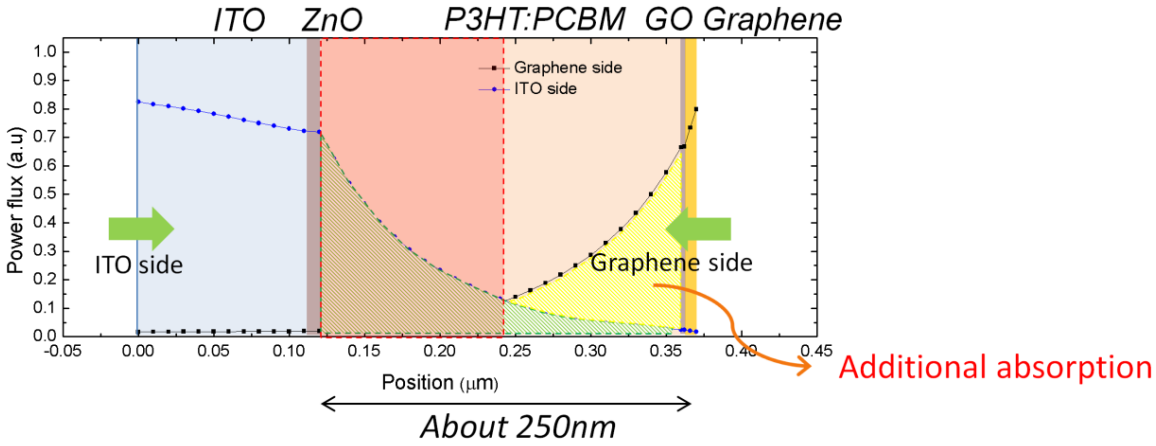

Figure 5.18 The power flux distributions of incident light inside the semitransparent device as illuminated from two respective sides using the 3D-FDTD simulation.

5.4.4 Electrical property

Figure 5.19 exhibits the dark current-voltage characteristics of the semitransparent (8 layers of graphene) and standard devices on a semi-logarithmic scale. Although the semitransparent solar cell with the graphene top electrode exhibits good diode behavior with a rectification ratio of approximately three orders in magnitude at biases 1 V, the device is much more resistive in the forward bias region with a higher serial resistance (8.62Ω cm^2) compared to that of the standard cell (2.33Ω cm^2). The higher serial resistance of the semitransparent device is mainly attributed to a larger sheet resistance of the graphene electrode and also a larger contact resistance between the polymer blend and the anode.

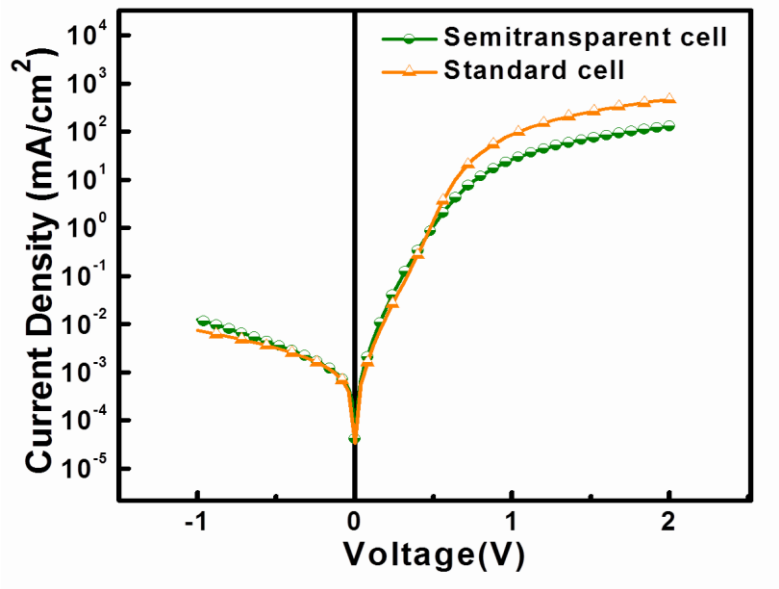

Figure 5.19 Dark current-voltage characteristics of the standard cell and the semitransparent cell (8 layers) on a semi-logarithmic scale.

To further clarify this effect, we performed the transient photovoltage (TPV) measurement to probe the photocarrier recombination behaviors of the semitransparent solar cell with different illuminating directions as shown in Figure 5.20 The recombination lifetime in the semitransparent device was found to be longer as illuminated from the ITO side (35.7 s) than that from the graphene side (18.6 s). Because the same device was used for two respective measurements, the lower recombination rate of the device illuminated from the ITO side is mainly attributed to the higher carrier collection efficiency as a result of lower sheet resistance of ITO. The standard opaque cell exhibits an even longer recombination time of (66.3 s) than the semitransparent device, indicating a more efficient carrier collection.

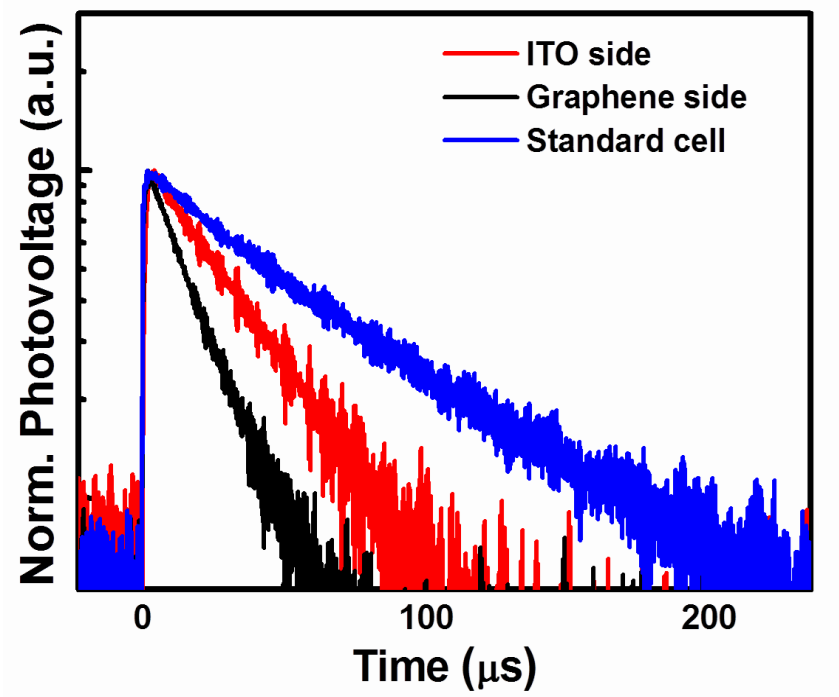

Figure 5.20 The transient photovoltage (TPV) decay curves of the standard cell and the semitransparent cell measured from two different illuminating directions. Devices were illuminated by white light with a power intensity of 50 mW cm^{-2}.

5.5 Refernece

[1] J. Huang, G. Li, Y. Yang, *Adv. Mater.* **2008**, *20*, 415.

[2] Y. Zhang, Y. W. Tan, H. L. Stormer, P. Kim, *Nature* **2005**, *438*, 201.

[3] R. R. Nair, P. Blake, A. N. Grigorenko, K. S. Novoselov, T. J. Booth, T. Stauber, N. M. R. Peres, A. K. Geim, *Science* **2008**, *320*, 1308.

[4] Y. Wang, S. W. Tong, X. F. Xu, B. Ö zyilmaz, K. P. Loh, *Adv. Mater.* **2011**, *23*, 1514.

[5] H. Park, J. A. Rowehl, K. K. Kim, V. Bulovic, J. Kong, *Nanotechnol.* **2010**, *21*, 505204.

[6] Y. Zhou, H. Cheun, S. Choi, W. J. Potscavage, Jr., C. Fuentes-Hernandez, B. Kippelen, *Appl. Phys. Lett*. **2010**, *97*, 153304.

[7] H. Chang, G. Wang, A. Yang, X. Tao, X. Liu, Y. Shen, Z. Zheng, *Adv. Funct. Mater.* **2010**, *20*, 2893.

[8] A. C. Ferrari, *Solid State Commun*. **2007**, *143*, 47.

[9] A. C. Ferrari, J. C. Meyer, V. Scardaci, C. Casiraghi, M. Lazzeri, F. Mauri, S. Piscanec, D. Jiang, K. S. Novoselov, S. Roth, A. K. Geim, *Phys. Rev. Lett*. **2006**, *97*, 187401.

[10] J. Y. Hwang, C. C. Kuo, L. C. Chen, K. H. Chen, *Nanotechnol.* **2010**, *21*, 465705.

[11] S. Bae, H. Kim, Y. Lee, X. Xu, J. S. Park, Y. Zheng, J. Balakrishnan, T. Lei, H. R. Kim, Y. I. Song, Y. J. Kim, K. S. Kim, B. Ö zyilmaz, J. H. Ahn, B. H. Hong, S. Iijima, *Nat. Nanotechnol.* **2010**, *5*, 574.

[12] G. Li, V. Shrotriya, J. Huang, Y. Yao, T. Moriarty, K. Emery, Y. Yang, *Nat. Mater.* **2005**, *4*, 864.

[13] Z. H. Ni, H. M. Wang, J. Kasim, H. M. Fan, T. Yu, Y. H. Wu, Y. P. Feng, Z. X. Shen, *Nano Lett*. **2007**, *7*, 2758.

[14] I. Jung, M. Vaupel, M. Pelton, R. Piner, D. A. Dikin, S. Stankovich, J. An, R. S. Ruoff, *J. Phys. Chem. C* **2008**, *112*, 8499.

[15] R. A. Synowicki, *Thin Solid Films* **1998**, *313*, 394.

[16] M. Hill, Handbook of Optics 2nd edition, Vol. 2, **1994**.

[17] S. Y. Chuang, H. L. Chen, W. H. Lee, Y. C. Huang, W. F. Su, W. M. Jen, C. W. Chen, *J. Mater. Chem*. **2009**, *19*, 5554.

[18] R. Hezel, *Prog. Photovoltaics Res. Appl.* **2003**, *11*, 549.

6

Conclusions

6.1 Conclusions

The core value of this thesis is to demonstrate a polymer solar cell with an inverted architecture which has a possibility to overcome the rapid oxidation of the Al top electrode leading to the instability and degrading of device performance. Compared to conventional polymer solar cells, inverted PSCs are fabricated with a more air-stable, high work function metal as the top electrode. An electron transport layer such as Zinc oxide is inserted between ITO and the active layer to reverse the layer sequence of conventional PSCs. In following chapter, we have investigated transport properties of inverted devices and also apply graphene and graphene oxide to several components of the inverted structure.

In chapter 3 we focus on the UV effect to the ZnO electron transport layer. The S-shape of J-V curves without UV exposure is mainly due to the shallow electron traps in Zinc oxide, which decrease the conductivity of ZnO thin films and make charges transported faster toward the interface than they can extract. However, by UV exposure, owing to the enhanced conductivity of ZnO thin films, device performance is

dramatically improved. We have further investigate the recombination rate of a working device by transient photovoltage measurement (TPV). The result indicates that there is a different recombination mechanism comes from the interface of ZnO thin film and the polymer blend without UV exposure.

In chapter 4 we demonstrate the substitution of graphene oxide and graphene for PEDOT:PSS as a hole transport layer in inverted polymer solar cells. We have known that graphene oxide is a promising candidate to replace PEDOT:PSS. In this work, we try to apply this material to an inverted structure, and the optimized device performance is comparable to that with PEDOT:PSS. Furthermore, graphene which is a two dimensional carbon material has also attracted our attention. We utilize the p-type property of graphene when exposed in air to select the hole. The uniformity and continuity on the active layer make it a good candidate for a hole transport layer. Although the device performance of the device with graphene as a hole transport layer is still lower compared to those with PEDOT:PSS due to the worse contact to the top electrode, these two materials have a great possibility to overcome some shortcomings of PEDOT:PSS for a high performance inverted device.

In chapter 5 we introduce a novel structure of semitransparent inverted polymer solar cell using graphene oxide as a hole transport layer and graphene as a top electrode. Most researchers have focused on the application of graphene to substitute for a bottom

electrode. However, we demonstrate a simultaneous thermal annealing/releasing procedure which can be fully integrated with the typical polymer solar cell fabrication procedures to make a graphene top electrode. We have further improve the process to minimize the residual organic impurities between each layer of graphene and led to a device performance about 73 % of that of the standard cell with Ag top electrode. Furthermore, this structure can also be used for a bifacial illumination, which may be another possibility for further enhancement of device performance in polymer solar cells.